

Doctoral Dissertation
Doctoral Program in Metrology (32.th cycle)

Pulsed Rubidium clock towards space applications

Compact design and advanced locking techniques for a vapor-cell microwave frequency standard

Michele Gozzelino

* * * * * *

Supervisors
Dr. Filippo Levi, Supervisor
Dr. Salvatore Micalizio, Co-supervisor

Politecnico di Torino
March 3, 2020

I hereby declare that, the contents and organization of this dissertation constitute my own original work and does not compromise in any way the rights of third parties, including those relating to the security of personal data.

. . . . . .

Michele Gozzelino

Turin, March 3, 2020

Summary

Compact Rubidium microwave clocks are a key component for precision-timing applications, both for industrial and for scientific applications. Modern global navigation satellite systems also demand always improving stability performances together with a small form factor. The Pulsed Optically Pumped (POP) clock developed at INRiM introduced the use of laser pumping together with a microwave Ramsey interrogation. The atomic sample constituting the frequency standard is a vapor-cell containing ^{87}Rb diluted in a buffer gas. The pulsed technique ensures a high atomic quality factor and lower sensitivity to fluctuations of the experimental parameters. Given these characteristics, a fractional frequency stability of $1.7 \times 10^{-13}\,\tau^{-1/2}$ was achieved, averaging down below 1×10^{-14} even after several days of measurement time in a laboratory environment. With an engineered model, comparable performances can be obtained with a total volume of less than 20 liters and 40 W of power consumption. This makes the technology appealing in particular for space application, where nowadays similar performances are only provided by hydrogen masers, at the expense of larger size, weight and power consumption (SWAP).

This thesis aims at improving the POP clock characterization and to provide different implementation and design options. We present a systematic analysis of the noise sources which currently describes the short-term behavior of the standard. Regarding the clock implementation, we present locking techniques which extend the basic frequency loop. Moreover, we present a compact design suitable for the POP scheme, which can be of interest where SWAP is a concern.

Concerning the short-term investigation, we notice that the noise budget is not limited by quantum noise sources, such as photon or atomic shot noise. The major limitations come from laser frequency and amplitude noises, which are converted into the amplitude of the detected atomic signal. In particular, we investigate in detail the AM-AM conversion with a signal theory formalism. Understanding such conversion mechanisms can point to the right strategy to mitigate them and improve the short-term stability.

On the clock implementation side, we introduce advanced locking algorithms to actively stabilize some physical parameters of interest for the clock operation. Given the low sensitivity of the POP architecture to laser frequency and microwave

amplitude, these parameters need to be stabilized with a low locking bandwidth. We introduce two methods that allow a stabilization of the laser frequency directly on the clock signal, without recurring to external references. This is possible with an extended interrogation sequence and digital processing of the signals. The stabilization of the microwave amplitude can be achieved in a similar manner, by exploiting the Rabi resonances. This last technique, already presented in a previous paper, is recalled and put in relation to the laser locking techniques.

In parallel, a re-design of the core of the physics package, with the purpose of significantly reducing the dimensions and weight of the whole assembly, is presented. In particular, a loaded microwave cavity is introduced, leading to a reduction of volume by a factor 8. A proof-of-principle prototype has been developed, exhibiting short-term stability below $5 \times 10^{-13}\,\tau^{-1/2}$ by using a $1\,\mathrm{cm}^3$ spectroscopic cell. The same mechanical design is used to investigate an alternative buffer-gas mixture (krypton-nitrogen) that provides a much smaller density-shift on the clock transition, compared to the traditional argon-nitrogen mixture. With this configuration, the clock sensitivity to ambient pressure and other barometric effects is reduced by at least one order of magnitude.

All these contributions facilitate the design process in different ways: first of all, by defining in more detail the laser noise specifications needed to reach a certain stability target. Secondly, by enlarging the design options, both from the operational point of view, with the introduction of alternative locking techniques, and from the constructive point of view, with the availability of a compact physics package architecture. Finally, the preliminary investigation of the krypton mixture poses the basis for either relaxed physical requirements or better performances, especially for a possible on-ground application, where the clock is operated at atmospheric pressure.

Finally, the thesis reports on the first experimental tests performed on an engineered physics package suitable for the POP technique. The prototype, produced by Leonardo S.p.A., was built in cooperation with INRiM under the supervision of the European Space Agency. The prototype is tested with INRiM electronics and optics and exhibits state-of-the-art short-term performances.

Acknowledgements

Vorrei ringraziare i miei supervisor e i miei colleghi per l'incalcolabile aiuto datomi durante il periodo di dottorato. Un ringraziamento speciale a Filippo e Salvatore per l'attenta lettura del manoscritto.

Grazie a Claudio per gli innumerevoli consigli e per la pazienza nel rispondere alle mie domande. Grazie ad Elio per l'indispensabile aiuto tecnico.

Grazie ad Alberto, Cecilia, Davide, Giovanni, Ilaria, Marco P., Marco T., Pierre per aver sempre avuto un po' di tempo per un consiglio.

Grazie ad Hai Xiao per l'anno condiviso insieme sull'esperimento, per l'amicizia e l'aiuto reciproco.

Grazie ai miei compagni di dottorato presenti e passati: Anna, Benjamin, Carolina, Filippo, Gianmaria, Matteo, Piero per il supporto ed i momenti divertenti passati insieme.

Un grazie particolare a Morgan e al suo fantastico gruppo di ricerca per avermi ospitato all'ICFO durante il periodo di secondment. È stata un'esperienza che mi ha arricchito umanamente e professionalmente.

Infine, *last but not least*, grazie ad Adalberto, Jacopo e al gruppo di Leonardo S.p.A. per l'ottimismo, la dedizione al progetto e l'interessante scambio di competenze ed idee.

Funding: This work has been partially founded by ASI through the contract GSTP6.2 AO7935.

Contents

List of Tables

List of Figures

Chapter 1

Introduction

Rubidium atomic frequency standards find a variety of applications where a stable oscillator is needed. They are usually realized by stabilizing the frequency of a quartz oscillator onto the ground-state microwave transition of a rubidium sample. In such a way, they benefit from the good long-term stability of the Rb atomic resonance, while delivering an RF output that can be easily managed. Among the ground-state Zeeman sublevels, the atomic line chosen for the clock operation is the one corresponding to the $m_F = 0 \rightarrow m_F = 0$ transition, since it is the most insensitive to environmental perturbations.

The most widelyspread and technologically-ready device based on this principle is the lamp-pumped Rubidium Atomic Frequency Standard (often abbreviated as RAFS or RFS). This kind of device finds its application where long-term stability requirements exceed the specifications of quartz oscillators and at the same time limits of cost, size, weight and power consumption prevent the use of other high-performing frequency standards (such as Hydrogen masers or Caesium beam clocks).

One natural field of application is the space sector. RAFS are indeed employed in every advanced global navigation satellite system (GNSS), such as GPS [1], GALILEO [2], GLONASS [3] and BeiDou [4]. Rubidium standards are also attractive for space missions where precise timing is needed. One notable example is the GAIA mission, where a Rb clock was deployed to provide the required time-stamping capability for the acquisition of the most detailed Milky Way map ever made [5].

The need for improved satellite navigation systems and the always higher demand for precise timing are driving the development of better performing standards. For example, one-way space radiometric tracking (which is regarded as the natural improvement of the nowadays used two-way tracking) requires on-board clocks that outperform the currently employed RAFS [6–8]. Another sector which demands always better timing is high-speed telecommunication, where a distributed network

of stable oscillators is desired. Even stock markets, due to high-speed trading demands, is requesting for accurate time-keeping ability [9]. Even though many of these tasks can be fulfilled with synchronization to UTC via GNSS receivers, the requirement of a wireless connection poses threats to the security and integrity of the time dissemination system [10]. Compact and reliable on-site clocks would ensure safer protocols, therefore the market is pushing for always better hold-over capabilities for commercial oscillators.

The availability of laser diodes starting from the 1980s paved the way for improved versions of vapor-cell clocks based on laser pumping. A whole new line of research was opened, leading to the realization of high-performing vapor-cell frequency standards. Laser light presents much narrower linewidth, less than 10 MHz for commonly used Distributed Bragg Reflector (DBR) or Distributed Feedback diodes (DFB), compared to a typical linewidth of 1 GHz for the light produced by a discharge lamp [11, 12]. A smaller linewidth means a more efficient optical pumping which in turns enables to detect the atomic resonance with enhanced contrast. Ultimately, for fixed resonance width and noise levels, a higher contrast turns into better short-term stability. The replacement of the lamp with the laser was not as successful as expected in improving the short-term stability of vapor-cell clocks [13]. In fact, the estimated improvement assumed photon shot noise as the limiting factor. Instead, the dominant noise process determining the short-term performance of laser devices was proven to be the coherent noise transfer (phase and amplitude) from the laser source, which can be one order of magnitude higher than the photon shot noise. This notwithstanding, with the proper optimization, laser-pumped vapor-cell standards outperformed the traditional architecture by one order of magnitude, leading to short-term stability very close to $1 \times 10^{-13}\ \tau^{-1/2}$ [14].

The introduction of the laser in the field of compact frequency standard led to the investigations of spectroscopic tools different from the continuous wave double-resonance technique. One notable example is the Coherent Population Trapping (CPT) scheme, that allows probing the alkali hyperfine transition by all-optical means. Few notable implementations of this interrogation scheme demonstrated short-term stability very close to $1 \times 10^{-13}\ \tau^{-1/2}$ [15, 16]. The absence of a microwave cavity enabled a strong miniaturization of the CPT system. After the first realization at the US National Institute of Standards and Technology [17], so-called "chip-scale clocks' based on CPT have become a fertile field of research, concerning both atomic clock improvement [18–22] and micro-cell manufacturing [23–26]. Of course, the use of a miniaturized cell leads to a degradation of the short-term stability due to lower atomic line contrast and larger resonance linewidth [27, 28]. Nevertheless, such devices are of interest as they provide a local oscillator with a stability of the order of 1×10^{-11} after one day of averaging time, with a power consumption of only a few hundreds of mW and a total volume of few cm^3. They are thus much stabler than comparable size temperature-stabilized quartz oscillators and much lighter and power-efficient than oven-controlled crystal oscillators,

bridging the gap between these two extremes.

Laser pumping is also suitable to pulsed schemes, both with CPT [29] and with microwave interrogation [30]. In particular, the Pulsed Optically Pumped (POP) clock developed at INRiM was the first high-performing clock to ensure good long-term performance (with stability in the 10^{-15} region). More recently, also one implementation of the pulsed CPT showed medium-term stability below 1×10^{-14}, with the use of the autobalanced-Ramsey interrogation scheme [31]. The underlying reason is the different sensitivity of the various clock architectures to laser power and frequency fluctuations, via the light-shift. We will see how the pulsed techniques are more favorable in this sense as most of the atomic evolution is performed in the dark. The interest in the Pulsed Optically Pumped scheme is testified by the increasing number of groups actively working on the subject: INRiM (Italy) [32], LTF (Switzerland)[33], SIOM and NTSC (China) [34, 35], VNIIFTRI (Russia) [36]. Recently, there has been also the involvement of private companies, such as Leonardo S.p.A. (Italy) and Frequency Electronics Inc. (United States). Significantly, the POP clock has also been proposed as a candidate for the future GPS generation, together with the mercury ion clock under development at Jet Propulsion Laboratory [37, 38].

The studies performed during my PhD research involve some steps towards the development of the POP scheme as a mature technology for space and high-demanding applications. One direction was exploring some strategies to simplify the clock implementation. In particular, advanced algorithms enabling the stabilization of the microwave field amplitude or the laser frequency directly on the clock signal were refined and further characterized. The other guideline of the research I conducted during my PhD activity moves directly in the way for possible use of the POP technique for spaceborne applications. In this sense an optimization of the physics package with particular attention to the overall size and weight is necessary. For this purpose, a redesign of the cavity-cell assembly was performed with the introduction of a loaded cavity, able to significantly reduce the size of the core elements of the clock. The proposed solution has led to an eight-fold reduction in the cavity volume, with consequent promising reduction of weight and power consumption for the complete apparatus. Finally, a technology transfer activity in cooperation with Leonardo S.p.A. has been conducted. The project goal is the realization of a fully operational space-qualified POP clock prototype for GNSS applications. In particular, my contribution was in the electromagnetic design of the cavity and in the first experimental tests on the physics package prototype.

Thesis outline

This doctoral thesis is organized as follows: in the introductory chapter, a brief overview of the traditional rubidium standards is provided, followed by a review of the laser techniques introduced to overcome the known limitations of

lamp-pumped devices. The comparison will stress the peculiarities of each clock architecture with focus on the environmental sensitivities, which is the main concern for a possible space application. In chapter 2 the focus switches onto the Pulsed Optically Pumped (POP) technique, whose development is the main objective of this work. The main characteristic of the POP clock realized at INRiM prior to my activity will be resumed. Moreover, the various sources of noise contributing to the short-term stability are analyzed in detail.

In chapter 3 a technique to actively stabilize the amplitude of the microwave output using the clock signal is presented. Moreover, two alternative algorithms to lock the laser frequency using the clock spectroscopic cell as a reference are introduced and characterized.

In chapter 4 a novel design for a compact cavity cell-assembly suitable for the POP scheme is presented. The design process, implementation and preliminary experimental results are shown.

Finally, in chapter 5, the work done in cooperation with Leonardo S.p.A for the realization of a space-qualified physics package is explained, of course leaving some details omitted for clearance issues. Some preliminary tests, which represent the first milestones towards the validation of the physics package are presented. The tests are being conducted in the frame of a European Space Agency (ESA) contract, which oversees INRiM and Leonardo S.p.A. as the main contributors. The realization of a space-qualified prototype is the real testbed for the establishment of the POP frequency standard as a mature technology, and it was very exciting to contribute to the pursuit of such effort.

1.1 Rubidium frequency standards: a quick overview

Vapor cell frequency standards based on alkali atoms have a long history, starting from the first laboratory realizations in the late 1950s [39, 40], rapidly followed by commercial development [41], to nowadays research and industry applications [42, 43]. The reason for such a long-lasting interest lies in the favorable properties as stable oscillators, joint with compactness, reliability and low power consumption. Vapor cell clocks had their scientific basis in the research made by the Nobel laureates Alfred Kastler and Hans Dehmelt on optical pumping and optical detection respectively [44][45]. These two techniques enable to prepare the atomic state for the interrogation with the microwave radiation and to detect the atomic population with a high signal-to-noise ratio. Other key components are the use of a buffer gas, which strongly suppresses Doppler broadening [46], and the isotopic filtration, the latter providing better pumping efficiency. After the seminal realization by Arditi and Carver [47] many studies and technological developments have been introduced in the following decades. Depending on the application, the focus was moved from

compactness and low price to always improving stability performance. In the latter case, the use of rubidium frequency standards in the most advanced Global Navigation Satellite Systems (GNSS) led to remarkable technological achievements [5, 48, 49].

1.1.1 Basics of a vapor-cell Frequency Standard

In Fig. 1.1 the building blocks of a passive microwave frequency standard are highlighted. A crystal oscillator is locked to the atomic resonance via a frequency lock loop. The raw output of the oscillator is usually split, one arm serving as the final-user device output. The other arm is frequency multiplied into the microwave region by an RF synthesis chain to match the atomic resonance frequency. The microwave radiation is sent to the physics package, containing the atomic sample, to perform the clock interrogation. After probing the resonance, a suitable discriminator signal is extracted and used to correct the frequency of the crystal oscillator.

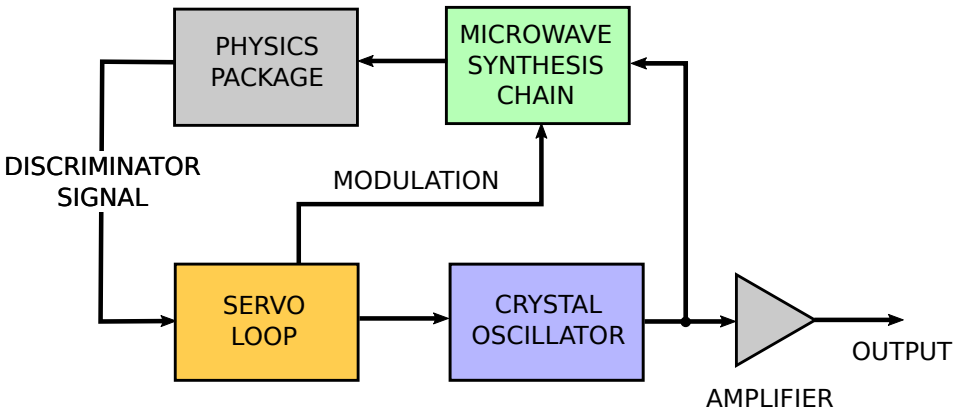

Figure 1.1: Schematics of the key components of a Rb frequency standard.

The choice of rubidium-87

The choice of the atomic species is performed by considering many technological and practical issues. Obviously, atoms are not naturally designed to provide frequency standards, and thus technological challenges have to be solved. The most obvious one is to produce the RF radiation at the desired atomic transition frequency and at the same time to provide an easily accessible frequency as output of the frequency standard (e.g. 10 MHz). To ease the practical realization, a proper choice of the atom, upon which the standard is based, must be done. The atomic

species should have a narrow atomic line, mostly insensitive to environmental perturbations, which would serve as the clock transition. Moreover, the transition must lie in a frequency range which can be covered by an electronic synthesizer. Finally, the population of the clock states should be easily read out in order to achieve a good signal-to-noise ratio for the frequency loop.

Rubidium-87 meets most of the requirements: it has a narrow transition (linking the ground-state hyperfine levels) in the GHz range. Moreover, it presents two easily accessible transitions (D-lines) in the near-infrared which can be used to prepare the atomic state for the clock interrogation and to read-out the atomic population.

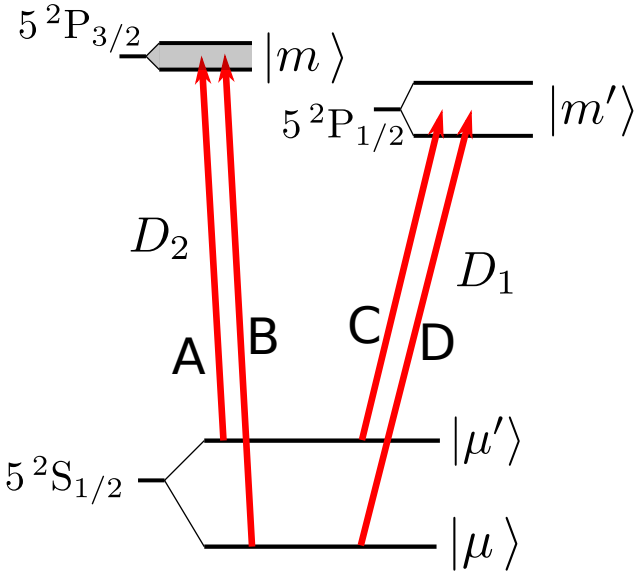

Figure 1.2: Scheme of the rubidium energy levels. The splitting between the ground states $|\mu\rangle$ and $|\mu'\rangle$ of ^{87}Rb at 6.8347 GHz is used as the clock frequency reference.

More specifically, the two ground states Zeeman sublevels $|F = 1; m_F = 0\rangle$ and $|F = 2; m_F = 0\rangle$ are used as the clock states, as their energy is insensitive to magnetic fields at first order. Moderate magnetic shielding (on the order of few thousands) is thus enough to achieve a stable reference. The absolute value of the clock transition (6.8 GHz) is high enough to provide a high transition quality factor, but still low enough to be reached by frequency multiplication from a crystal oscillator. Moreover, this frequency range implies the use of a microwave cavity of reasonable size (few cm), keeping the dimension of the physics package compact. At the same time, the cavity inner dimensions are large enough to store a few cm glass cell, easily accessible by a light beam, leading to a high signal-to-noise ratio. Compared to ^{133}Cs and ^{85}Rb, ^{87}Rb has a lower nuclear spin ($I = 3/2$), thus more atom contribute to the $m_F = 0$ transition, providing a larger clock signal. Finally, rubidium has another favorable property: the two natural isotopic species (^{87}Rb and ^{85}Rb)

show a not negligible overlap in the lower ground state energy levels (see Fig. 1.3). A glass cell containing only ^{85}Rb can thus be tailored as a filter to absorb light resonant with only one of the two clock states. The light emerging from the filter is much more effective in optically pumping the atoms of the clock spectroscopic cell and in creating the population imbalance needed for the clock interrogation. An alternative technique makes use of a single clock cell filled with natural rubidium (integrated-filter cell). As the light propagates through the cell, it is filtered by ^{85}Rb and efficient optical pumping takes place in the rear of the cell. This solution provides more compactness, at the expense of parameters optimization. Indeed the temperature and size of the filter (an accessible parameter in the case of a discrete filter design) cannot be chosen independently from the clock cell.

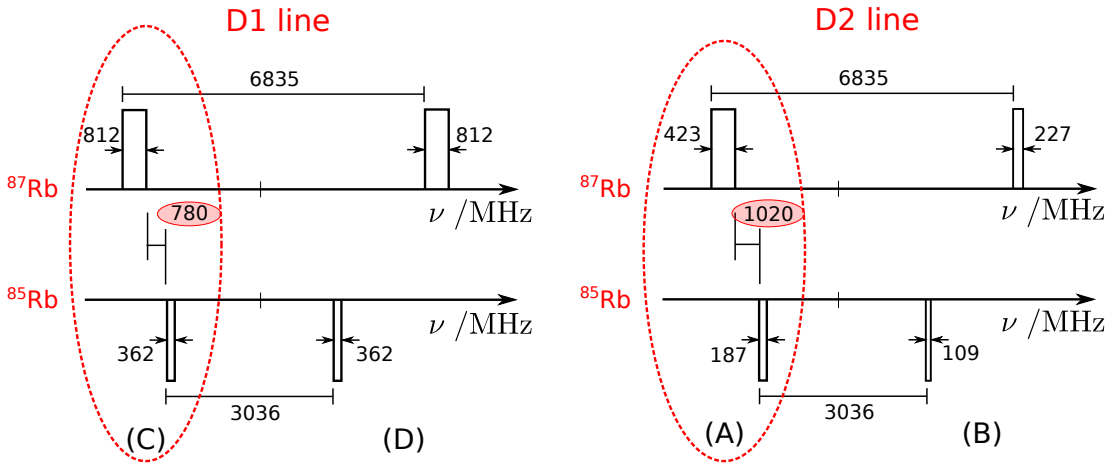

(a) D_1 line.

(b) D_2 line.

Figure 1.3: Structure of the D optical lines (connecting the $5\,^2S_{1/2}$ ground state to the $5\,^2P_{1/2}$ and $5\,^2P_{3/2}$ excited states). The diagram shows the relative position of the optical lines between ^{85}Rb and ^{87}Rb (the labels refer to Fig. 1.2). The reported width of the transitions represents the maximum splitting between the upper states hyperfine levels. When the spectrum of a lamp is considered, many broadening mechanism are involved, leading to a linewidth greater than 1 GHz for the single lines, thus a substantial amount of overlap is present between the two isotopes for line A and C.

Finally, rubidium presents a vapor tension slightly lower than that of cesium, which still allows obtaining a reasonable atomic density in vapor phase by operating in a temperature range moderately above room temperature (30 °C to 60 °C).

Dicke narrowing

One of the key ingredients for obtaining a stable slaved oscillator is to perform the spectroscopy of a narrow atomic resonance. Any kind of time-varying shift or broadening mechanism affecting the atomic line is, of course, reflected on the local oscillator stability. When using a hot vapor confined in a cell, the main broadening mechanism is caused by the atomic motion through the Doppler effect. Moreover, the inelastic collision of the alkali atoms with the cell walls causes an immediate loss of coherence. Both problems can be mitigated by using a buffer gas, as originally proposed by Dicke [46]. In the case of inert gases, the alkali atoms can perform hundreds of elastic collisions without losing coherence. The motion of the Rb atoms is diffusive and, if the mean-free-path between collisions is smaller than the radiation wavelength λ ("Dicke-condition"), the net result is to obtain an effective reduction of the transition linewidth [46]. In a true diffusive regime, the profile of the atomic transition can be expressed as [50]:

$$I(\omega) = A \frac{1}{\left(\frac{D(2\pi)^2}{\lambda^2}\right)^2 + (\omega_0 - \omega)^2} \tag{1.1}$$

where D is the diffusion constant of the alkali in the buffer gas (inversely proportional to the buffer gas pressure). Thus the shape of the resonance becomes Lorentzian, with a full-width-at-half-maximum of $4\pi^2 D/\lambda^2$. In the case of a transition in the microwave region, this value can be much smaller than the Doppler width, leading to transition widths of few tens of Hz [51–53].

Double-resonance technique

The usual spectroscopic method to probe the hyperfine clock transition of alkali atoms is the so-called double-resonance technique (often shortened as DR). Light resonant with an optical transition (usually the D_1 or D_2 line) is used together with microwave radiation whose frequency matches the clock transition. The microwave field excites the magnetic dipole transition linking the two ground states hyperfine levels while the light beam spectrum is tailored to be mainly resonant with only one of the two ground-states. In this way, the light source acts as a pump and effectively creates a population imbalance between the two clock states (for a ^{87}Rb vapor in thermal equilibrium, assuming a Boltzmann distribution, the two ground-states are almost equally populated, with a population imbalance smaller than 0.1 %). As a consequence of optical pumping, the amount of light transmitted by the vapor increases. If the microwave radiation is exactly resonant with the atomic transition, it will tend to equalize again the population of the two levels. Thus, if we look at the transmission of the pump light as a function of the microwave field frequency, we will see a dip, due to augmented absorption, when the microwave field frequency matches the atomic frequency. By this means it is possible to probe the microwave

transition with optical photons. The use of light for pumping and detection allows detecting the resonance with high contrast and high signal-to-noise ratio.

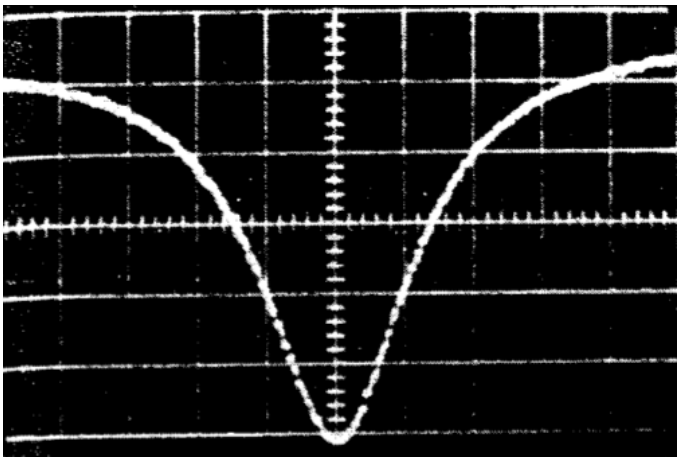

Figure 1.4: Atomic resonance probed with the double-resonance method as a function of the microwave transition detuning (the x-axis has 30 Hz per division). Extracted from [40].

1.1.2 RAFS: state of the art

Rubidium Frequency standards have shown relatively minor changes in their working principle. Of course, the architecture has evolved together with the technology over the years, since their first realization. Arguably, the greatest change happened in the electronic part, with digital components taking over analog counterparts. In particular, direct digital synthesizers (DDS) provide better tunability and lower FM distortion. The main improvements in the short-term performance where possible by improving the spectral characteristics of the light generated by the lamp, leading to better optical pumping. In this regard, the goal of reaching stabilities below 1×10^{-12} at one second, once considered unreachable, has been achieved with a Rb lamp employing Xe as buffer gas, together with a thin-film bandpass filter [1, 12]. Regarding the long-term performance, a careful engineering of the various components has allowed reducing some of the thermal and light-shift sensitivity coefficients. In particular, a light-shift intensity coefficient as low as $1 \times 10^{-12}/\%$ [1, 49] has been reported. In parallel, refined thermal and mechanical designs permitted a better stabilization of the environmental parameters affecting the clock transition. This has led to remarkable long-term stability results, in the low 1×10^{-14} region (without drift removal) and in the low 1×10^{-15} region at 10 days of averaging time (with the use of an aging model to predict the slow frequency drift) [48].

1.1.3 Strong and weak points

As shown in the previous section, lamp-pumped rubidium frequency standards have very favorable characteristics. Namely, they present good long-term stability while remaining compact and lightweight. Nevertheless, some issues remain unsolved. First of all, they suffer from a not easily predictable aging, of few parts in 10^{-14}/d. Many possible explanations have been addressed to this observed phenomenon, the main candidates being Helium permeation [54, 55] and light-shift [56] (caused by a modification of the spectral properties of the lamp or of the filter). Indeed the lamp, even if it is considered reliable concerning the noise properties and expected lifetime, is at the same time one of the weak points. It is long known that discharge lamps suffer from intensity jumps, which have been proven to degrade the device time-keeping ability significantly [57–59]. Since the mode of operation is a plasma regime, its power output is not easily modeled and still not completely understood [60].

1.2 High-performing vapor-cell frequency standards

The improvement of rubidium and cesium compact clocks has been an active field of research, and it still provides room for systems optimization, as well as fundamental physics studies to provide better theoretical models. The most performing experimental realizations make use of laser for atom preparation and probing. Among laser-based frequency standards, we can further distinguish between devices based either on cold atoms or upon hot-vapor cells. Cold-atoms-based devices can be characterized in terms of accuracy and can possibly benefit from micro-gravity in space applications [61]. However, in the framework of this dissertation, we will focus only on vapor-cell devices, given the closer affinity with the main matter. For the interested reader, we point at the literature on the subject [62–64]. We also report at least two remarkable commercial products based on cold atoms: one by the French company Muquans [65], the other developed by the American company Spectradynamics [66].

Vapor-cell clocks based on laser pumping can be cataloged by the interrogation scheme. With the exception of coherent-population trapping, all schemes employ a microwave cavity to perform the clock interrogation, while the laser is tuned to be resonant to one of the two hyperfine ground states and acts both for pumping and probing. The other common feature is the use of buffer-gas to increase coherence time and suppress Doppler-broadening at microwave wavelengths. An alternative approach to increase the atomic population coherence time is the use of a wall-coated cell. However, this technique is not common in the field of frequency standards. Even though very long coherence time has been obtained with

this method [67], the main limitations arise from the higher thermal coefficient [68] and the phase-shift effects due to atomic motion [69].

The effect of buffer-gas collisions on the atomic coherence properties and thermal stability of the standards are further discussed in section 4.1.4, with application to the new design of a compact physics package. Here in the following, we will focus on the laser and microwave interrogations schemes, recalling the main features and reviewing some of the state-of-the-art published results.

1.2.1 Continuous-wave double-resonance spectroscopy

A scheme of a typical continuous-wave (CW) laser-pumped frequency standard is shown in Fig. 1.5. The laser is sent to the physics package after a beam shaping, collinear to the quantization z-axis, the latter provided by a DC magnetic field excited by a solenoid. The microwave transition is excited by means of a microwave cavity, often designed to be resonant with the atomic transition with the cylindrical TE_{011} mode. This cavity mode provides a rather uniform H_z component over the typical cell volumes [70]. For the clock transition, it is useful to define the Rabi angular frequency corresponding to the magnetic field $\vec{H}$, expressed as [50]:

$$b(\vec{r}) = \mu_0 \mu_B H_z(\vec{r}) \tag{1.2}$$

where μ_0 is the vacuum permeability and μ_B the Bohr magneton [50]. The laser is tuned to be resonant with only one of the two ground states. The excited state is either the $5\,^2P_{1/2}$ or the $5\,^2P_{3/2}$ manifold, depending if the D_1 or D_2 line is chosen. The D_2 line is often preferred, as the greater transition strength provides a more efficient pumping. Given that the hyperfine splitting of the excited levels is small enough compared to the typical absorption profile of the clock cell (broadened by Doppler effect and buffer gas collisions), a simplified description of the clock as a 3-level system is often adequate for a quantitative description of the various processes. With reference to Fig. 1.2, we can thus introduce also an optical Rabi frequency associated with the transition between the ground state $|\mu\rangle$ and and the state $|m\rangle$ excited by the optical field $\vec{E}(\omega_L, t, \vec{r}) = E_0 \vec{e_\lambda} cos(\omega_L t + \vec{k} \cdot \vec{r})$:

$$\Omega_R = \frac{E_0}{\hbar} \langle \mu | \, e\vec{r} \cdot \vec{e_\lambda} \, | m \rangle = \frac{E_0}{\hbar} d_{\mu m} \tag{1.3}$$

where $\vec{e_\lambda}$ is the optical field polarization vector, Ω_L its angular frequency and $\vec{k}$ its wavevector.

Another useful quantity is the pumping rate $\Gamma_p = \Omega_R^2/(2\Gamma^*)$. Γ^* is the relaxation rate of the optical state $|m\rangle$, dominated by the contribution from collisions with buffer-gas molecules through quenching mechanisms (see section 4.1.4 and [71]). For the usual experimental conditions it is in the range $2 \times 10^9\,s^{-1}$ to $5 \times 10^9\,s^{-1}$.

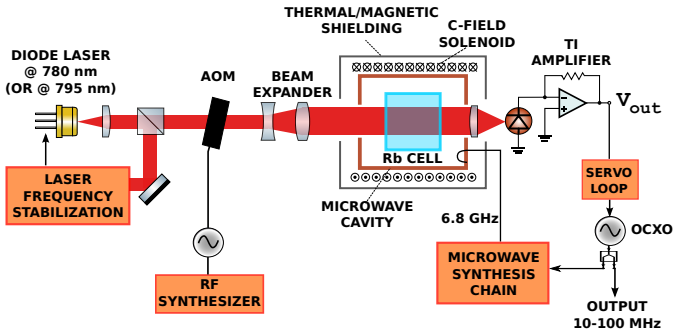

Figure 1.5: Simplified setup of a laser-pumped CW frequency standard.

The operating principle is completely analogous to the lamp-pumped rubidium standards. The laser is tuned close to the transition linking one of the two ground-states and the excited state $|m\rangle$. The laser is usually frequency stabilized to an external reference cell with no buffer gas. Thus, an acousto-optic modulator (AOM) is used to bridge the frequency of the reference laser branch to the desired tuning for the clock cell. A CW microwave radiation is applied together with the laser and the double-resonance is detected by looking at the transmitted laser intensity. The frequency of the microwave radiation is modulated with a square wave with a modulation depth close to the half-width of the resonance. The signal acquired with the photodiode is demodulated and serves as the input to close the frequency loop of the local oscillator.

The width of the resonance is ultimately set by the (transversal) relaxation rate of the ground state coherence γ_2. This is usually limited by the spin-exchange collisions between alkali atoms and lies in the range $200\,\mathrm{s}^{-1}$ to $1000\,\mathrm{s}^{-1}$ for typical temperatures of operation. The observed linewidth is affected also by power broadening both from laser and microwave fields, and is usually well described by a Lorentzian curve, whose full width at half maximum (FWHM) is [72]:

$$\Delta\nu = \frac{1}{\pi}\sqrt{b^2 + (\gamma_2 + \Gamma_p)^2} \tag{1.4}$$

The laser intensity is chosen in order to optimize the detection of the double-resonance. On one hand, raising the laser power would make the optical pumping more efficient and thus increase the line contrast. On the other hand, low laser light intensity is desired to avoid line broadening. It has to be noted that in (1.4) the various parameters depend on the position of the cell, and the resulting detected signal is an average over the whole volume. In particular, the pumping rate changes exponentially along the propagation axis, due to absorption in a thick medium. Moreover, the microwave field amplitude has a spatial dependence determined by the cavity eigenmode.

With such kind of device, very good line contrast (above 20 %) where demonstrated [14, 73] with consequent very good short-term stability (in the low 1×10^{-13}

at 1 s). In the most recent works the photon shot noise contribution was calculated to be in the mid 10^{-14} range. Indeed, the short-term stability can be written as:

$$\sigma_y^2(\tau) = \sigma_{y,\text{shot}}^2(\tau) + \sigma_{y,\text{LO}}^2(\tau) + \sigma_{y,\text{AM-AM}}^2(\tau) + \sigma_{y,\text{FM-AM}}^2(\tau) \tag{1.5}$$

where the main contributions are highlighted. Besides the photon shot noise, there is a residual contribution from the local oscillator phase noise, via the intermodulation effect [74, 75]. The last two terms are usually the dominant ones and they come from coherent noise transfer from the laser. Amplitude fluctuations (AM) are directly transferred to the intensity of the detected signal, while frequency fluctuations (FM) are converted into amplitude by a combination of atomic absorption and atomic cross section fluctuations [76, 77].

Laser intensity and frequency fluctuations play a role also in the medium-term performance. The presence of the light field during the clock interaction gives rise to power and frequency-dependent light shift on the clock transition. Indeed light-shift is thought to be the main source of limitation for continuously operated devices [14]. In the literature, when describing the effect close to an optical resonance, two different light-shift coefficients are introduced to describe the observed shift: a frequency-dependent coefficient $\beta_{LS} = \Delta\nu_{\mu\mu'}/\Delta\nu_L$ and an intensity coefficient $\alpha_{LS} = \Delta\nu_{\mu\mu'}/\Delta I_L$. Since the latter is not always linear in the light intensity, it is good practice to define the coefficient as the clock frequency variation over a fractional change of the intensity around the working point: $\alpha_{LS\%} = \Delta\nu_{\mu\mu'}/(\Delta I_L/I_L)$. Alternative strategies have been proposed to reduce the effect of light shift in CW standards: one option is to modulate the laser light (in intensity or frequency) to create sidebands. By choosing the right modulation index, the various sidebands can have canceling contributions [78]. As we will see in the following section, this is similar to the first-order cancellation obtainable with the CPT scheme. However, the most practical operative condition is to choose a specific laser detuning at which the intensity coefficient is minimized and operate the clock with very low power [79]. Recently, an interesting interrogation scheme has been theoretically proposed to actively compensate light-shift in continuously-operated atomic clocks [80].

Another dependence on the laser power comes from inhomogeneities of the physical parameters (microwave field, magnetic gradients, laser intensity). This is usually named the "position effect" [81] or "pseudo-light-shift" as it mimics the behavior of the off-resonant light-shift.

Other sources of frequency instability in the medium-long term are also due to the microwave amplitude fluctuations. A dependence on the microwave field amplitude comes mainly from inhomogeneities of the magnetic field [82] and from cavity pulling [50]. The latter effect is not negligible for passive Rb frequency standards as it scales as the ratio between the atomic and the cavity quality factors ($\propto Q_c/Q_a$). To mitigate these two phenomena, a low cavity-Q together with a high H_z field uniformity over the active volume are needed. If the fluctuations of power are indeed a limiting factor, an active stabilization might be implemented, either on

an external reference or by exploiting the so-called "Rabi resonances" as proposed in [83].

1.2.2 Coherent Population Trapping technique

The coherent population trapping is a well-known phenomenon, which has been object of study in precision laser spectroscopy [84] and has found applications in frequency metrology [85, 86].

The interrogation scheme is sketched in Fig. 1.6: two phase-coherent laser beams couple the two ground states to a common excited state (Λ-scheme). When the frequency difference between the two beams equals the hyperfine splitting, a quantum interference effect leads to a creation of a coherent state ("dark state") in which the atoms cannot make a transition to the excited level. Consequently, a "dark line" appears in the fluorescence spectrum or, if we look at the transmission through the vapor of the two beams, a "bright line" is observed, due to electromagnetic induced transparency. In a cesium or rubidium cell with buffer gas the linewidth of such resonance can be lower than 100 Hz [87, 88], making it a suitable frequency reference to build an atomic standard. The experimental setup of a

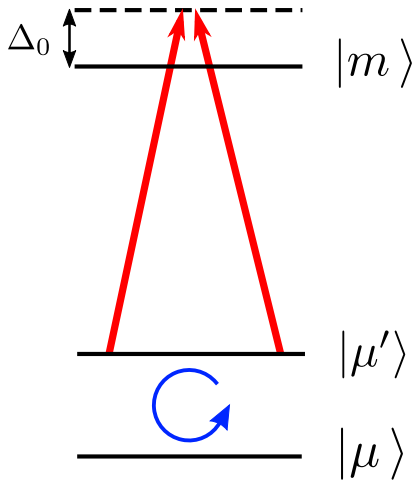

Figure 1.6: Simplified picture of the Λ interrogation scheme.

high-performing CPT standard includes the clock cell, surrounded by a few layers of thermal and magnetic shielding. There is no need for a microwave cavity since the clock frequency is probed by optical means. The phase coherence between the two laser beams is ensured either by two phase-locked lasers or by generating two modulation sidebands from a single laser beam (acting directly on the injection current or with an electro-optic modulator). A microwave synthesis chain is still needed in order to bridge the local oscillator frequency to the hyperfine splitting

of rubidium (or cesium). The synthesized radiation is either compared to the frequency offset between the two clock laser or directly used to drive the modulator to generate the laser sidebands (in this case the synthesized radiation frequency is half the atomic frequency). The clock signal is acquired by looking at the laser transmission through the vapor. The synthesizer frequency is modulated around the maximum of the bright line and the demodulated signal is used to lock the local oscillator frequency in correspondence of the maximum transmission.

To achieve good short term stability a detection of the bright line with high contrast is needed. Two main techniques have emerged as the most effective: the *lin⊥lin* technique and the *push-pull* technique [89, 90]. They have been demonstrated to be equivalent [91, 92] and they both allow the creation of a dark state for the $m_F = 0$ Zeeman sublevels with a large atomic population, avoiding optical pumping towards dark states with high (or low) m_F number (which always occurs where simple circularly polarized light is used).

When a modulated laser is used, the light shift can be canceled at first order by a proper choice of the modulation index, i.e. properly adjusting the power partition among the various sidebands. In fact, the light shift affecting the clock transition due to the various sidebands can be written as [93, 94]:

$$\frac{\Delta\nu_{\mathrm{LS}}}{\nu_{\mu\mu'}} = \left(\frac{\Omega_{RL}}{\nu_{\mu\mu'}}\right)^2 \left[\Theta(m_\phi) + \Xi(m_\phi)\left(\frac{\Delta_0}{\nu_{\mu\mu'}}\right)^2\right] \tag{1.6}$$

Here m_ϕ is the modulation index and Ω_{RL} is the Rabi frequency of the unmodulated beam. The analytical expression of Θ can be found in [93]. What is important here is that the function has a zero crossing for $m_\phi = 2.4$, which can be used to cancel this term. The other term, proportional to Ξ, cannot be canceled simultaneously, but it is usually of second order. Nevertheless, to have a stable modulation index is not straightforward during the clock operation. Indeed, to achieve a medium-term stability below the 1×10^{-13} level, power stabilization and a tight frequency lock are needed, together with a careful control of all the experimental parameters [16].

Regarding the mid-term contributions, light shift still remains one of the main issues. Other mechanisms lead to a sensitivity of the clock frequency to environmental parameters. Buffer-gas introduces a temperature sensitivity which is treated by working around a temperature inversion point for the total shift [95]. Nevertheless, the sensitivity can be few parts in $1 \times 10^{-11}\,\mathrm{K}^{-1}$. Given the absence of direct microwave radiation, there is no dependence on the power of the microwave field. When an electro-optical modulator is involved, there is although a dependence of the clock frequency on the bias voltage amplitude. Active stabilization of this parameter is needed [16], and at a few days timescale a residual contribution is possible. Finally, environmental magnetic field fluctuations must be properly shielded [96].

In the last years a LNE-SYRTE (Paris, FR) has demonstrated a stability of

$3.2 \times 10^{-13}\ \tau^{-1/2}$, averaging down up to $\tau = 100\,\mathrm{s}$ with the use of two phase-locked external-cavity diode lasers (ECDL) in a $lin \perp lin$ configuration. The same group reported similar performances on a simpler and more compact setup, using an alternative polarization modulation technique [15, 97]. FEMTO-ST (Besançon, FR) built a high-performing setup based on the push-pull technique [16].

Pulsed CPT

To overcome the light shift problem and at the same time pursuing a higher atomic quality factor, a pulsed version of the CPT was introduced. The beams in the Λ configuration are sent to the atomic sample, then turned off for a free-evolution time T and then switched on again. This basic sequence is repeated indefinitely and the atomic population is usually probed at the beginning of the laser pulse. The introduction of the free-evolution time creates an additional modulation pattern in the CPT resonance (often called "Raman-Ramsey" fringes) [98]. The width of the central fringe thus obtained is proportional to $1/T$, similarly to the Ramsey interrogation scheme. Given that the atoms spend most of the time in the absence of light, the light-shift coefficients are strongly reduced. Recently, to better understand the observed fringes, a theoretical model considering also density and propagation effects has been developed [99]. The transient nature of the dark state production and evolution has been underlined, leading to a not trivial dependence of the clock resonance parameters on temperature, pumping rate and detection time.

Some notable reported results regarding short-term stability can be found in [29, 100]. Even if a reduction of the light-shift power of more than a factor 20 of the clock sensitivity to laser intensity variation was demonstrated, both devices are still limited in the mid-term by environmental sensitivities [96]. Recently, with the use of an improved interrogation protocol, called "symmetric-autobalanced-Ramsey" a clock stability of 2×10^{-14} at 1000 s was demonstrated for the first time [31]. The "autobalanced-Ramsey" protocol was introduced in the field of ion optical clocks [101] as an improved Ramsey scheme. By introducing an additional sequence with a shorter free-evolution time, it is possible to construct a double loop which makes the interrogation of the resonance much more insensitive to imperfections of the probing laser [102]. In the CPT clock, where the same atoms are probed many times during subsequent cycles, a symmetric version of the scheme was employed to avoid memory effects.

1.2.3 The Pulsed Optically Pumped (POP) technique

The strategy of overcoming light-shift related issues by switching to a pulsed approach was firstly investigated by Arditi and co-workers in 1964 [103], following the suggestion of Alley [104]. Clearly, if the pump-probe light is switched off during

the clock interrogation phase, light-shift is greatly suppressed. This is the main motivation towards the development of a device working in a pulsed regime. In [103] there was also another innovation: the clock interrogation was realized with the Ramsey technique [105]. Similarly to cesium beams clocks, where the atoms pass through the microwave cavity twice, with a free-space evolution in the middle, here two phase-coherent microwave pulses are sent to the microwave cavity, separated by a free-evolution time, while the atoms are essentially fixed in space by the presence of the buffer gas (the mean path covered by the atoms is much smaller than the linewidth for the time of the clock interaction). In 1978 English resumed the idea of a pulsed rubidium standard to solve the light shift issue, alternating optical pumping and microwave interrogation [81]. The first practical implementations, even though they demonstrated a reduced light-shift coefficient, did not lead to improved performances in terms of frequency stability. This was mainly because of technological issues. In particular, optical pumping with the use of a lamp is not efficient enough to ensure a good duty cycle. In recent years the group led by A. Godone at INRiM proposed and realized a laser Pulsed Optically Pumped standard, first with microwave detection (realizing a pulsed passive maser [106]), followed by a prototype with optical detection [32].

In the following chapter, the main characteristic of the latest prototype will be resumed. Here we just compare the reported sensitivities of the best performing vapor-cell clocks to laser intensity and frequency variations (table 1.1). We can notice how the pulsed techniques are intrinsically less sensitive to variations in the field properties, with the POP clock demonstrating a higher degree of resilience.

Table 1.1: Sensitivities to laser parameters (intensity I and frequency ν_L) for the clock architectures described in the text. ABR stands for symmetric autobalanced Ramsey.

	$\alpha_{LS\%} = \frac{(\Delta\nu/\nu_0)}{(\Delta I/I_0)}$	$\beta_{LS} = \frac{(\Delta\nu/\nu_0)}{\Delta\nu_L}$
CW DR [14]	$2 \times 10^{-12}/\%$	1×10^{-11}/MHz
CW CPT [16]	$1 \times 10^{-11}/\%$	4×10^{-12}/MHz
Pulsed CPT [29]	$3 \times 10^{-12}/\%$	4×10^{-12}/MHz
Pulsed CPT (with SABR) [31]	$2.4 \times 10^{-13}/\%$	2.5×10^{-14}/MHz
POP [32]	$6 \times 10^{-14}/\%$	2×10^{-14}/MHz

Chapter 2

Pulsed Optically Pumped Rb clock

2.1 Experimental realization

In this section the main characteristics of the experimental realization of the POP clock at INRiM [32] are resumed. The clock building blocks and components are detailed. Moreover, the basic timing and clock operation is recalled, as it will serve as the basis for the more advanced locking techniques introduced in chapter 3.

It is common practice to divide the setup into three building blocks: the optics, physics and electronics packages. The optics includes the laser head, an optical isolator, the beam shaping optics, the frequency stabilization setup and the acousto-optic modulator for the switching. The physics includes the cavity-cell assembly, the quantization field solenoid, thermal shields to set and stabilize the operational working point. Three layers of magnetic shielding complete the package. The electronics provides the signal acquisition chain (trans-impedance amplifier, signal conditioning plus low noise digital-to-analog converter), as well as the pattern generator which sets the timescale of all the clock signals. The computational core of the electronics part is a field-programmable-gate-array (FPGA) , which processes the input signals and manages the frequency loop. In the electronics package we also include the microwave synthesis chain, which creates the 6.8347 GHz radiation starting from the 100 MHz local oscillator. In Fig. 2.1 a sketch of the whole setup is shown. The three main packages are highlighted in boxes of different colors.

2.1.1 Physics package

The physics package presents a cylindrical geometry and a layered structure. The layers provides the adequate thermal and magnetic shielding for the atomic sample. The core of the atomic clock is indeed the spectroscopic cell where the

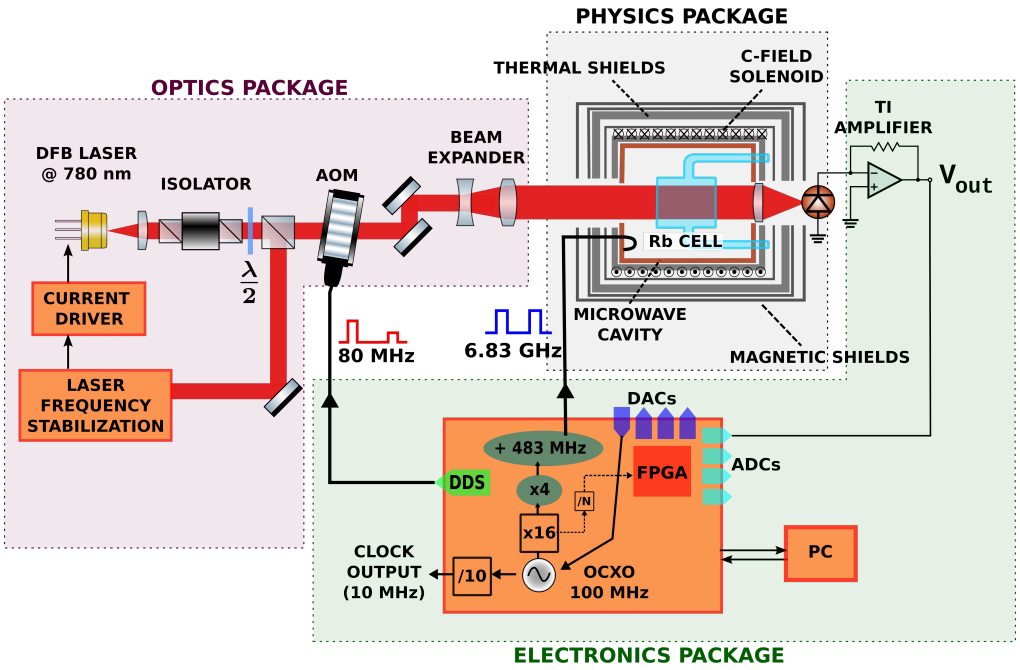

Figure 2.1: Scheme of the main components of the POP setup. The three main packages are highlighted in the colored boxes. TI: transimpedance-amplifier.

atomic sample is stored. The cell is filled with isotopically enriched ^{87}Rb and with a mixture of argon and nitrogen (1:1.6 ratio, 25 torr total pressure). The cell is made of quartz (fused silica) and is cylindrical, with internal length and diameter equal to 2 cm and wall thickness of 1.4 mm. The cell is placed at the center of a cylindrical microwave cavity, in order to excite the magnetic dipole transition between the two clock states. Two filling stems reach out from the cell body and exit the microwave cavity. In this way excess rubidium can condensate outside the cavity volume.

The cavity also shares a cylindrical geometry, with internal diameter $2a = 5.2$ cm and length $d = 4.9$ cm. With this dimensions, together with the dielectric loading deriving from the quartz cell, the TE_{011} mode is resonant with the atomic clock transition. The cavity is made of molybdenum, a metal with good electric conductivity and low thermal expansion coefficient. It is placed inside an aluminum cylinder which acts as an oven to bring the cavity and the clock cell at the operational temperature. The latter is set to 66 °C to minimize the buffer-gas-related instability [107].

The oven also holds a solenoid which provides the quantization magnetic field. The relative stability of the current generator is better than 1×10^{-5} for the typical measurement timescales. We operate the clock with a bias magnetic field of 1.5 µT. This value ensures enough splitting of the magnetic transitions to avoid Rabi pulling on the clock line [108].

The next layer is a magnetic shield, followed by a second aluminum cylinder. The latter serves as a thermal shield and its temperature is actively stabilized. A Kapton heater is wrapped around it and the temperature is sensed by two negative-temperature-coefficient resistors. The two stems are in thermal contact with the oven, thus also the thermal gradient between the core of the cell and the end tip pf the stem is kept constant. This mitigates the effect of buffer gas migration between the stem and the cell, which leads to additional temperature-dependent frequency fluctuation on the clock frequency [107].

The physics package is completed by 2 mu-metal magnetic shields. The total magnetic shielding factor is above 1000 on the axial direction. The thermal and magnetic shields are thermally and electrically insulated and aligned by means of Teflon spacers.

The whole package is placed under vacuum (2×10^{-7} mbar) in a dedicated vacuum chamber. The vacuum is mainly needed to ensure better thermal insulation and possibly barometric effects due to ambient pressure and humidity changes [109, 110]

2.1.2 Electronics package

The electronics package is the "brain" of the atomic clock. All input and output are managed with the use of a field-programmable-gate-array (FPGA), which provides synchronous operation at the level of 100 ns. The input hardware is composed by a set of analog-to-digital converters (ADCs) and a signal conditioning unit (SC) aimed to match the impedance and to adjust the signals dynamic range. The output is a specular set of digital-to-analog converters (DACs). The FPGA is able to run 6 general purpose loop functions. One is used for the main clock loop, the others can be used to implement additional locking schemes (see chapter 3) or as a monitor of environmental parameters. The input and output of each loop function can be programmed to be linked to the appropriate hardware. The FPGA hosts a pattern generator that drives each block according to the sequence of steps typical of the clock configuration, and implements the loop functions accordingly. The FPGA is interfaced to a computer for setting the working parameters and for monitoring (and optionally logging) the internal data flow. The operational parameters for the clock operation are stored into the local memory, thus they can be changed via PC communication, but the unit can also run as standalone.

The synthesis chain is described in detail in [111]. It is based on a commercial unit (Pascall XMN) which incorporates a 100 MHz oven-controlled crystal oscillator (OCXO) and a direct multiplication stage which delivers a low-phase-noise output at 1.6 GHz. The output of the module is splitted and three different frequencies are generated by direct multiplication, programmable division and Direct Digital Synthesis (DDS) respectively. These frequencies are then mixed together to reach the atomic clock frequency. The use of a DDS ensures simultaneous and fast phase,

amplitude and frequency modulations. Moreover, it allows to scan the atomic resonance over a wide frequency range. This synthesis scheme is well suited for generating the atomic microwave frequency of rubidium as well of cesium (both the 9.192 GHz radiation and half of it in case of CPT [112]) just by changing the multiplication and division factors and the final filter. It is thus suitable to run most of the high-performing clocks detailed in section 1.2.

In Fig. 2.2 the main components of the electronic board are highlighted. The electronics is completed by an additional DDS which generates the 80 MHz radiation to drive the single-pass AOM. Finally, a transimpedance amplifier is mounted on a board close to the physics package. The amplifier uses a low input-current noise amplifier (Analog device AD8671) and has a conversion factor of 1.6×10^4 V/A. The noise floor of the amplifier is limited by the Johnson thermal noise of the feedback resistor (at 50 °C).

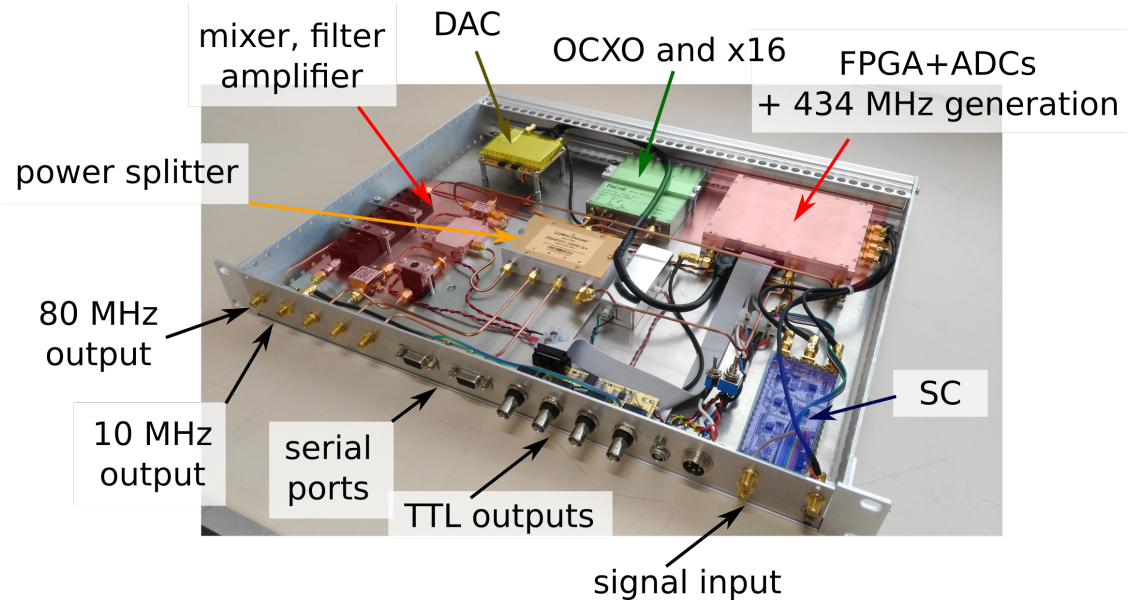

Figure 2.2: Picture of the current electronics package with the main components highlighted. SC: signal conditioning. The box is mountable in a standard 19-inch rack.

2.1.3 Optics package

The only laser source used to operate the clock is a distributed-feedback laser (DFB) [113, 114] from Toptica. It provides around 27 mW at 100 mA of injection current. An optical isolator (Faraday rotator) prevents optical feedback from spurious reflections. A half-waveplate followed by a polarizing beam-splitter select a small fraction of power which is dedicated to the stabilization of the laser frequency

on an external reference cell containing natural rubidium. The details of the frequency lock are given in section 3.2.1. The lock has a low bandwidth (usually below 50 Hz), as the frequency stability mainly influences only the medium-long term.

The acousto-optic modulator, in a single-pass configuration has a double function: firstly, it provides fast attenuation to operate in a pulsed regime. In this sense it acts as a switch with at least 40 dB of attenuation when no RF power is sent to the device. The second purpose is to frequency bridge the frequency of the clock branch. Indeed, the optical transition is red-shifted by the collision of the buffer gas by around 160 MHz in the clock cell, with respect to the reference cell upon which the laser frequency is stabilized (see section 4.1.4). The AOM radiofrequency is provided by a direct-digital synthesizer embedded in the clock electronics, thus its timing is naturally set by the pattern generator.

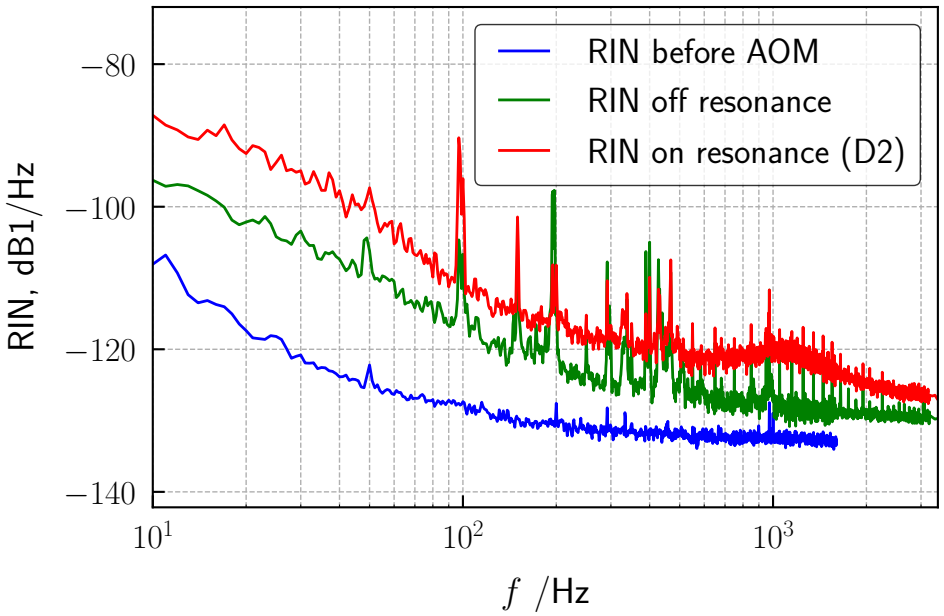

Figure 2.3: Relative intensity noise measured in continuous wave before and after the acousto-optic modulator.

2.1.4 Clock timing and operation

The clock frequency loop is performed by alternatively probing the two sides of the atomic resonance. The resulting signals are subtracted in order to create a suitable error signal (the equivalent to a demodulation for an analog lock-in). The basic clock sequence to probe the resonance is composed by a series of steps. First the atoms are prepared into one of the two clock states by means of a strong

laser pulse. The optical pumping, with the choice of the right power and length, has also the effect of destroying the residual coherence from the previous clock interrogation. Then the clock transition is probed with two Rabi pulses ($\pi/2$) separated by a free-evolution time T, in a Ramsey configuration. The free-evolution time is chosen in such that $T \simeq 1/\gamma_2$, a condition that maximizes the line quality factor. The phase-coherence between the pulses is guaranteed by the fact that only the amplitude of the DDS is set to zero during the free-evolution time, while the phase keeps accumulating. Finally the atomic population is probed by sending a weak laser pulse and looking at the transmitted signal. A detection window is opened in correspondence with the probe pulse and the signal from the photodiode is averaged for a time τ_d. One of the advantages of working in the pulsed regime is the possibility to adjust the pump and probe power independently, while in the CW regime a compromise between the two must be found.

The typical timing used for the current prototype of the POP clock is shown in Fig. 2.4a. The pumping pulse and Rabi pulses duration is 0.4 ms, the free-evolution time $T = 3$ ms and the detection time $\tau_d = 0.15$ ms. The pump power is around 17 mW and the detection power is 700 µW.

The atomic signal S is obtained by integrating the detected photo-current over the detection window τ_d. To get an odd error signal centered at the top of the fringe, the synthesizer frequency ν_0 is modulated with a square wave (with modulation depth ν_m). A demodulated signal is obtained by constructing an error signal $E[2kT_c;\nu_0] = S[2kT_c+1;\nu_0-\nu_m] - S[2kT_c;\nu_0+\nu_m]$. The error signal is available at time $2kT_c$, and thus the maximum rate of correction is $1/(2T_c)$. As we will see later the sampling rate of the atomic signal has an impact on the way the detection noise is transferred into the clock short-term stability. In particular an aliasing process occurs. A signal model theory to understand the noise conversion is developed in the next section.

2.2 Stability budget: short-term contributions

In this section we consider the major contributions to the total short-term stability. The contributions to the stability budget for short timescales come from fundamental quantum noise (such as photon and atomic shot-noise) or from technical noise sources, such as frequency and intensity noise of the laser and microwave fields interacting with the atomic sample. We will see how the latter are in fact predominant in the case of the POP clock. As we are working in a pulsed regime, we need to consider that possible aliasing phenomena may occur. This is well known in the case of the Dick effect for the local oscillator noise, but often not underlined in the case of laser noise. In the following a signal theory model is presented that can be use to predict the contribution to the fractional frequency stability given an arbitrary laser AM spectrum as input. Some of the tools developed in the model

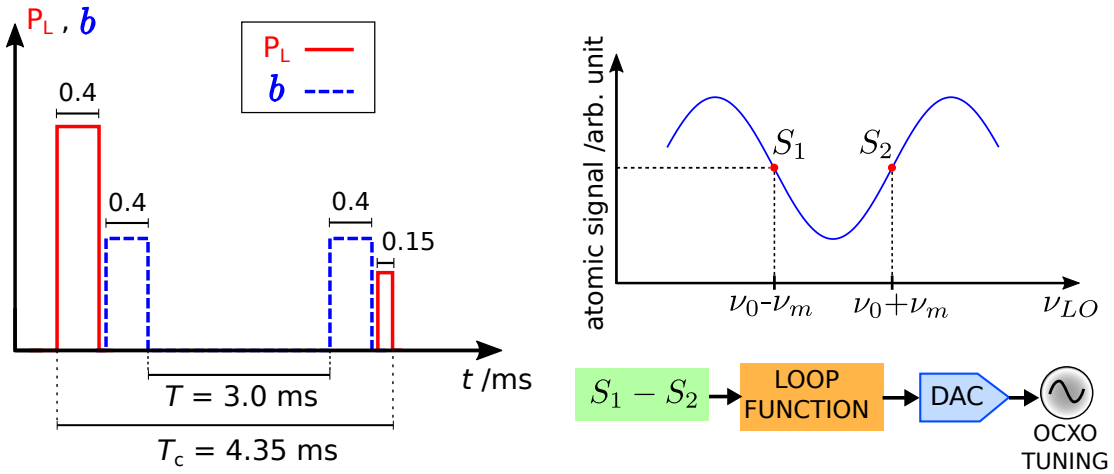

(a) Clock timing. (b) Locking scheme.

Figure 2.4: a) Basic clock sequence to probe one side of the atomic resonance. The output of the sequence is the atomic signal S. b) Scheme of the basic LO frequency loop.

can be applied also for the simpler case of white noise (encountered in the case of photon shot noise and electronic noise). A reliable estimate of the impact of such noise components on the clock performance is useful in the design phase, when a proper laser source is to be chosen. Moreover, to optimize the performance of the clock, it is useful to know the detail of the noise transfer mechanisms.

2.2.1 Laser AM noise - signal theory model

In the pulsed scheme of the POP clock the atomic population at the end of the Ramsey sequence is probed with a weak pulse, performing an absorption measurement. Since there is no noise background cancellation, AM noise present on the probe laser directly adds to the clock signal. Noise on the detected atomic signal is then converted into LO frequency noise by the clock loop itself. The situation is sketched in Fig. 2.5. We will see in the following how AM laser noise during the detection phase can significantly worsen the short-term clock stability and constitute a major technical limitation.

For the determination of the short-term contribution, we are interested in the fast components of the noise spectrum, which might convert into baseband. For simplicity we assume the atomic medium as an ideal absorber, that leaves the noise properties unaltered as the laser propagates through it. Moreover, we focus on the effect of fast laser noise during the detection phase only, as intensity fluctuations at the detector are directly converted into fluctuations of the measured photocurrent.

The validity of these hypothesis will be checked "a posteriori" by means of an experimental test (see section 2.2.1). Not introducing the active medium characteristics makes the description more general and not linked to the particular experimental parameters. The only remark is to remain in a weak probe condition.

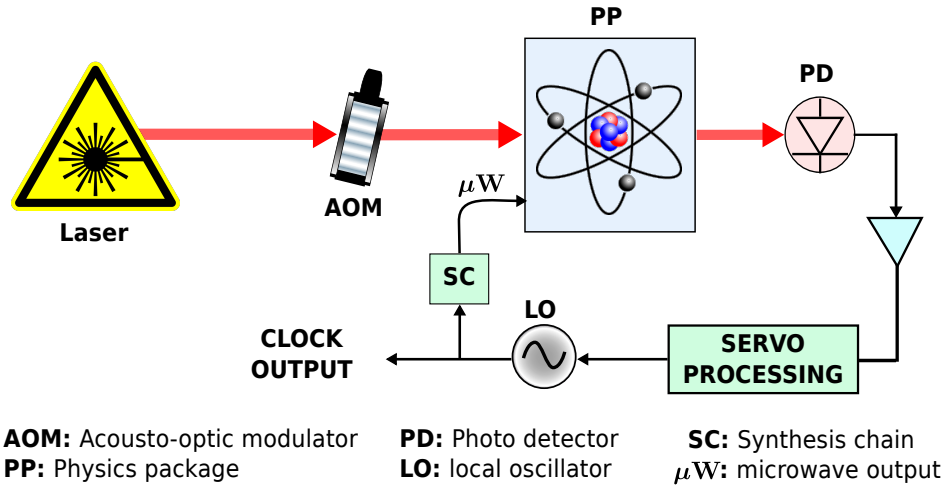

Figure 2.5: Sketch of the detection scheme. Since no differential measurement is implemented laser intensity noise directly affects the clock signal and is transferred to the clock frequency loop.

To understand the noise conversion, it is clearer to analyze the signal processing in time domain. Since usually the laser intensity fluctuation are expressed in term of Power Spectral Density (PSD), it is useful to translate the formalism into the frequency domain. By this means we are able to link the noise PSD of the laser to the PSD of the acquired error signal and from the latter to derive an expression for the clock short-term stability, expressed as Allan deviation.

Time-domain

We start by defining the relative intensity fluctuations of the laser intensity.

$$i(t) = \frac{\delta I(t)}{I_0} \tag{2.1}$$

or, alternatively, $I(t) = [1 + i(t)]I_0$. In (2.1) $i(t)$ is a random process with zero mean, while I_0 is the mean laser intensity of the detection pulse. To simplify the treatment we make the following assumption: the noise properties are the same of the laser continuously running. The pulsing does not alter the noise characteristics and does not introduce additional noise. Moreover the atomic medium is considered as a passive attenuator, which changes the mean intensity of the laser beam, but

the relative noise is preserved. The latter hypothesis is valid only in case of probing with low laser intensity and pumping effect is negligible.

The pulsed operation foresees the acquisition of the atomic signal over a detection window of length τ_d. The signal is commonly averaged over the window duration. The averaging operation is described by the following impulse response function:

$$h_a(t) = \begin{cases} \frac{1}{\tau_d} & \text{for } 0 \leq t \leq \tau_d \\ 0 & \text{elsewhere} \end{cases} \tag{2.2}$$

We can define the fluctuations of the detected signal as the convolution of the impulse response with the input noise:

$$s(t) = h_a(t) * i(t) \tag{2.3}$$

As described in section 2.1.4, the creation of a useful error signal involves the subtraction of two atomic signals obtained with opposite frequency modulation. Two subsequent signals are temporally separated by the clock basic cycle which has duration T_c. This further operation is described by the impulse response function $h_\Delta(t) = \delta(t) - \delta(t - T_c)$. Thus, the fluctuations of the error signal can be expressed as follows:

$$e(t) = h_\Delta(t) * s(t) = s(t) - s(t - T_c) \tag{2.4}$$

Up to this point all operation are conducted on the continuous-time signals. To fully describe the clock operation we also need to introduce a sampling process. Indeed in the actual implementation, the error signal is available as a series of discrete samples taken at the time $t = 2kT_c$, where k is an integer. The sampled error signal is expressed, as in usual signal theory analysis, as:

$$e_\delta(t) = e(t) \times 2T_c \sum_{k=-\infty}^{\infty} \delta\left(t - 2kT_c\right) \tag{2.5}$$

The fluctuations of the sampled error signal are transferred into frequency fluctuations of the local oscillator by the servo control. Since we are interested in the stability of the slaved local oscillator for averaging times longer than the frequency loop time constant ($\tau > \tau_L$), we can avoid to insert the fluctuations in the loop dynamics and simply write:

$$y(t) = -\frac{1}{D_e} e_\delta(t) \tag{2.6}$$

Here $y(t)$ are the fractional frequency fluctuations and D_e is the frequency discriminant, proportional to the absolute atomic frequency and to the slope of the side of the atomic resonance ($D_e = 2\nu_0 D$). All the aforementioned operations are summarized in the block scheme of Fig. 2.6.

If more elaborated averaging operation or another demodulation scheme are used, they can be modeled in the same way by adopting the proper impulse response functions $h(t)$ and $h_\Delta(t)$ respectively. The general signal theory model still holds.

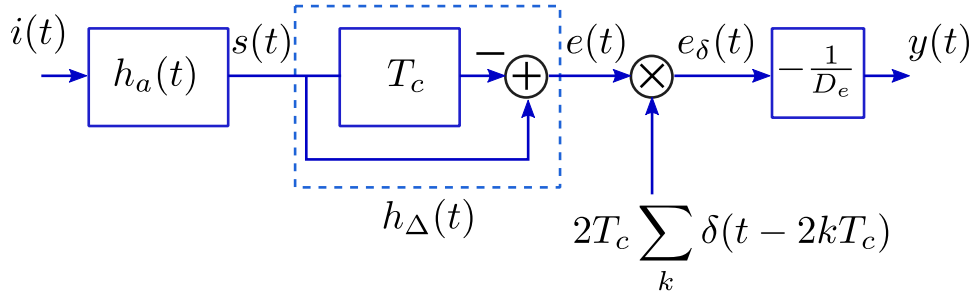

Figure 2.6: Block scheme of the model of noise transfer to the clock stability in time domain.

Frequency-domain

Having highlighted the main functional blocks in the time domain, the passage to the frequency domain is quite straightforward. The relative intensity noise (RIN) is described by the two-sided Power Spectral Density $S_i(f)$. The first two blocks of Fig. 2.6 are linear and time invariant, thus we can write the spectrum of the error signal as:

$$S_e(f) = |H_a(f)H_\Delta(f)|^2 S_i(f) \tag{2.7}$$

where $H_a(f)$ and $H_\Delta(f)$ are the Fourier transform of $h_a(t)$ and $h_\Delta(t)$, respectively. In case of the functions defined in the previous section, we have $|H_a(f)|^2 = \mathrm{sinc}^2(\pi f \tau_d) = \sin^2(\pi f \tau_d)/(\pi f \tau_d)$ and $|H_\Delta(f)|^2 = 4\sin^2(\pi f T_c)$.

The sampling of the signal introduces aliasing, since the clock modulation rate is usually lower than the bandwidth of the noise process [115]. For this reason, noise components at multiples of the error signal sampling rate are converted into baseband. The resulting aliased spectra has the following form [116]:

$$S_{e_\delta}(f) = \sum_k |H_a(f_k)H_\Delta(f_k)|^2 S_i(f_k) \tag{2.8}$$

where we defined $f_k \equiv f - \frac{k}{2T_c}$. The expression (2.8) is a general result, that provides the aliased spectrum of the error signal, and from which the corresponding Allan deviation can be calculated [117]. As we are interested in calculating the clock stability for $\tau >> \tau_L$, we can limit the analysis to the portion of the spectrum at low Fourier frequencies. We can further simplify the expression taking the limit $f \to 0$. In this case $H_\Delta \to 4$ for k odd and is zero elsewhere. The summation can thus be performed taking the value of the spectrum for frequencies that are *odd* multiples of $1/(2T_c)$:

$$S_{e_\delta}(f) \simeq \sum_{k\ \mathrm{odd}} 4 \left| H_a\left(\frac{k}{2T_c}\right)\right|^2 S_i\left(\frac{k}{2T_c}\right) \tag{2.9}$$

This expression does not depend on f, thus the resulting spectrum in the low frequency region tends to be white.

Contribution to the clock stability

The clock Allan variance is evaluated by calculating first the Allan variance of the sampled error signal, and thus scaling it by D_e^2 (see (2.6)). We remind that for a given white noise level h_0 (bilateral) the corresponding Allan variance is $\sigma_y^2(\tau) = \frac{\mathsf{h}_0}{\tau}$ [118], so we have:

$$\sigma_y^2(\tau) = \frac{4}{D_e^2} \sum_{k \text{ odd}} \operatorname{sinc}^2\left(\pi \frac{k}{2T_c}\tau_d\right) S_i\left(\frac{k}{2T_c}\right) \frac{1}{\tau} \tag{2.10}$$

We can derive a simplified version of equation (2.10) in the case of white noise, useful if the laser intensity noise is approximately white in the frequency range of interest and in the case of photon-shot noise and electronic Johnson noise, which are truly white.

We substitute to $S_i(f)$ the constant noise level h_0^i. We assume that the noise bandwidth is higher than the bandwidth of $H_a(f)$ ($B_e = \frac{1}{2\tau_d}$), which acts as a low-pass filter. In this case the sum of (2.10) can be stopped at k_e defined as the odd number closest to $\frac{B_e}{f_s} = \frac{T_c}{\tau_d}$, f_s being the sampling frequency $f_s = \frac{1}{2T_c}$. Therefore, the contribution to the clock stability simplifies to:

$$\sigma_y^2(\tau) = \frac{2}{D_e^2} \frac{T_c}{\tau_d} \mathsf{h}_0^i \frac{1}{\tau} \tag{2.11}$$

Because of the aliasing process, the laser RIN at low frequencies is enhanced by a factor $2\frac{B_e}{f_s} = 2\frac{T_c}{\tau_d}$.

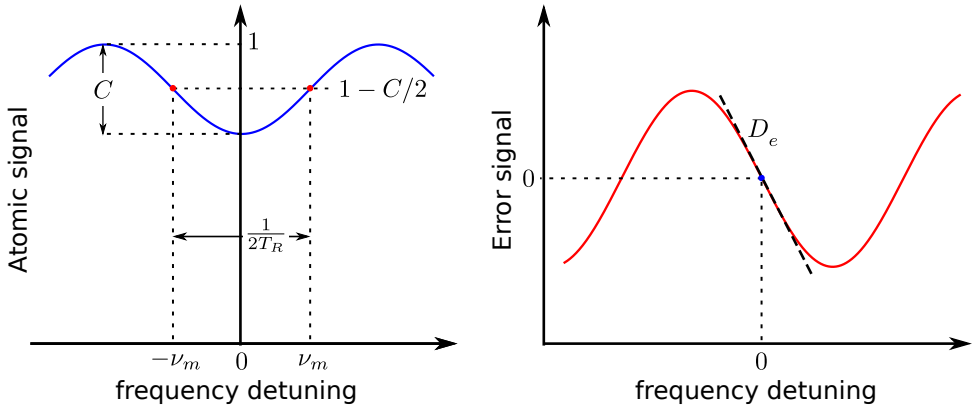

Figure 2.7: Definition of the fringe contrast and shape of the atomic and error signal in the case of the POP clock.

It is to be noted that the model here developed does not make any assumption on the nature of the atomic signal. It makes use of standard signal theory formalism assuming only to be known a priory the general shape of the clock signal and the noise at the input. In particular the slope of the frequency discriminant D_e must be included. Thus the model can be applied to any pulsed clock architecture (in condition of weak probe) where no background noise cancellation is in place, with minor modifications. One notable example is the pulsed CPT clock.

With focus on the POP clock, which is the main object of this dissertation, we finally give an explicit form of D_e in terms of the clock parameters (see also Fig. 2.7 for the definition of the contrast):

$$D_e = \pi \frac{C}{1 - C/2} Q_a \tag{2.12}$$

being C the contrast of the central Ramsey fringe and $Q_a = \nu_0/(2T_R)$ the atomic quality factor. The expression is derived by approximating the central fringes with the function $S(\nu) = 1 - C/2[1 + \cos 2\pi T_R(\nu - \nu_0)]$.

We stress that (2.11) is derived here as a simplified case of the more general result of the model of section 2.2.1, but is consistent with the usual equations encountered in textbooks (e.g. [119, 120]) which use variable notation and are derived with a simpler reasoning and implicitly assume white noise processes. Here we recovered it starting from a more general treatment (for arbitrary noise processes) in the case of a discrete probing of the atomic resonance (a sort of "digital lock-in", typical of the pulsed operation).

Experimental model validation

To validate the signal theory model, and in particular to confirm the fairness of the few assumptions made, we made an experimental test on the POP setup. The experimental conditions are the one of section 2.1.4. Here we just reduced the detection power, to be sure to operate in a weak probe condition (pulse peak power 100 µW). The Ramsey fringes obtained in this condition show a contrast of 27.8 % and an atomic quality factor $Q_a = 4.7 \times 10^7$. The clock cycle T_c is 8.78 ms long, including short pauses between the pulses.

For demonstration purposes the laser RIN entering the physics package has been artificially enhanced by modulating the amplitude of the RF signal that drives the AOM. The noise level is chosen in a way that all other noise contributions are negligible. In this particular situation, we can directly compare the measured clock stability to the stability estimated with the use of the model. Two test cases are considered, which are often encountered in laser sources: white and flicker noise. In Fig. 2.8 the noise levels, as measured before the clock cell, are shown. The white noise level h_0^i is $1.7 \times 10^{-7}\,\mathrm{Hz}^{-1}$, band-limited to 25 kHz and the flicker level h_{-1}^i is 4.8×10^{-6}. In table 2.1 the measured stabilities are compared with the estimates of

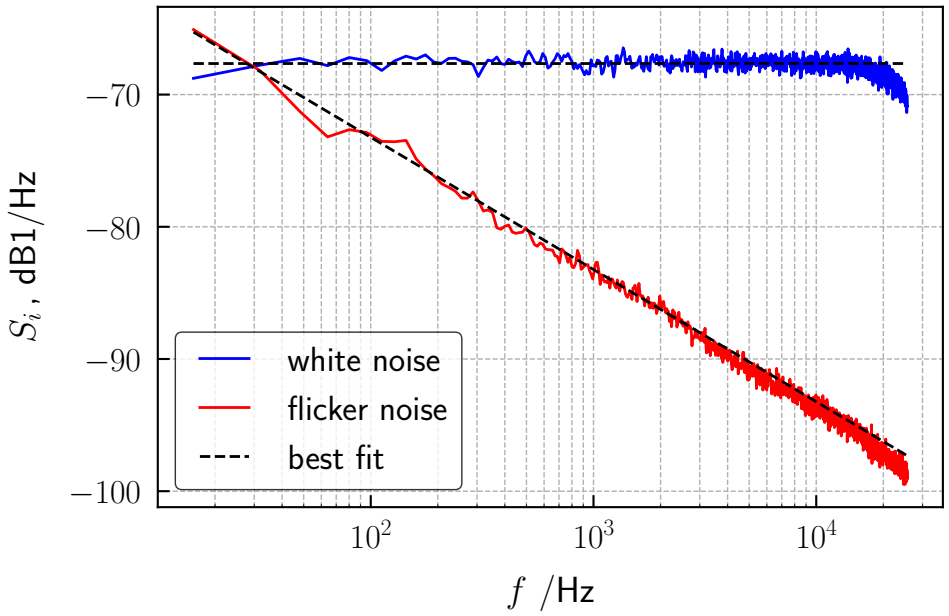

Figure 2.8: Enhanced noise levels used in the in the model validation as measured at the input of the clock cell.

Table 2.1: Stability measurements compared to the estimate from the model

Input noise	Measured ADEV(1 s)	ADEV(1 s) from (2.10)
White noise ($1.7 \times 10^{-7}\,\mathrm{Hz}^{-1}$)	7.0×10^{-11}	6.4×10^{-11}
Flicker noise ($4.8 \times 10^{-6}/f$)	1.4×10^{-11}	1.2×10^{-11}

the model. The model takes as input a best fit of the measured noise level and the available experimental parameters (C, τ_d, T_c, T_R). The results are consistent with the measured stability within 15 %, demonstrating the reliability of the model.

2.2.2 Laser FM-AM conversion

Since the laser pulse used during the detection phase is resonant with the atomic transition, we expect that laser frequency noise would convert into AM noise at the output of the clock cell. Since in operational conditions we need to consider a thick vapor, the theoretical treatment is not straightforward. In fact we have to

deal with non-linear stochastic equations [76, 77]. Moreover the noise conversion is quite dependent on the operational conditions, through physical parameters such input power, atomic density, laser frequency detuning, etc. A proper treatment of the laser-atom interaction, which can be seen as an extension of the model of section 2.2.1, is under development. For the present discussion we can collect some experimental observations obtained with our DFB laser (which has a linewidth of about 2 MHz). In particular we have seen that the phase noise conversion leads to a degradation of the short-term stability of a factor 2 with the laser properly tuned on the minimum of the absorption profile, with comparison to the off-resonant case. A degradation of the stability up to a factor 8 arises with the laser detuned by few tens of MHz. More details are given in section 3.2.3. Here we can observe the effect on the AM noise measured in the continuous regime after the passage through the clock cell for different laser detuning, compared to the noise observed with the laser completely off-resonant (section 2.2.2). We can observe a significant dependence of

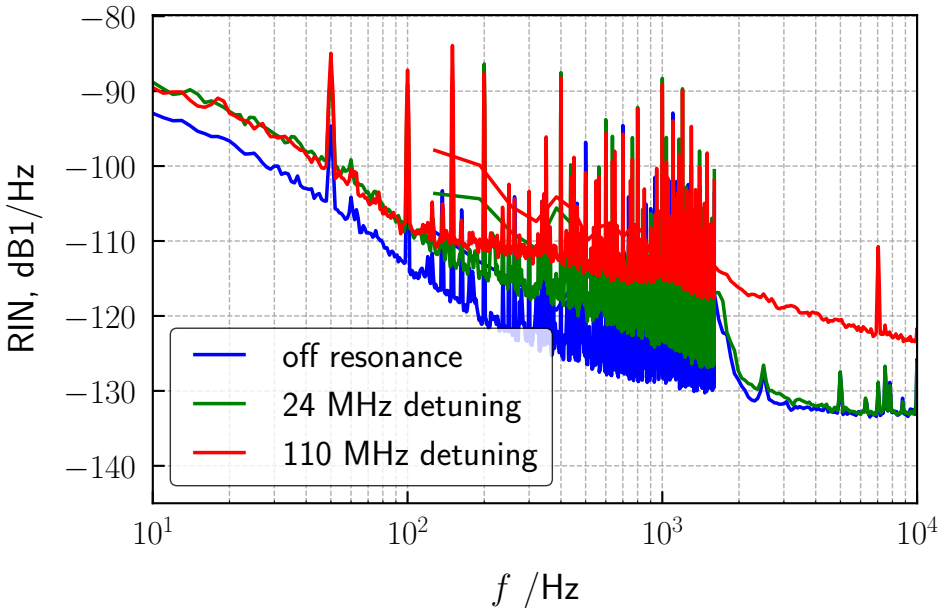

Figure 2.9: RIN measured after the clock cell with laser off resonance and on resonance, with different detuning from the minimum of the buffer-gas-broadened absorption profile.

the noise level on the laser detuning. It is clear how the proper frequency setpoint is rather critical to achieve the best short-term stability. This point will be addressed in section 3.2.3.

2.2.3 Laser photon shot-noise

The shot-noise contribution comes from the quantum properties of light. The granular nature of photons gives rise to a Poissonian statistic for the number of photons N reaching the photodetector, with a variance that scales as N. The Poissonian statistics is transferred to the statistic of the photocurrent, for an ideal photodetector. In case of inefficiency, we can still assume the statistic to be maintained, with the number of photo-electrons being the number of photons multiplied by the coefficient $\eta < 1$. In terms of optical power and photocurrent, we can express the mean photocurrent during the detection phase as:

$$\langle I \rangle = W \langle P_{det} \rangle \tag{2.13}$$

Where I is the photocurrent, W the spectral responsivity of the detector (expressed in A/W) and P_{det} the optical power incident on the detector. The relative noise Power Spectral Density due to the current shot noise is thus:

$$S_{shot} = \frac{2e}{\langle I \rangle} = \frac{2e}{W \langle P_{det} \rangle} \tag{2.14}$$

And the contribution to the short-term stability, following (2.11) and (2.12), becomes:

$$\sigma_y^2(\tau) = \frac{2}{D_e^2} \frac{T_c}{\tau_d} S_{shot} \frac{1}{\tau} = \frac{(1 - C/2)^2}{(\pi C Q_a)^2} \frac{2T_c}{\tau_d} S_{shot} \frac{1}{\tau} \tag{2.15}$$

For a typical power level of 25 µW at the detector, the shot-noise contribution is estimated at the level of $3 \times 10^{-14}\, \tau^{-1/2}$.

2.2.4 Detector electronic noise

The detector noise is designed and experimentally confirmed to be limited by the Johnson thermal noise of the feedback resistor (R_f) of the trans-impedance amplifier (in the spectral range of interest for the clock). Other sources, like the input current noise of the amplifier or photodiode noise are negligible). The contribution from the thermal-noise is white and is calculated with the well known expression $S_{th} = 4 k_B T R_f$, where k_B is the Boltzmann constant and T the absolute temperature of the resistor. The contribution to the clock frequency stability is again calculated with the use of (2.11):

$$\sigma_y^2(\tau) = \frac{2}{D_e^2} \frac{T_c}{\tau_d} S_{th} \frac{1}{\tau} = \frac{(1 - C/2)^2}{(\pi C Q_a)^2} \frac{2T_c}{\tau_d} S_{th} \frac{1}{\tau} \tag{2.16}$$

With the typical signals level encountered in the operational condition, we obtain an estimated contribution from the detection electronic noise on the short-term stability of $2 \times 10^{-14}\, \tau^{-1/2}$. This noise contribution is lower than the shot-noise by design.

2.2.5 Local oscillator phase noise (Dick-effect)

The contribution of the free-running local oscillator noise when dealing with a pulsed operation has been extensively treated in the literature, first in the case of the cesium fountain standards [121–123] and later for the optical frequency standards [124, 125] and CPT standards [126]. The POP clock shares the same interrogation method of the cesium fountain, thus the same formalism applies. The formula to calculate the short-term stability contribution, starting from the fractional frequency noise spectrum of the microwave synthesizer $S_y^{LO}(f)$, is the following [122]:

$$\sigma_y(\tau)^2 = \sum_k \mathrm{sinc}^2\left(k\pi\frac{T}{T_c}\right) S_y^{LO}(k/T_c)\,\tau^{-1} \tag{2.17}$$

where as usual T_c is the clock cycle (single detection sequence) and $\mathrm{sinc}(x) = \sin(x)/(x)$. Expression (2.17) is indeed a simplified case, which assumes a sensitivity function equal to one during the free-evolution time and zero elsewhere. This approximation is valid in the limit of short Rabi pulse, compared to the free-evolution time ($t_1 << T$). In the more general case we should use the complete sensitivity function and replace $\mathrm{sinc}(k, T, T_c)$ with [122]:

$$\begin{aligned} f(k, T, T_c, t_1) &= \frac{2T_c}{f_0\pi k\left[T_c^2 - (4kt_1)^2\right]}\left\{4kt_1\cos\left(\frac{\pi(kT+2kt_1)}{T_c}\right) + T_c\sin\left(\frac{k\pi T}{T_c}\right)\right\} \\ f_0(T, T_c, t_1) &= \frac{4}{T_c}\left(T/2 + 2t_1/\pi\right) \end{aligned} \tag{2.18}$$

Moreover, equation (2.17) needs a cut-off frequency at which the summation is stopped, otherwise it would lead to a divergent result. The cut-off is given by the Rabi pulses length. In fact, the noise of the free-running oscillator is averaged out during the Rabi pulses. Mathematically, this is equivalent to multiply the simplified transfer function of (2.17) by a box filter $\mathrm{sinc}^2(k\pi t_1)$, or to stop the summation to an integer close to $k_e = 1/(2t_1)$. To clarify this concept, in Fig. 2.10 we compare the two transfer functions (squared). From the plot it is clear that the approximate transfer function is less selective than the complete one. Indeed, the use of the simplified transfer function leads to an overestimation of the Dick effect contribution by about 20 %. We can conclude that the simplified equation can be used when a conservative estimation is desired.

In Fig. 2.11 the phase noise of the microwave synthesis chain is presented. From the plot we can also compare the phase noise of the output at 6.8 GHz with the phase noise of the OCXO ideally multiplied. From this comparison we notice that residual phase noise introduced by the frequency multiplication stages is very low as the two curves basically overlap. With such phase noise properties and with the use of (2.17) we estimate a Dick-effect contribution of $2\times10^{-14}\,\tau^{-1/2}$, negligible compared to the previously examined contributions.

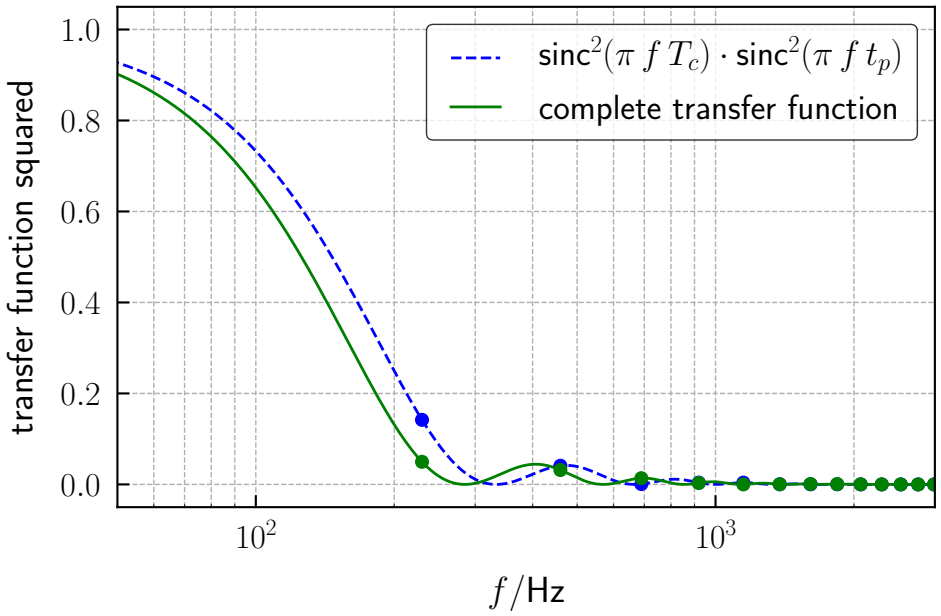

Figure 2.10: Comparison between the approximate transfer function (dashed line) and the complete transfer function (continuous line), for the calculation of the Dick-effect term. The dots correspond to $f = kT_c$. Timings are $T_c = 4.35\,\mathrm{ms}$, $T = 3.0\,\mathrm{ms}$, $t_1 = 0.4\,\mathrm{ms}$ in both cases.

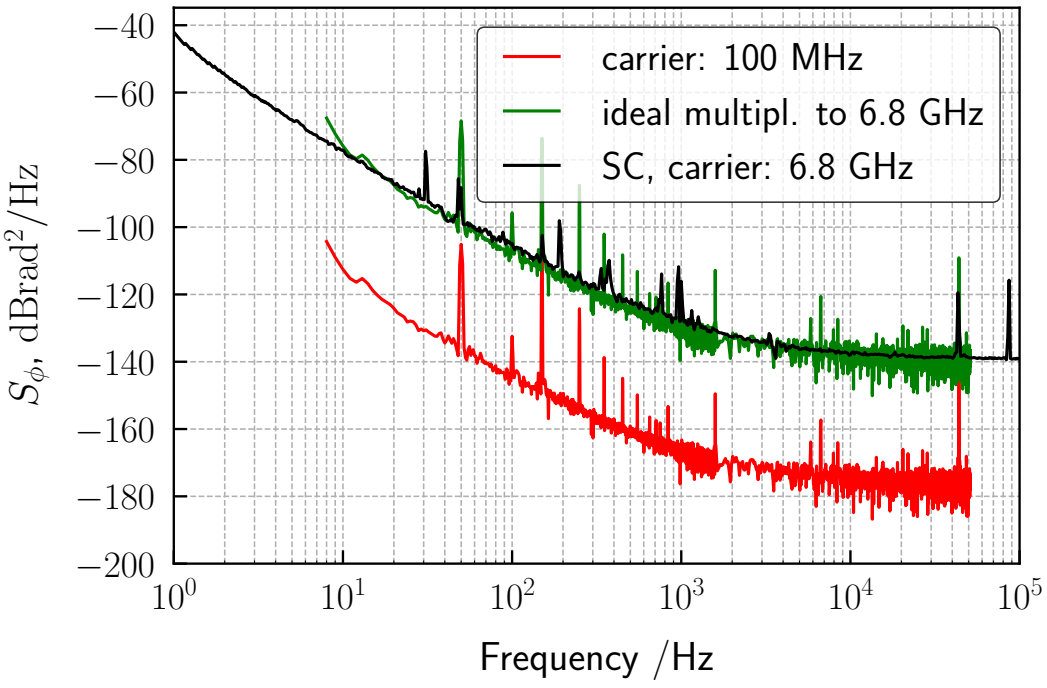

Figure 2.11: Phase noise levels for the synthesis chain. Black: Phase noise measured at 6.8 GHz. Red curve: Phase noise of the Quartz oscillator (at 100 MHz, red). Green: 100 MHz noise ideally multiplied at 6.8 GHz.

2.3 Long-term: environmental sensitivities

The stability of many environmental parameters start to play a role particularly for averaging times above 1000 s. The physical mechanism by which these parameters impact the clock frequency stability are different. A good recap of such mechanisms can be found for example in [110] and [127]. Reference [128] also give some experimental characterization of the long-term sensitivities for the POP clock. Reference [129] analyzes some long-term contributions comparing the pulsed and CW operation on two high-performing setups.

Conceptually, we can divide the effects into two categories: some parameters directly affect the atomic reference, inducing a frequency shift on the clock transition. Other parameters variations produce a shift of the observed frequency because of inhomogeneities in the active region. Given the distribution of the atomic sample in space, asymmetries in the physical parameters across the vapor cell can introduce additional environmental sensitivity. In the latter case it is more difficult to give an a-priori evaluation of the expected sensitivity, as the nature of the gradients is often not known. In both cases, the frequency sensitivity often depend on the operational conditions and the sensitivity coefficients experimentally evaluated by varying the parameter under study around the working point.

In this section we will focus on some of the most critical parameters and recap the physical phenomena which determine the relative clock sensitivity.

2.3.1 Sensitivity to thermal fluctuations

The main sensitivity to thermal fluctuations has its physical origin in the temperature dependence of the buffer-gas collisional shift (see section 4.1.4 for more details). The sensitivity induced by single buffer gas species can be of the order of $1 \times 10^{-9}\,\mathrm{K}^{-1}$. However, this coefficient can be constrained below $1 \times 10^{-11}\,\mathrm{K}^{-1}$ with a proper 2-species mixture [130]. In fact, the use of two inert gases with opposite linear thermal coefficient produces an inversion point of the shift at a specific temperature. By working around this specific operational setpoint, a much smaller quadratic dependence on the gas temperature is observed and a thermal control below 1 mK is sufficient to guarantee good long-term performances.

Another effect that in some cases can completely mask the previous phenomenon, is buffer gas migration between the cell body and the pinch-off stem (which usually lies outside of the cavity volume) [107]. In this case we have two connected gas reservoirs. If the temperature difference between the two varies, a gas density variation takes place as well. The clock frequency becomes thus sensitive to the temperature difference between the cell body and the end tip of the stem.

Changes in the stem or cavity temperature can also lead to a variation of the alkali vapor density. Such variation leads to a temperature dependent shift via spin-exchange collisions [131]. Usually this terms is of the order of $1 \times 10^{-12}\,\mathrm{K}^{-1}$,

thus smaller than the buffer gas contributions.

Finally, temperature can also affect the clock frequency via the cavity pulling effect or by changing the coupling efficiency of the microwave feed to the cavity. Since these effects scale proportionally to the cavity quality factor, they can be mitigated in the POP clock with optical detection, where such parameter can be set to a low value (< 500) by design [70, 132].

2.3.2 Sensitivity to microwave amplitude fluctuations

The stability of the microwave field parameters is also a factor that can potentially limit the medium-long term stability. As already noted, one mechanism that can lead to a dependence of the clock frequency to the amplitude of the magnetic field is the spatial dependence of the magnetic field over the active volume. If the Rabi frequency $b(\vec{r})$ varies over the atomic sample then the position of the central Ramsey fringe, detected as a global absorption signal, can acquire a dependence on the average field amplitude.

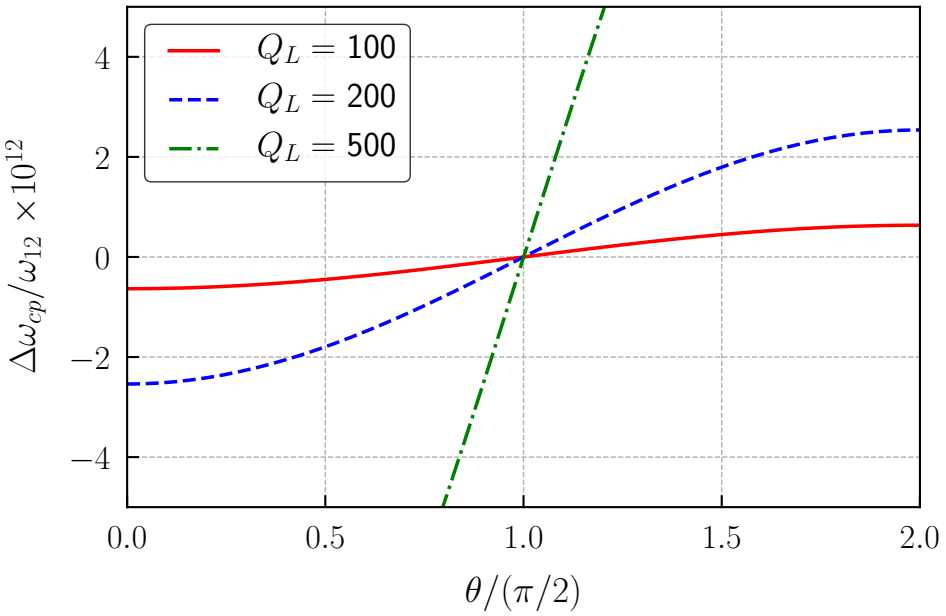

Figure 2.12: Computed cavity-pulling shift as a function of the Rabi pulse area for three different quality factors and fixed cavity detuning ($\Delta\nu_C = 500\,\mathrm{kHz}$)

Another effect which influences the clock transition is cavity-pulling. This effect, for the POP clock, mainly takes place during the free-evolution time. There, the atoms feel the effect of the magnetic field emitted by the atomic coherence and sustained by the microwave cavity. If the cavity is detuned with respect to

the atomic frequency, the magnetic field will induce a phase shift on the atomic coherence. This will in turn reflect on a shift of the central Ramsey fringe. For this reason, a good stability of the cavity dimension through thermal control is needed to ensure a stable cavity detuning [70].

The cavity pulling introduces also an additional dependence on the microwave field amplitude, through the Rabi pulse area θ. In Fig. 2.12 the cavity-pulling shift is plotted as a function of the pulse area for different cavity quality factors and fixed cavity detuning ($\Delta\nu_C = 500\,\mathrm{kHz}$) using the formalism of [106]. In such calculation no inhomogeneities in the field amplitude were included. We can notice that the shift is linear close to the working point $\theta = \pi/2$.

In [133] a more detailed treatment concerning the various cavity parameters affecting the cavity-pulling is given. There a substantial improvement in the medium-term stability is also reported by implementing an active stabilization of the microwave pulses amplitude (see also section 3.1).

2.3.3 Sensitivity to laser power and frequency fluctuations

As noted in section 1.2.3, for the POP clock the sensitivity to laser power fluctuations is much reduced compared to other laser techniques, since the microwave clock transition is probed in absence of light. However, the sensitivity to power fluctuations can still limit the long-term, as the global power coefficient $\alpha_{LS} = (\Delta\nu/\nu_0)/(\Delta P_L/P_L)$ usually lies in the range $5 \times 10^{-14}\,\%^{-1}$ to $5 \times 10^{-13}\,\%^{-1}$. At the same time, the sensitivity to laser frequency fluctuations is reported in the range $2 \times 10^{-14}\,\mathrm{MHz}^{-1}$ to $3 \times 10^{-13}\,\mathrm{MHz}^{-1}$. The exact values of these two parameters depend on the particular implementation and possible nonidealities of technical components. In [128] a different value of α_{LS} is reported as a function of the laser frequency locking point, revealing an interplay between the spectral properties and the sensitivity to power fluctuations. Since there is some degree of freedom on the choice of the laser frequency locking point, an optimal working point can be identified to minimize such dependency.

The physical mechanism which can lead to a residual dependence of the clock frequency on laser power are the following:

- Residual leakage of laser light during the clock interrogation, due to non ideal power switches. Some residual power leaking into the system re-introduces power and frequency dependent light-shift.

- Residual coherence from the previous clock cycles. The pumping pulse strongly suppresses the hyperfine coherence between subsequent clock interrogations [106]. However, given also the strong absorption from the thick vapor which limits the pumping efficiency, a residual phase shift dependent on the laser pump power can persist.

- Spatial inhomogeneities of the microwave and laser field amplitudes create a not uniform atomic population. The detected clock signal is thus the result of a weighted average across the active volume. Varying pump and detection powers lead to interrogate the atomic sample with different weights, in turn inducing a change in the detected signal. Given the physical origin, the observed shift in the clock frequency is called "position-shift".

The first two points can be tackled with a careful experimental design, while some degree of inhomogeneity, at least in the propagation axis of the beam, is unavoidable. In fact the laser power changes exponentially in this direction due to absorption in the thick atomic vapor.

Chapter 3

Advanced locking techniques

The stabilization of many physical parameters involved in the clock operation, like laser frequency and microwave intensity, is of critical importance to ensure good long-term performances. The effect on frequency stability is the result of the clock's intrinsic sensitivity to a variation of a parameter multiplied by the absolute variation of that parameter at a certain timescale. The naive approach to improve the performances of the clock is to stabilize the physical parameter to an external reference. Sometimes this is the only way and has proven to be effective. There are cases when an external stabilization is not easily achieved or (since the goal of vapor cell clocks is to be reliable and compact) is not desirable, as it may add extra complexity to the system.

Recently alternative approaches have been developed. The first approach goes in the direction of reducing the clock sensitivity to environmental parameters, by adopting alternative interrogation schemes such as the so-called "hyper-Ramsey" [134, 135] or the more general "autobalanced-Ramsey" [31, 101, 102]. The second approach is to stabilize the physical parameter by extracting additional information from the clock spectroscopic signal (apart from the frequency difference between the local oscillator and the atomic resonance as in usual operation). This approach has been demonstrated to be effective in the case of the stabilization of the amplitude of the LO microwave field [133] in the POP experiment. In this chapter we will recall the basic principles of the latter algorithm, relating it to other two proposed methods to stabilize the pump/probe laser frequency using the clock signal instead of an external reference cell.

3.1 Microwave amplitude stabilization using the clock signal

As noted in section 2.3.2 the sensitivity of the POP clock to fluctuations of the microwave field amplitude can be a concern to achieve good long-term behavior. Given a sensitivity of the clock of around $5 \times 10^{-14}/\%$ [32] and a typical relative fluctuation of the field amplitude of about $0.2\,\%$ at one day of averaging time, an active stabilization of this parameter is needed to reach the 10^{-15} region. Such stabilization could be implemented by referencing the output of the microwave synthesizer to a stable voltage reference. However, this would increase the hardware complexity and we would have to rely on the stability of additional components. Moreover, no assurance is provided on the stability of the delivery system (microwave cables and coupling to the cavity).

An alternate way to achieve an active stabilization is provided by the clock signal itself. In the following section, an algorithm to perform the stabilization by exploiting the symmetries of the atomic signal is described. It is based on a double modulation of the amplitude and frequency of the LO field and a double digital lock-in. Notably, the method requires no substantial modifications in the existing clock hardware.

3.1.1 Rabi oscillations: a tool to stabilize the microwave field amplitude

In the Ramsey interrogation scheme, the important parameter to be dealt with is the microwave pulse area $\theta = bt_1$. Since the timing of the pattern generator is derived directly from the OCXO, t_1 is at least 2 orders of magnitude stabler than the pulse peak amplitude b [136]. For this reason, the fluctuations of the pulse area are dominated by the field amplitude instability, and we will consider the two quantities interchangeably in the present discussion (only a multiplicative factor links the two quantities, but the relative stability is the same).

To understand how the clock signal can be used as a tool to stabilize the LO field amplitude to a stable setpoint, it is useful to look at the dependence of such a signal on the pulse area θ. In Fig. 3.1 the maximum of the absorption signal detected after the clock cell (i.e. the top of the Ramsey fringe) is plotted as a function of this parameter. The observed behavior derives from the well known Rabi oscillations [50]. In the same picture, the usual Ramsey scan (absorption signal as a function of the LO frequency) is shown, with fixed pulse area $\theta = \pi/2$. The usual operation of the clock is indeed around $\theta = \pi/2$, which is the condition that maximizes the fringe contrast. Around this setpoint, the absorption signal is symmetric in the two variables and presents a minimum for both. We can thus think of performing a double modulation of the LO frequency and amplitude and actively stabilize both

parameters directly on the absorption signal. The picture is even clearer if we look

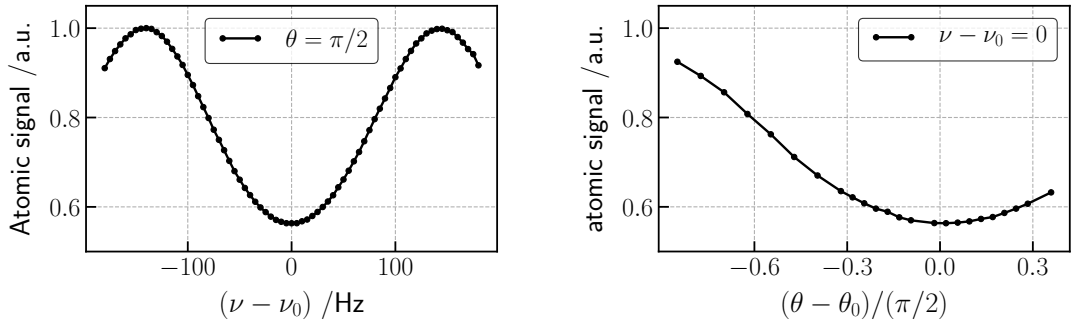

(a) Atomic signal as a function of microwave detuning (at fixed pulse area θ).

(b) Atomic signal as a function of the pulse area θ (at fixed microwave detuning).

Figure 3.1: Atomic signal as a function of LO amplitude (at fixed microwave detuning) compared to the atomic signal as a function of microwave detuning (at fixed amplitude). Both curves are normalized to the maximum signal level (corresponding to the top of the fringes with maximum contrast).

at the experimental fringes in the 2D space of the parameters (Fig. 3.2). Around the operational setpoint, the signal can be approximated as a paraboloid, shallower in the pulse area direction and steeper in the microwave detuning direction. In the next section, the details about the algorithm to perform the double stabilization are given.

3.1.2 Algorithm and experimental realization

The algorithm to stabilize the microwave field amplitude is a natural extension of the usual clock operation described in section 2.1.4. In the following, for simplicity, we will drop the time dependence of the signal. We will assume that every step, required to obtain the atomic signal S_k, is the result of a basic clock sequence of length T_c. The extended algorithm foresees four steps, detailed in table 3.1. During these steps, the LO frequency and amplitude are dithered with modulation depth b_m and ν_m respectively. The modulation scheme is also sketched in Fig. 3.3. The four output of the sequence are combined to generate two error signals, one for each loop:

$$E_n^{\nu} = (S_{4,n} + S_{2,n}) - (S_{3,n} + S_{1,n}) \tag{3.1}$$

$$E_n^{b} = (S_{4,n} + S_{3,n}) - (S_{2,n} + S_{1,n}) \tag{3.2}$$

The corresponding corrections are computed by the controller. A proportional-integrative controller can be implemented. The parameters of the loop are chosen

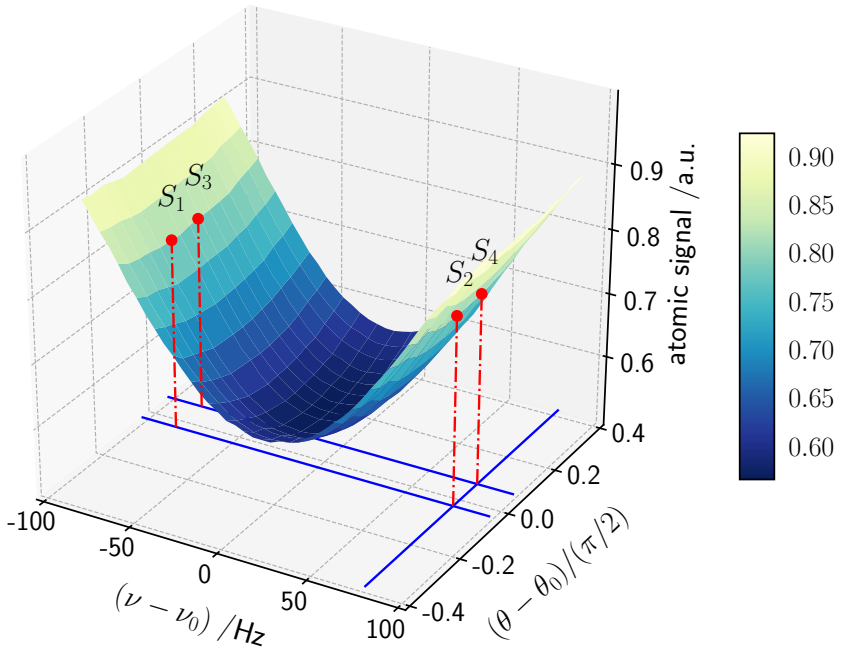

Figure 3.2: Clock signal as a function of both microwave detuning and Rabi pulses area.

Table 3.1: n-th sequence to extract the two error signals.

	microwave frequency	microwave pulse amplitude	Atomic signal
step 1	$\nu_{0,n} - \nu_m$	$b_{0,n} - b_m$	$S_{1,n}$
step 2	$\nu_{0,n} + \nu_m$	$b_{0,n} - b_m$	$S_{2,n}$
step 3	$\nu_{0,n} - \nu_m$	$b_{0,n} + b_m$	$S_{3,n}$
step 4	$\nu_{0,n} + \nu_m$	$b_{0,n} + b_m$	$S_{4,n}$

not to degrade the main frequency loop. For this reason ν_m is chosen to be at half-width-half-maximum of the central fringe, a condition that maximizes the error signal slope. At the same time, the gain of the frequency control loop is kept as high as possible, with a time constant of the order of 100 ms. Conversely, b_m is

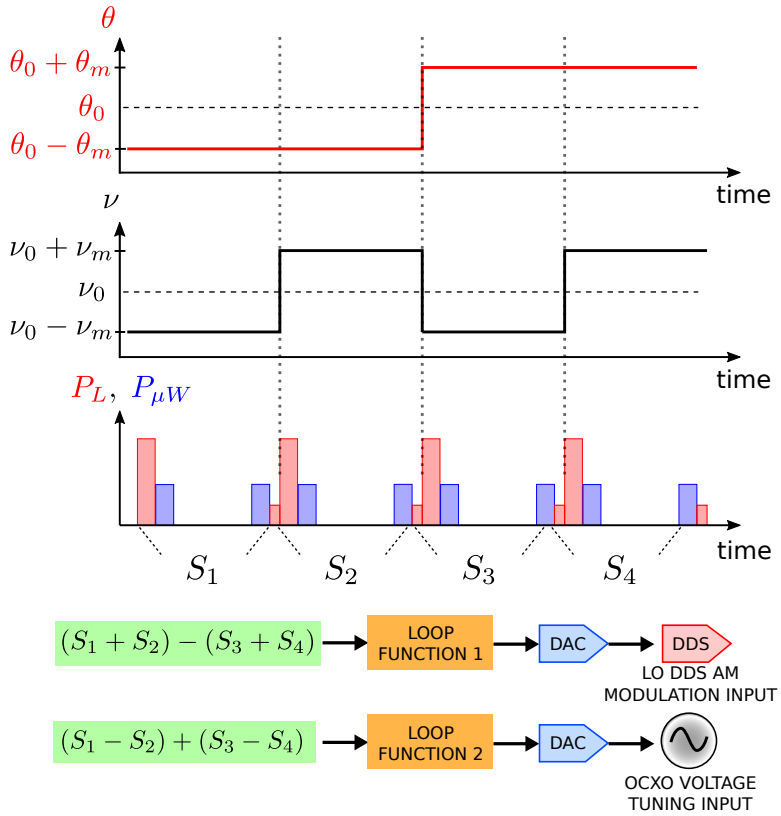

Figure 3.3: Basic sequence of the double-modulation loop. Two error signals are generated as the proper linear combination of the resulting clock signals.

kept as low as possible, not to perturb the frequency stability. Clearly, a trade-off for having sufficient sensitivity to amplitude variations must be chosen. The low sensitivity to amplitude variations, dictated by the shallower minimum and by the small modulation depth, is compensated by a long time-constant of the loop (around 10 s). During this time the error signal is accumulated and the noise is reduced. Such a slow time-constant is possible because of the following facts: the short-term stability of the synthesis chain is usually rather good, while random noise degrades the medium long-term. Moreover, the clock stability is higher at low averaging time. Thus the clock stability is affected by LO amplitude fluctuations only for averaging times longer than 1000 s.

In our experimental setup the LO amplitude modulation b_m is achieved by changing the numerical amplitude of the synthesis chain DDS which in turn sets the amplitude at the amplitude of the synthesizer. The actuator, on the other hand, is implemented by tuning the full-scale current of the same DDS. the tuning is performed through a high-resolution DAC. The dynamic range of the applied correction is $\pm 15\%$ of the total amplitude, while the resolution is around 5×10^{-6}

[137].

It is to be noted that the proposed algorithm does not increase the short-term contribution coming from the Dick-effect. Indeed, the frequency of the LO is compared to the atomic frequency at each step and all the retrieved information is used to stabilize the LO frequency. In other words, what is important for the Dick-effect contribution is the duty cycle of the single basic step, i.e. the ratio between the Ramsey time and T_c. This ratio is not changed in the current implementation.

3.1.3 Experimental validation

In this section, we validate the ability of the proposed algorithm to detect synthesizer output amplitude variations and correct for them. With a modulation depth equal to 5 %, we observed a well defined odd error signal centered around $\theta_0 = \pi/2$ as a function of the pulse area θ. The magnitude of the discriminator slope is given by two factors: the sharpness of the Rabi oscillations peak around $\pi/2$ and the amplitude modulation depth b_m. Well defined Rabi oscillations have been observed for a loaded Q_L as low as 100, therefore the proposed method is suitable to common cavity-cell arrangements [14, 138].

Another way to validate the characteristics of the stabilization loop is to analyze the in-loop response when a step amplitude change is purposely introduced. Qualitative analysis can be made on the effectiveness of the control to detect and correct for amplitude variation. Moreover, the loop bandwidth can be experimentally estimated and adjusted. In Fig. 3.4 the error signal E^b and the calculated correction C^b are plotted in the case where a sudden negative step-change in the microwave amplitude is introduced. In the same figure, the corresponding frequency variation is also shown. The amplitude step induces a frequency jump of 4×10^{-12} in the clock frequency that is recovered by the loop with a time constant $\tau_L = 25\,\mathrm{s}$. Since we cannot directly monitor the stability of the field amplitude in closed loop, we can only estimate the expected gain of the controller from the loop parameters. In case the loop is implemented with a simple first-order integrator, in the frequency domain, the LO AM power spectral density is reduced by a factor $(f/B_L)^2$, where $B_L = \frac{1}{2\pi\tau_L}$ is the bandwidth of the loop. In terms of Allan deviation, the expected improvement in the stability of the field amplitude is $k\frac{\tau_L}{\tau}$, where k is a multiplicative constant that depends on the noise type and equals $\sqrt{3}$ in case of random walk. Since, as already noted, the amplitude fluctuations of the synthesis chain output start to play a role after 1000 s, we usually maintain a bandwidth of few mHz, which is easily reached with a small modulation depth. In these operational conditions, the main frequency loop performances are not affected.

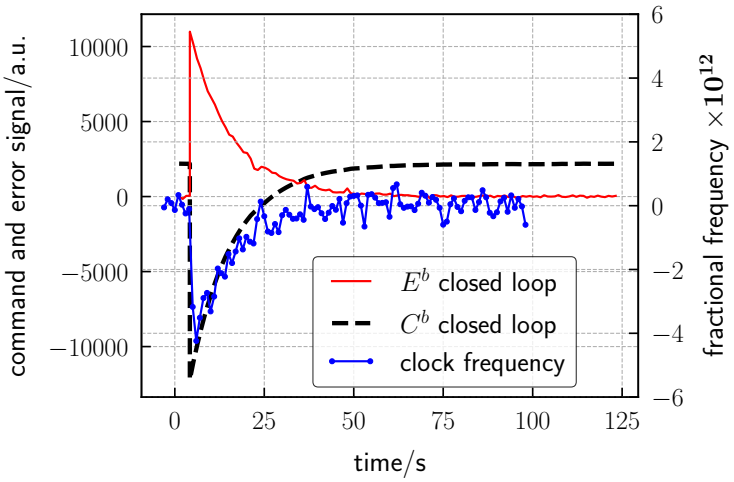

Figure 3.4: In-loop error signal E^b (continuous red line) and applied correction C^b (dashed line) as a response to an arbitrary step-change in the LO amplitude (left y-axis). Fractional frequency variation synchronously acquired (right y-axis, blue dotted line).

Impact on the medium-term performances

In this section, we will show the potential of the method by looking at the medium-term performances obtained in the case of our POP clock prototype. In particular, two long measurements (of a few days each) were taken sequentially. All the experimental parameters are the same in the two cases. The only difference is the usage of the microwave amplitude stabilization loop. The frequency modulation depth is $\nu_m = 80\,\text{Hz}$ and the microwave amplitude modulation depth $b_m = 0.05\ b_0$. The laser power levels and the basic clock sequence are the ones detailed in section 2.1.4. The cavity quality factor is around 500 and the cavity detuning is of the order of -1 MHz. The POP clock was measured against a reference oscillator, which is a composed of a BVA quartz phase-locked to an active hydrogen maser. Between the two measurements, we reduced the time constant of the phase-lock loop (from 3 s to 100 ms), to improve the frequency stability of the reference. As we will see later, this change has an impact only in the short-term stability evaluation, thus it is not of concern for the comparison.

In Fig. 3.5, frequency data of two long-run measurements are presented. In the upper trace no active control on the field amplitude is performed ("open-loop" in the following). In the "closed-loop" case, the microwave field amplitude was actively stabilized as described in section 3.1.2. A linear drift is assumed and calculated as a best fit in the two cases (red thick line). It is around -4×10^{-14}/day in the open-loop measurement, while after applying the microwave amplitude stabilization, it

remains at the level of -8×10^{-15}/day over more than ten days. It is then significantly reduced if compared to the previous measurement. In Fig. 3.6, the clock

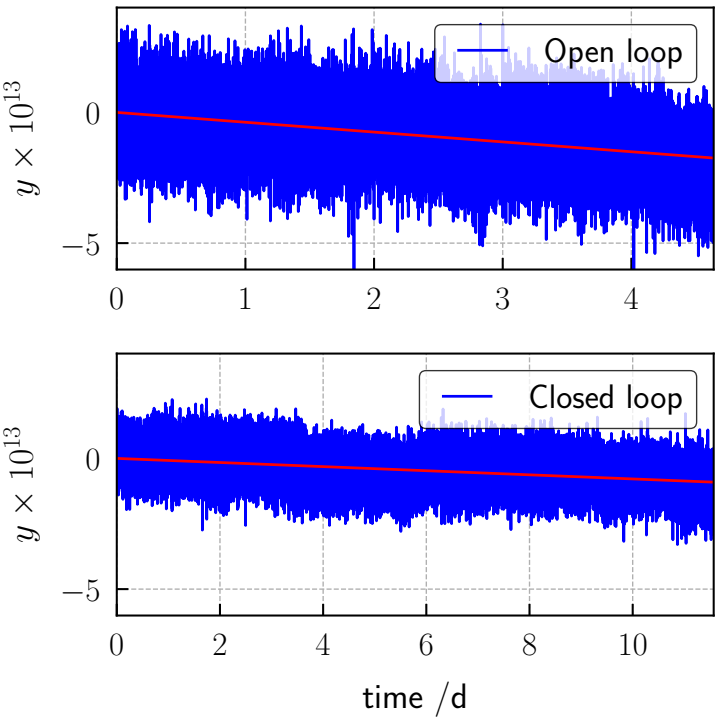

Figure 3.5: Frequency data of long-run measurements with the microwave field amplitude not stabilized (upper trace, "open loop") and with the active stabilization active (lower trace, "closed loop"). Both data sets are presented with no drift removal. The drift is shown as the (red) trend line.

overlapping Allan deviations for the same dataset are presented (no drift removed). The bump at 20 s in the first case is due to the reference, while the short-term in the second case is representative of the rubidium clock only, as the reference instability was brought to a lower level. Regarding the effect of the stabilization on the long-term performances, a significant improvement around averaging times of 10^4 s and longer can be noticed. Looking at the trend lines representing the drift contributions, we can observe that in closed loop there is an additional instability contribution, apart that coming from the linear drift. We attribute that to other sources of long-term instabilities that show up as the microwave amplitude contribution is reduced. For example in this set-up a temperature instability at cell location of 100 µK at 2×10^5 s can lead to a contribution as large as 2×10^{-14} in fractional frequency stability [107]. Concerning the drift reduction, when thermal effects directly affecting the physical package are properly treated, we expect the

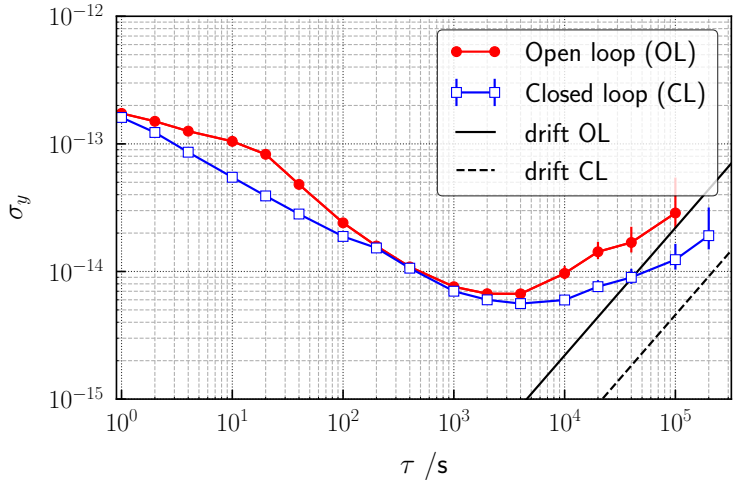

Figure 3.6: Overlapping Allan deviation for the datasets of Fig. 3.5. Measurement bandwidth $f_h = 0.5\,\mathrm{Hz}$. No drift-removal. The calculated drift contributions are shown as trend lines.

instability contribution from the applied microwave field to be the leading term for a wide range of cavity Q and detuning. By stabilizing the pulse amplitude, the residual sensitivity to cavity pulling comes mainly from the slow change rate of the cavity quality factor. This should keep the cavity pulling contribution to the frequency instability in the 10^{-15} region for the usual experimental conditions.

3.2 Laser frequency locking using the clock cell

In this section two alternative approaches to lock the laser frequency using clock cell spectroscopy are presented. The first method makes use of the buffer-gas broadened profile as a frequency reference. The use of such a broad profile is made possible by two factors: 1) the low-noise electronics already implemented for the microwave transition detection; 2) the intrinsic low sensitivity of the POP scheme to laser frequency fluctuations compared to the other vapor cell clock architectures (see section 2.3). Indeed the use of a broader resonance allows for a wider capture range at the expense of lower locking bandwidth. As further discussed in sections 3.2.2 and 3.2.3, the POP scheme allows for a small locking bandwidth while increasing the capture range improves the robustness of the system. More importantly, the locking on the internal cell leads to a remarkable simplification of the hardware setup: the elimination of the saturation spectroscopy setup allows for a reduction of size, complexity and total power consumption by reducing the number of optical, RF and electronic elements.

The second method to frequency lock the laser on the internal cell makes use of the dispersive shape of the light-shift curves as a function of the frequency detuning. The laser frequency that corresponds to a zero crossing for the light-shift curve is again very close to the point of best short-term stability. The algorithm interleaves to the usual POP clock sequence a short Rabi clock sequence (strongly susceptible to light shift) to probe the light-shift and correct the laser frequency detuning accordingly, to minimize it. This latter method has two main advantages: allows to inherently operate the clock at the point where the light-shift is zero (at first order) and allows to retrieve an error signal for the laser frequency lock with a strong signal-to-noise ratio (since the Rabi sequence can be optimized for light-shift detection, without interfering with the main loop). Of course, it has the drawback of interleaving an additional step in the total clock sequence which is seen as dead time for the main clock loop, increasing the Dick effect (in)stability contribution from LO frequency noise.

Before entering into the details of the two methods, we will briefly recall the traditional locking scheme based on the saturation spectroscopy signal from an external reference cell and some details will be given about the laser frequency stability requirements and about the POP clock short-term performances as a function of the laser frequency.

3.2.1 Laser frequency locking onto an external reference cell

The stabilization of the laser is commonly implemented by using an evacuated reference cell. In our case, the cell contains isotopically-enriched ^{87}Rb and is heated to around 30 °C. In Fig. 3.7 the locking scheme is presented. A polarizing beam splitter (PBS) separates the main laser beam into two branches. The main branch is used for the clock operation (pumping and atomic detection). The other branch is used for the stabilization on the external reference. The power ratio between the two branches is selected by means of a half-wavelength plate. On the reference branch, the main beam is again split into three different paths with a parallel plate to perform the saturation spectroscopy [139, 140]. The first and second reflections from the plate constitute two parallel probe beams, while the transmitted light is used as the pump beam. The pump is frequency shifted by 160 MHz with an AOM in double-pass configuration and superimposed to one of the two probe beams almost counter-propagating. The transmission through the cell is detected with a differential photodiode. Since only one of the two probe beams is aligned with the pump, by setting the individual gain of the photodiodes the Doppler profile is canceled and the Doppler-free peaks are better resolved. In order to lock on one of the Doppler-free peaks, the frequency of the pump is modulated by ±14 MHz by acting on the AOM carrier. The error signal is then extracted by demodulating the differential photodiode signal with a digital lock-in amplifier. The correction is

obtained with an analog proportional-integrative controller and performed by acting on the laser current modulation input. The stability of the free-running laser

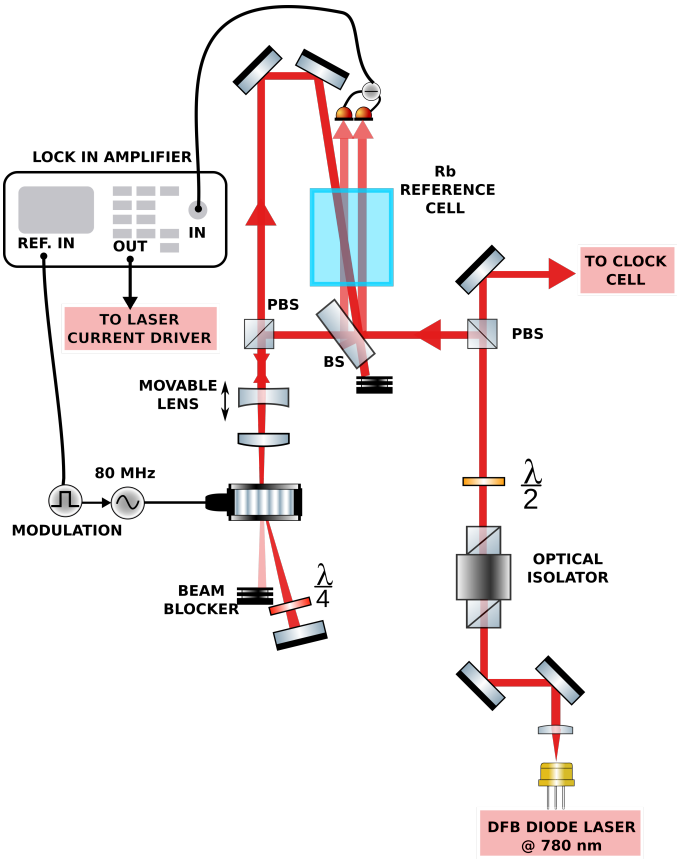

Figure 3.7: Sketch of the experimental setup to implement the frequency lock on the external reference cell.

is reported in Fig. 3.8. It is at the MHz level for averaging times up to 100 s and then increases as random walk. In the same graph, the closed-loop stability of the laser frequency, with the laser locked on the saturation absorption setup, is also shown. The latter measurement is performed by using the clock cell spectroscopy as a reference, thus it might be overestimated. A more rigorous stability measurement is planned by using a stabler reference (i.e. measuring the beatnote with another laser referenced to a frequency comb) or with three-corner-hat technique. Nevertheless, this conservative estimate is well below the requirements (dashed line in the pictures), assuming a clock sensitivity to laser frequency of 2×10^{-14}/MHz.

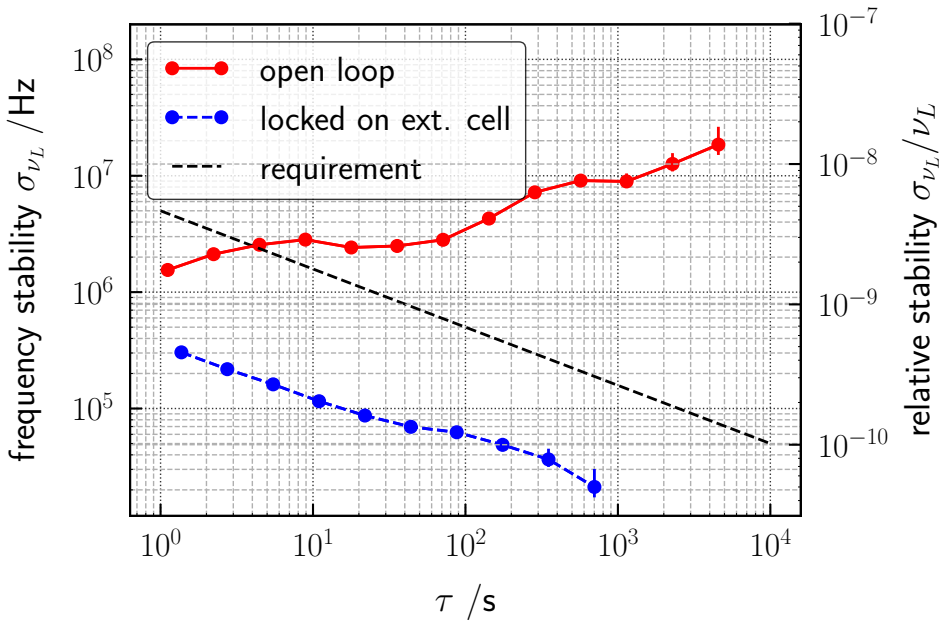

Figure 3.8: Laser frequency stability of our DFB laser free-running and locked on the saturation absorption setup and free-running, compared to the stability requirements for a high-performing POP frequency standard.

3.2.2 Short-term as a function of the laser locking point

The first suggestion towards the use of the clock cell absorption profile as a tool to frequency lock the laser comes from a deeper investigation of the clock short-term stability as a function of the laser frequency. The stability contribution from detection noise can be experimentally estimated as we slowly scan the laser frequency along the absorption profile. The procedure is the following: instead of performing two clock cycles as in usual clock operation, we indefinitely repeat six cycles. The first two cycles acquire the clock signal with the LO frequency set to zero detuning (to remove LO noise contributions). From these signals, the error signal and its Allan deviation (σ_e) are computed. Since the LO contribution is negligible, the variance of the error signal is representative of the detection noise only. Four additional clock cycles with different microwave detuning are performed to evaluate the error signal slope in real time (see Fig. 3.9). The short-term stability is then computed as usual as $\sigma_y = \sigma_e/D_e$ (see section 2.2.1). The result of such investigation are shown in Fig. 3.10 in the case of the D_2 line. In Fig. 3.10 (d) the clock stability retrieved with this method is plotted versus the laser detuning. It is evident how the performances of the clock strongly depend on the locking point for the laser frequency. There is a clear region of minimum stability, and the laser

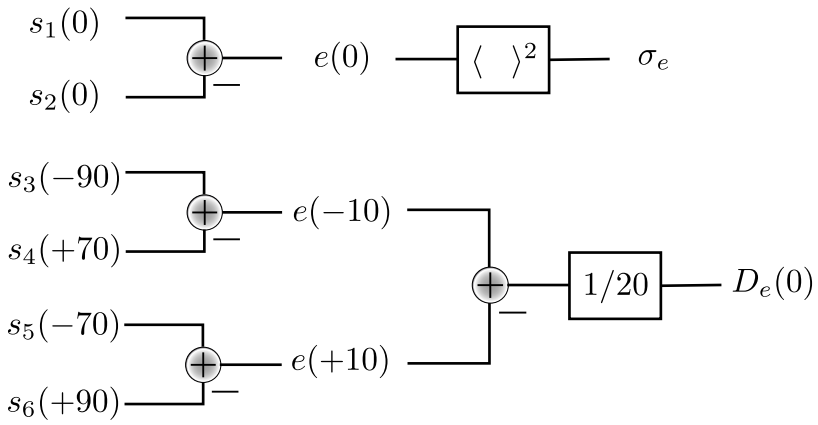

Figure 3.9: Extended clock sequence to evaluate the error signal variance and slope in real time as a physical parameter is scanned.

frequency must lie within few tens of MHz from the optimum not to degrade the stability significantly. For this reason, if using the external reference spectroscopy, not all the Doppler-free peaks are equivalent and even when choosing the peak closest to the optimum, the frequency bridge needs to be finely adjusted. This may lead to work with AOM RF frequency away from the nominal ones, with consequent power inefficiencies. By looking at Fig. 3.10 (a) and (b), we can notice that the point of best stability coincides with the minimum of the absorption profile or, equivalently, to the zero of its first derivative. If we are able to implement a digital lock-in to perform a laser frequency lock on the clock absorption profile, the setpoint is naturally optimal for what concerns the short-term stability. Moreover, locking on the bottom of the clock cell profile, there is no need to have a separate laser branch for the saturation spectroscopy and, consequently, there's no need to bridge the frequency of the laser, as the best stability naturally occurs when the first derivative if the clock cell absorption profile nulls. In the following sections, the algorithm to performs such frequency lock is described, and a preliminary characterization is given.

3.2.3 Laser frequency locking on the clock cell absorption profile: algorithm

The algorithm to perform the laser frequency lock on the clock cell is by all means similar to the one used for the lock of the LO field amplitude (section 3.1). The clock basic cycles are four and a double modulation is performed. The doubling of the traditional clock pattern allows for a symmetrization of the interrogation

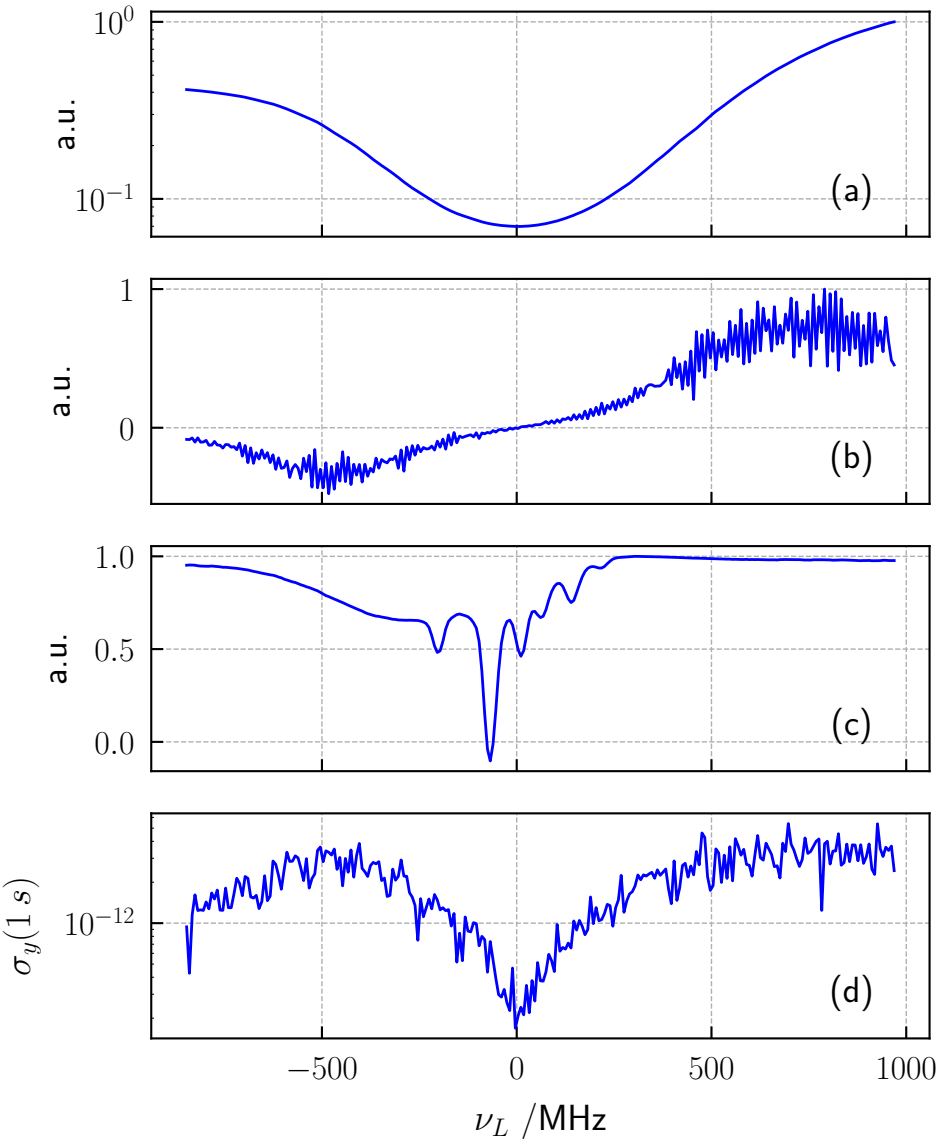

Figure 3.10: a) clock cell absorption profile; b) first derivative of the absorption profile; c) External cell saturation spectroscopy signal (laser frequency shifted by 80 MHz on this branch). d) Experimentally evaluated short tern stability $\sigma_y(1s)$.

sequence. In this way, no net shift occurs on the clock frequency because of the laser frequency modulation. The laser frequency modulation is performed by sending a square wave to the laser current modulation input (thus the laser current is $i_L = i_0 \pm i_m$). The error signals for the LO frequency loop and for the laser frequency loop are the result of a linear combination of the four clock signals (S_i,

with $i = 1,4$). Since all the signals are involved in the clock error signal creation, no additional dead-time is introduced for the main clock loop, and the contribution to the stability from the Dick effect is unchanged. If the correction to the LO is performed at the end of four cycles, then the maximum locking bandwidth is reduced by a factor two. Nevertheless, if needed, the correction can be implemented every two cycles as in usual operation and no average shift would be induced in any case.

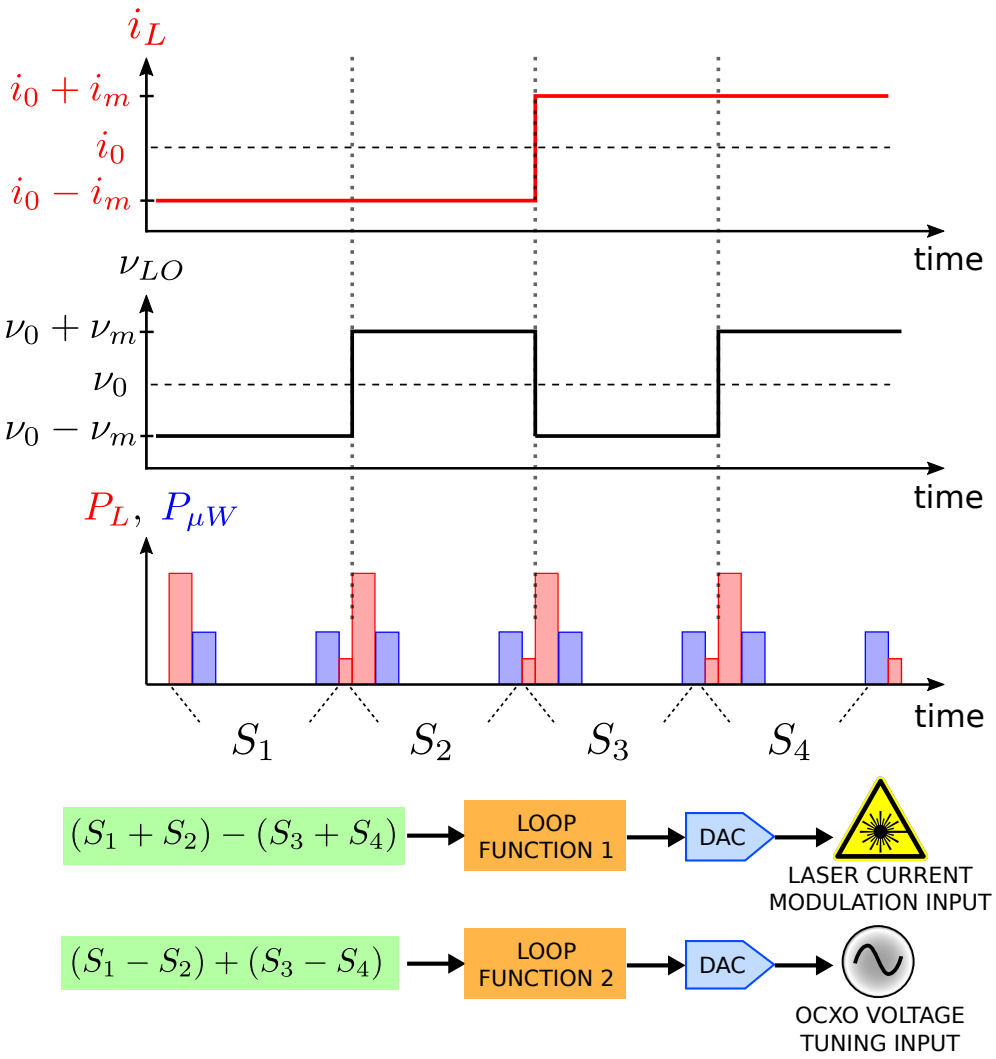

Figure 3.11: Scheme of the algorithm to frequency lock the laser on the clock cell absorption profile.

Detection noise and locking bandwidth

The lock on the clock cell profile has a rather simple implementation (one single extra modulation plus an additional actuator). Nonetheless, care must be taken, as the lower error signal slope, compared to the saturation absorption signal case, poses more stringent requirements on the detection system noise. Indeed, detection noise is translated into frequency noise by the loop itself. The lowest boundary to the achieved stability of the laser frequency is thus set by the detection system. Hopefully, in case of white noise, the contribution will scale as $\tau^{-1/2}$. To characterize the loop we also need to assess the proper locking bandwidth. The latter needs to be set in order to achieve the desired medium-term performances. By looking again at Fig. 3.8, we can see that a loop attack time of 4 s is enough to reach the target stability. Given an extended clock sequence duration T_s of about 17 ms, we should expect no impact on the clock stability by locking the laser frequency with the proposed algorithm. Indeed, the loop will begin to compensate for the laser fluctuations after a few T_s. The achievable bandwidth of the loop is also influenced by the width of the resonance profile, the modulation depth ν_m and the integral/proportional gains of the loop. The optimal modulation bandwidth is chosen with the following criteria: 1) a lower bound is set by the need for sufficient bandwidth and related loop gain to achieve the desired medium-term frequency stability. 2) a higher bound is set by the short-term performance. Indeed increasing the modulation depth too much would interfere with the clock loop, by reintroducing FM-AM conversion. In this section, we will evaluate the noise contribution from the laser itself and from the detection system in the case of our prototype. Moreover, we will characterize the bandwidth of the lock for the privileged modulation depth.

The detection noise of the loop is estimated by locking the laser on the external reference cell and acquiring the error signal e_{ν_L} obtained with the algorithm of section 3.2.3 with no current modulation i_m. In this way, the variance of e_{ν_L} is representative of the detection noise only (assuming that the external lock does not introduce additional noise). As usual, if we divide the variance of the error signal by the laser frequency discriminant $D_{e_L} = \Delta e_{\nu_L}/\Delta\nu_L$, we can obtain an estimate of the laser frequency fluctuation induced by the detection system. Fig. 3.12 shows such estimate in terms of Allan deviation of the laser frequency. The stability contribution coming from the current detection system is more than one order of magnitude lower compared to the requirements (assuming a sensitivity of the clock $(\Delta\nu/\nu_0)/\Delta\nu_L = 2 \times 10^{-14}\,\mathrm{MHz}^{-1}$). In Fig. 3.13 the response of the frequency lock to an induced frequency jump is shown, together with the correction applied to the laser current (upper plot). The bandwidth of the lock was lowered to 16 mHz for illustrative purposes. In normal operation is at least 4 times higher. In the lower plot, the fractional frequency for the same time slot is presented. We can observe how the stability improves as the loop brings back the frequency of the laser to the

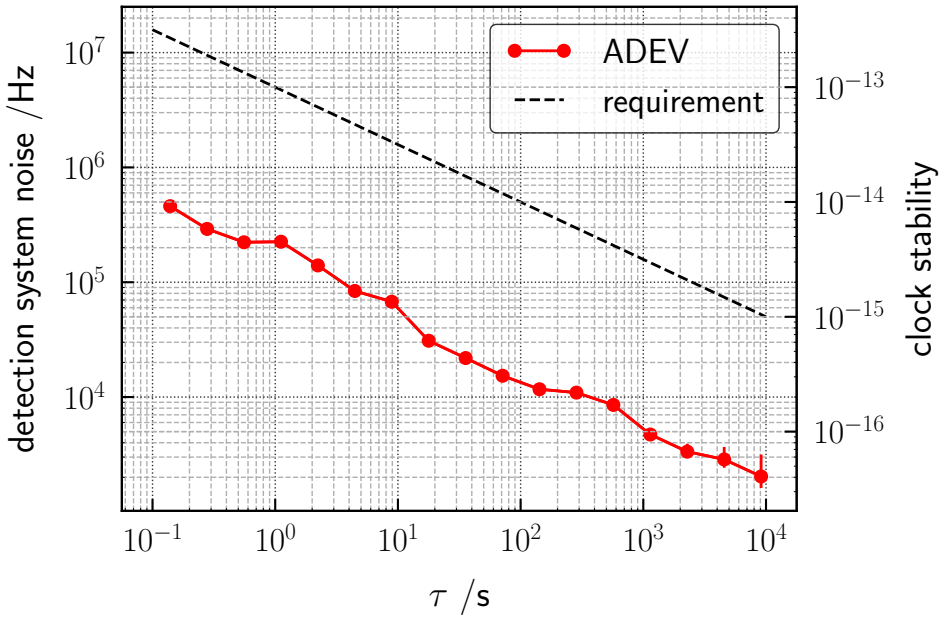

Figure 3.12: Contribution from the detection noise, acquired as explained in the text, converted into laser frequency units by means of the error signal slope D_{e_L}. The dashed lines represents the frequency stability requirements in case of a clock sensitivity $(\Delta\nu/\nu_0)/\Delta\nu_L = 2 \times 10^{-14}\,\mathrm{MHz}^{-1}$.

setpoint.

3.2.4 Laser frequency locking by means of the light-shift curve

In 1975 Arditi and Picqué proposed to exploit the resonant light shift in alkali atoms to frequency stabilize a laser onto a microwave frequency standard. This approach goes somehow in the opposite direction as the recent research field which aims to transfer the nowadays superior phase noise properties of ultrastable lasers into the microwave domain [141, 142]. Nevertheless, we can resume that idea in the case of the POP frequency standard. In this case, indeed we already have a stable microwave oscillator at hand (the clock itself), and the frequency stability requirements for the pumping/detection laser are not so stringent. We can thus think of using the resonant light-shift observed on the clock transition as a tool to stabilize the laser directly on the clock spectroscopy cell. In order to probe the light shift on the microwave transition, we can interleave to the usual POP sequence (which is inherently less sensitive to light-shift) a clock sequence purposely very sensitive to light shift. This can be achieved with a CW interrogation scheme or

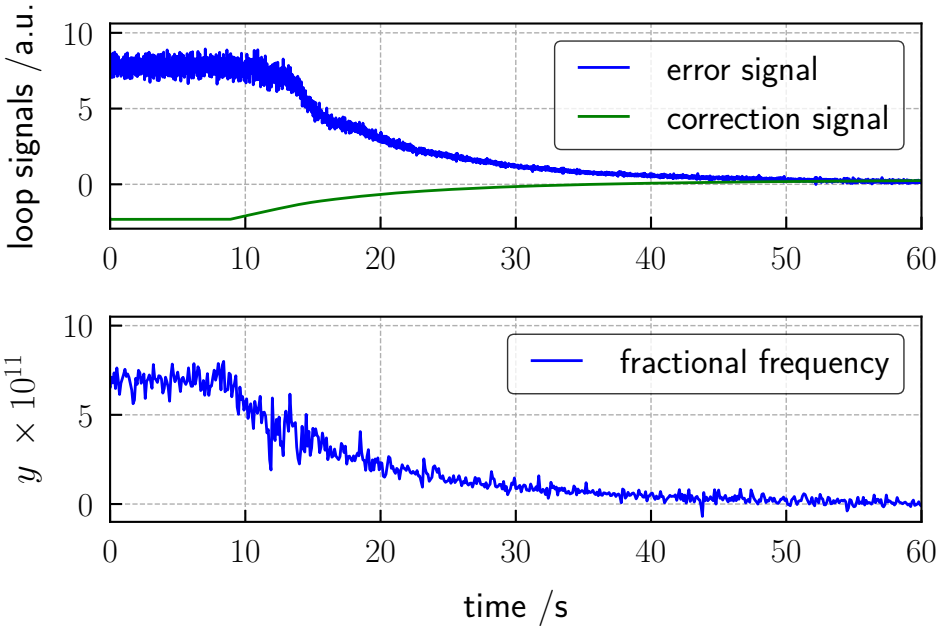

Figure 3.13: a) Transient response of the loop to a frequency jump of the laser. The bandwith of the frequency lock was set to 16 mHz. b) Fractional frequency of the locked LO as measured against a hydrogen maser during the same time period.

with a Rabi interrogation scheme. We prefer the latter since, by introducing an additional pumping phase, we destroy the residual coherence from the previous clock sequence. In this way the two interrogations loops are better decoupled.

The light-shift as a frequency discriminant

The frequency shift induced on the hyperfine microwave transitions by resonant light is a phenomenon often encountered in precision spectroscopy. As observed in [143], the effect of a strong resonant microwave field together with the optical field prevents the use of the standard perturbation theory [144] to describe the effect. In this section, we will not focus on a precise theoretical description of the observed light shift curve, which will be the object of future investigation. We will focus instead on few experimental observations that allow us to insert light-shift into the clock operation as a tool to frequency stabilize the clock laser frequency.

The algorithm to perform the frequency lock by means of the light-shift is depicted in Fig. 3.14. Two different clock schemes are interleaved: the usual Ramsey sequence, each its cycle leading to the signal S_i, and a Rabi sequence giving, as a result, the clock signals $S_{i,R}$. These signals, properly processed, are used as input of two separate digital loops. The Ramsey loop is used to lock the LO frequency, while

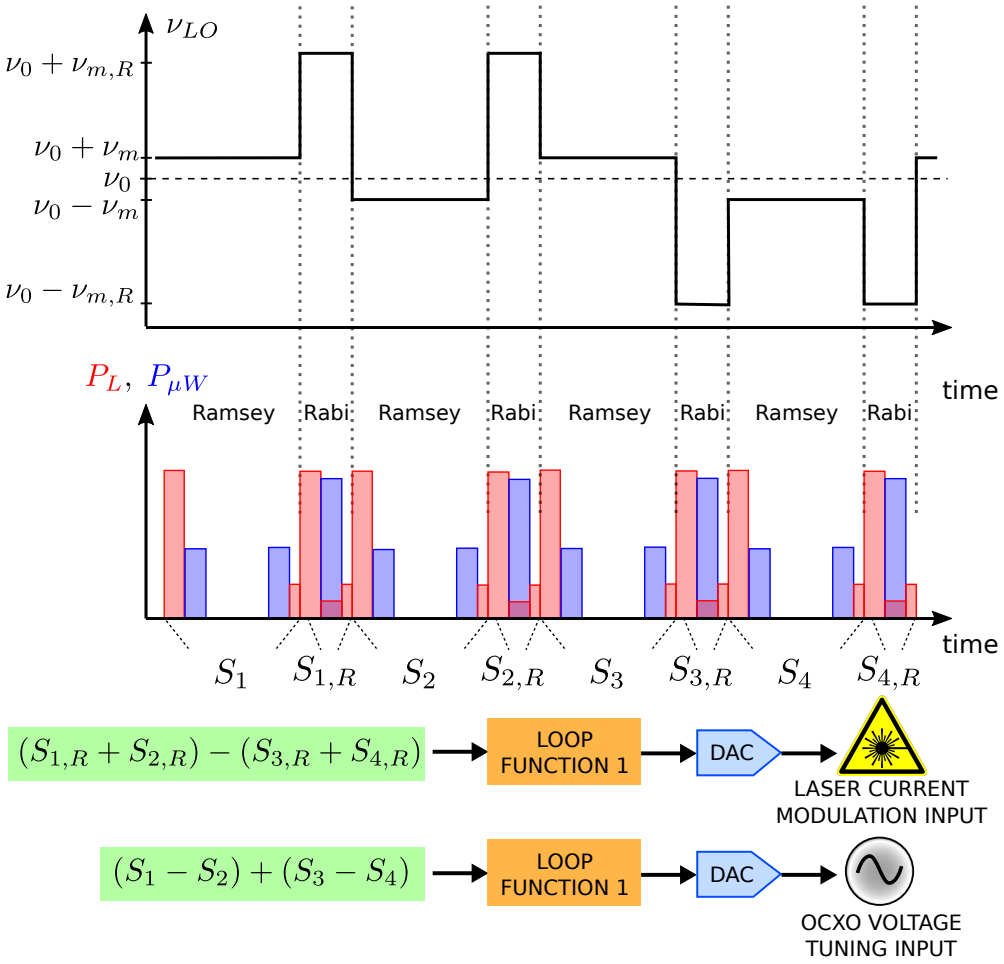

Figure 3.14: Scheme of the algorithm to frequency lock the laser on the clock cell absorption profile.

the Rabi loop acts on the frequency of the laser. The basic Ramsey sequence has the same properties and timings already explained in section 2.1.4. The basic Rabi sequence is composed of a pumping phase (4 ms) in which the atomic coherence is destroyed and the atoms are pumped to the $F_g = 1$ state; after the pumping phase the laser is attenuated to few tens of µW and a microwave π-pulse (8 ms) is applied. Finally, the microwave is switched off and the population of the $F_g = 2$ is probed by a weak laser pulse with absorption spectroscopy (0.1 ms). The low power laser light leaked during the Rabi pulse gives rise to a shift of the microwave clock transition. The magnitude and sign of the shift are dependent on the laser detuning, thus by locking on the zero light-shift detuning, we can perform a frequency stabilization of the laser frequency. In Fig. 3.15 the resonance line probed during the Rabi sequence is plotted as a function of the LO frequency. To highlight the presence

of light-shift, the same curve is acquired with the perturbing laser on and off. In presence of laser light, together with a loss of coherence, we can observe an absolute shift of about 10 Hz. In the clock algorithm, the usual Ramsey sequence, as well as the Rabi sequence, are doubled in order to symmetrize the modulation pattern. Indeed, even if a strong pumping pulse is performed at the beginning of each clock cycle, a small coherence can survive and give rise to a systematic shift. This is also the reason to prefer a Rabi interrogation to a CW clock sequence, even if potentially increasing the dead time. Indeed by performing CW clock spectroscopy interleaved with the Ramsey sequence, we observed survival of the Ramsey pattern superimposed to the CW spectroscopic line. Conversely, we observed no difference in the line of Fig. 3.15a obtained during the interleaved sequence or as a standalone sequence.

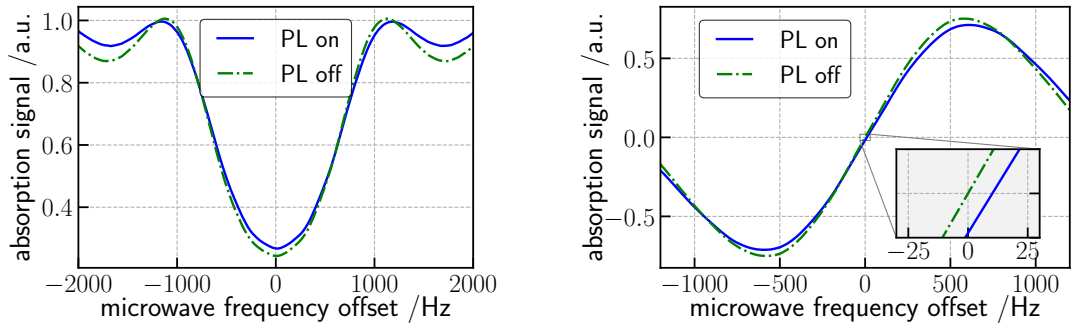

(a) Resonance line obtained with the interleaved Rabi sequence.

(b) Error signal obtained with the interleaved Rabi sequence.

Figure 3.15: Microwave spectroscopy obtained during the interleaved Rabi sequences. The microwave frequency is scanned and the laser frequency is locked on the SAS crossover peak $|F = 2\rangle \rightarrow |F' = 2{,}3\rangle$. The perturbing laser (PL) when present, has a power of 20 µW.

In Fig. 3.16 the light shift observed on the Rabi spectroscopy is plotted as a function of the laser frequency, with the laser tuned on the $F_g = 2$ and $F_g = 1$ line. In both cases a dispersive shape is observed with a zero crossing rather close to the optimum detuning already identified in section 3.2.3. The obtained curve can thus be directly used to frequency lock the laser frequency. As already noted, this locking technique introduced additional dead time to the main clock sequence. Nevertheless for the clock electronics developed in [111] the Dick-effect contribution to the short term stability is 3.5×10^{-14}, thus well below other sources of instability. Conveniently, a dedicated clock sequence for the additional loop allows to freely optimize the physical parameters, independently from the main frequency loop. We point out that in this locking technique, differently from the lock on the absorption profile, the atomic sample which contributes to the lock error signal is just the

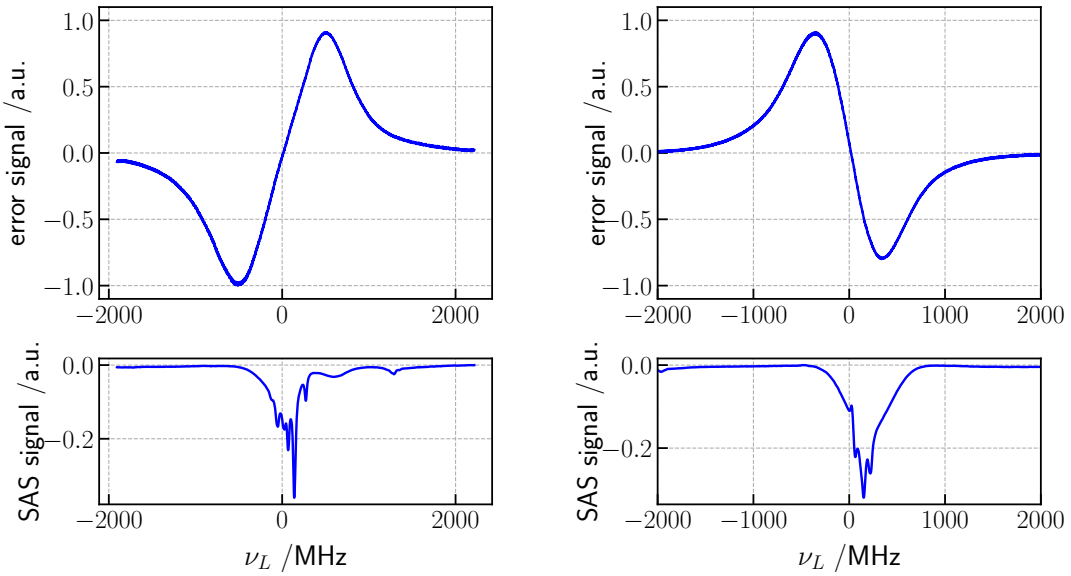

(a) $F_g = 2$ line.

(b) $F_g = 1$ line.

Figure 3.16: Light-shift curve for the Rabi transition which acts as an error signal for the laser stabilization loop (upper plots). The perturbing laser power is 20 µW. Saturation spectroscopy signal, shifted by -80 MHz, is shown as a reference (lower plots).

population of the $m_f = 0$ Zeeman sublevels. This method is thus in principle more immune to effects related to other atoms not contributing to the clock operation. In particular, traces of ^{85}Rb that might modify the total absorption profile, here have no effect on the signal used to frequency lock the laser.

Detection noise and locking bandwidth

To characterize the lock performances, the detection noise must be evaluated. Similarly to the previous case, the error signal for the frequency lock is acquired with the frequency loop open. The perturbing laser is switched off during the Rabi pulse. In such configuration, the error signal does not depend on the laser frequency (has zero average) and its frequency is representative of the detection noise only.

To translate this noise into laser frequency noise units, we divide the variance thus obtained by the laser frequency discriminant $D_{e_L} = \Delta e_{\nu_L}/\Delta\nu_L$, obtained with the perturbed laser on from a laser frequency scan (similarly to Fig. 3.15). The noise contribution coming from the detection system around one order of magnitude below the specification (assuming a clock sensitivity of $2 \times 10^{-14}\,\mathrm{MHz}^{-1}$) and scales as $\tau^{-1/2}$ up to above 1000 s. For longer averaging times some flicker contribution

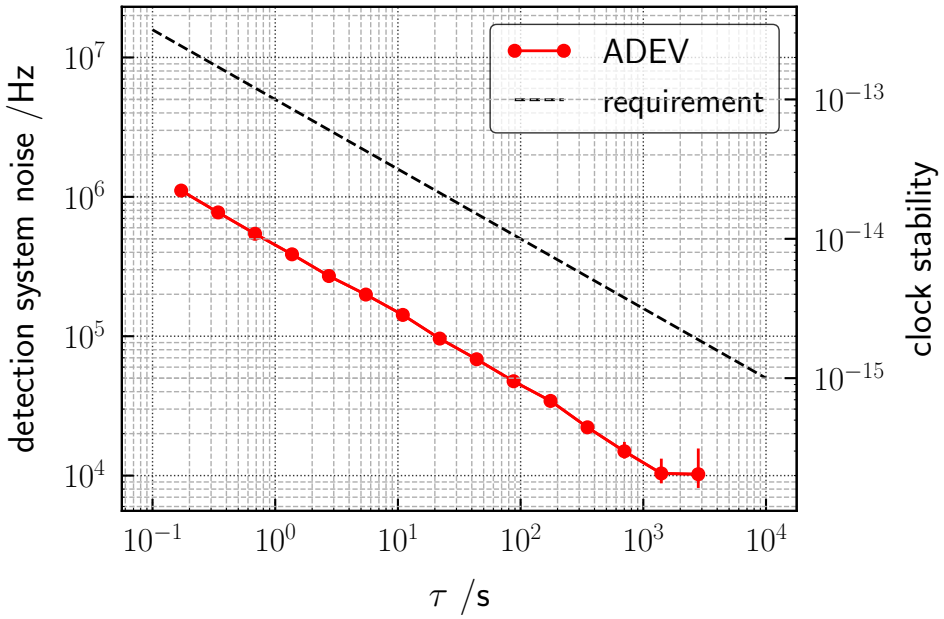

Figure 3.17: Noise contribution from the detection noise, acquired as explained in the text, converted into laser frequency units by means of the error signal slope D_{e_L}. The dashed lines represents the frequency stability requirements in case of a clock sensitivity $(\Delta\nu/\nu_0)/\Delta\nu_L = 2 \times 10^{-14}\,\mathrm{MHz}^{-1}$.

seems to appear. The reproducibility and origin of this noise property is under investigation.

The bandwidth of the lock is chosen with the same criteria already expressed in section 3.2.3. In usual operation, the loop attack time is around 2 s. In this case, the free parameter that can be optimized to tune the locking bandwidth is the perturbing laser power. Since the main loop is unaffected by the Rabi sequence, the latter is a true free parameter and can be adjusted to obtain the desired proportional gain.

Chapter 4

A compact cavity-cell assembly

Suitability for spaceborne applications is one of the main goals of the research on compact vapor-cell clocks. For this reason, we have been pursuing a re-design of the physics package, starting from the cell-cavity assembly [70]. The goal is to reduce the size of the physics package core. This would allow the scaling of all the layers of thermal and magnetic shielding, with a consequent significant reduction of the overall size and weight. Moreover, if the cavity-cell assembly is reduced in size, in principle it is easier to reduce gradients of temperature and magnetic fields that can impact the long-term stability. To our knowledge, two solutions are available to reduce the size of the microwave cavity keeping it resonant with the atomic transition: the use of a slotted-tube cavity ("magnetron-style") or the use of a dielectric-loaded cavity. The first approach has been already implemented for the POP clock in [33], leading to an external volume for the cavity of 44 cm^3 compared to an inner volume for the usual TE_{011} cylindrical cavity of 100 cm^3. The loaded-cavity approach has been already proposed at least on two occasions: for a compact lamp-based Rb clocks [145] and for a compact hydrogen maser [146]. We chose the second approach mainly because of two factors: the easier mechanical design of the structure, with the possibility for the inserted dielectric material to act not only as a filler but also as a spacer, to properly center the cell inside the microwave cavity. Secondly, the potential stronger reduction of size, if the proper dielectric is chosen. From the research point of view and especially for industrial applications, it is also interesting to explore an alternative technique. Having additional design solutions can be of great benefit to the establishment of the POP clock as a mature technology.

4.1 Design of the loaded cavity

The design driver of the cavity-cell assembly is, of course, the electromagnetic uniformity and the quality of the mode. The design phases were structured along

the following workflow to reach the final configuration: the first step is the choice of the materials, based on their mechanical, thermal and electric properties. Subsequently, a Finite Element Methods (FEM) simulation of the cavity eigenmodes is performed. Based on the results of the simulation, a proper geometry for the cavity and cell is fixed. After a suitable geometric configuration for the clock cell is found, the best buffer-gas mixture and pressure is analyzed by considering the hyperfine coherence relaxation terms as well as the temperature coefficients. Finally, all the contributions to the short-term stability are calculated and a stability budget is obtained. The design is validated (or rejected) on the basis of the expected stability. The stability threshold that we considered is below 1×10^{-12}, while the goal is to remain below 5×10^{-13}. The description of the cavity assembly design in the following sections follows these conceptual steps. For clarity's sake, in this thesis, only the final configuration is described, not mentioning all the discarded solutions.

4.1.1 Choice of the materials

The choice of the material for the cavity internal parts must meet two fundamental criteria: being transparent at GHz frequencies (low loss-tangent $\tan\delta$) and having a high loading power (high dielectric constant ϵ). Moreover, a good thermal conductivity is preferred, to allow better thermal uniformity at cell location. Regarding the loading dielectric, high-purity alumina (Al_2O_3) meets all of these criteria, since it can have small losses ($\tan\delta < 10^{-4}$) and an extremely high dielectric constant (close to 10 in the GHz range [147]). Moreover Al_2O_3 has a relatively high thermal conductivity of $30\,\mathrm{W\,m^{-1}\,K^{-1}}$, considering that is a ceramic material. Finally, it is desirable for the loading material to be stable with respect to temperature, namely to have a dielectric constant not rapidly varying with the temperature. This would ensure the microwave cavity mode frequency to be resilient against environmental changes. Again, high-grade alumina meets this requirement, with a relatively low temperature dependence of ϵ on temperature (of the order of 10^{-2} %/K). As reported in [148], doping with TiO_2 leads to reduced temperature dependence, or even to a change of sign of the thermal coefficient. This can be exploited to compensate for the intrinsic thermal expansion coefficient of the metallic cavity, leading to a very thermally stable cavity ensemble. This doping was not investigated here mainly for difficulties in the procurement of the manufactured pieces, but it will definitely be an option for future optimization.

The other choice in play is the cell material. In previous realizations of the POP clock, a quartz cell was used, mainly because the interrogation scheme was based on microwave photons detection [106]. In that case, a very high cavity quality factor was mandatory, and only the low dielectric losses of quartz met the requirement. In the case of the POP with optical detection such a high quality factor is no more needed, and in fact could be even detrimental, as a very selective cavity leads to higher cavity-pulling related instabilities [133, 149]. For these reasons, we

included in the project one batch of cells made of Pyrex, a material that ensures moderate losses and can be more easily shaped from the manufacturer's point of view. For another batch of cells, we used quartz, as it has more predictable and known properties. This batch can be used as a benchmark in case the Pyrex presents some anomalous behavior. The two batches share the same geometry.

Finally, the material of the microwave cavity itself is to be identified. For the first proof of principle realization, we choose aluminum, as it is light, easily manufactured, it has good electrical and thermal conductivity. For thermal uniformity reasons, copper is a superior material, while for the stability of the cavity mode a material with a lower thermal expansion coefficient (like Molybdenum) is preferable. If one of these two aspects will reveal to be critical during the testing phase, a second generation of the prototype will be realized with the optimal material solution.

4.1.2 Mechanical design

The design of the physics package maintains the layered structure typical of vapor-cell clocks, with the clock cell representing the core of the structure. The cell is placed at the center of the loaded microwave cavity and their design is tightly connected. As it will be further explained in the following, the dimension of the cell are chosen following a few criteria: the ratio of microwave cavity and cell dimension should ensure good microwave field uniformity. The uniformity is also determined by the aspect ratio. A good rule of thumb is to maintain the ratio between the diameter and the length of the cavity (and of the cell) close to 1 [70]. Moreover, the cell must be large enough to ensure a large population and good optical access for probing the atomic transition with a high signal-to-noise ratio.

Since we are going to operate with a cylindrical cavity, all the components of the physics package share a cylindrical geometry. The cell has internal length d and diameter $2a$ both equal to 1 cm and a windows thickness of 1 mm. A stem reaches out from the body of the cell and exits the cavity from the bottom. This configuration allows the rubidium reservoir placed in the stem to lie outside the electromagnetic field volume. The end tip of the stem is in thermal contact with the first thermal shield, stabilized at a lower temperature with respect to the cavity. This thermal gradient ensures the excess metallic rubidium to condensate outside the active volume, avoiding metalization of the cell walls, which is detrimental for two reasons: it perturbs the cavity mode and it changes the transmittance of the laser light across the cell.

The cell is supported by the loading material itself, which is a monolithic alumina tube. The purity grade of Al_2O_3 is 95.5 %. The material was sintered, cut to the final shape and finally polished by the manufacturer (Morgan Advanced Ceramics). The loading material is made cylindrical to maintain as much as possible the symmetry of the system. As explained later during the electromagnetic study, the

loading material does not touch the cavity walls. It is thus centered with respect to the cavity walls by means of Teflon supports. It has 12.5 mm internal diameter, 20 mm external diameter and a length of 18 mm. Moreover, the tube presents a rectangular recess to allow the cell stem to pass through. The cavity is designed to

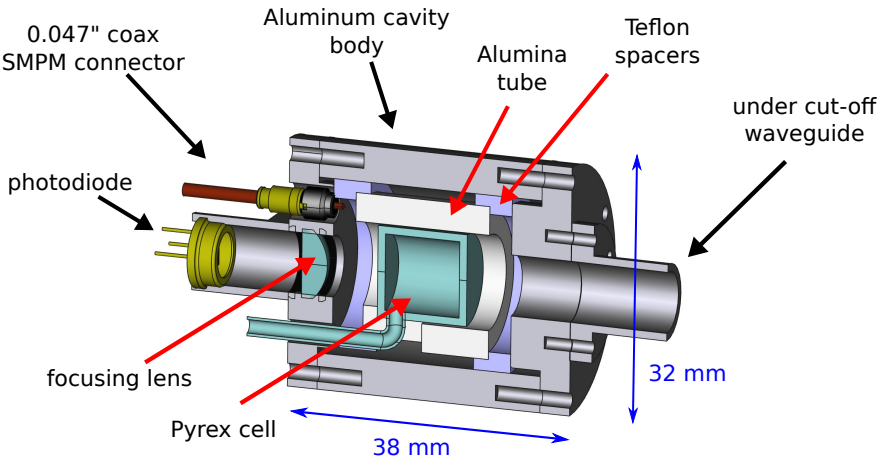

Figure 4.1: CAD rendering of the cavity cell assembly.

resonate in a cylindrical pseudo-TE_{011} mode, thus the mechanical design is rather simple. The cavity is composed of a cylindrical body and two end caps. The internal radius of the cavity is 11.5 mm, while the distance between the two caps, constituting the length of the cavity, is 24 mm. The caps are made with an indented surface entering the cylinder. The radius of the indented part is 0.75 mm smaller than the internal radius of the body. In this way, the internal surfaces (constituting the microwave cavity boundaries) of the cap and body are not continuous and the axial current lines cannot close. This arrangement constitutes a mode-choke for the TM_{111} mode, which is expected to be the closest one to the operational mode. Conversely, the TE_{011} mode, whose current lines are along the tangential direction, is unaffected. The two end caps present a circular hole with 9 mm diameter to allow the passage of the laser beam. To prevent microwave leakage around 6.8 GHz two under-cut-off waveguides are placed in correspondence of the two holes. A waveguide length of 13 mm allows for a field attenuation ($10\log(H/H_0)$) of -22 dB. The caps-waveguide interior is threated, to allow the placement of a focusing plano-convex lens ($f = 20$ mm) and the detection photodiode along the optical axis. Both elements are fixed by retaining rings.

In Fig. 4.1 a CAD rendering of the final design solution is shown and the main components previously described are labeled. The loaded cavity assembly, including the waveguides, has an external volume of only 37 cm^3 and a total mass budget of 0.077 kg.

4.1.3 FEM electromagnetic simulations

The simulations are performed with the Finite Element Method (FEM) software CSTstudio. An eigenfrequency analysis is conducted to identify the resonance modes of the loaded cylindrical cavity. Given the relatively low dielectric losses expected in the system, the spatial configuration of the modes is determined with loss-free materials, and the Q-factor is estimated a-posteriori from dielectric and wall losses. As a first step, the mode of interest (pseudo-TE_{011}) is recognized. Then the parameters of cavity, cell and loading material are optimized to tune the mode frequency to the atomic frequency. Finally, the magnetic field distribution is analyzed and, in particular, the field uniformity along the z-axis is quantified.

Determination of the cavity eigenmodes

The TE_{011} mode is identified by its spatial configuration, with the H field aligned along the z-axis at the center of the cell and the field lines closing in a toroidal configuration. In Fig. 4.2 the $\vec{H}$ field is shown in the (x, z) and in the (y, z) planes. For

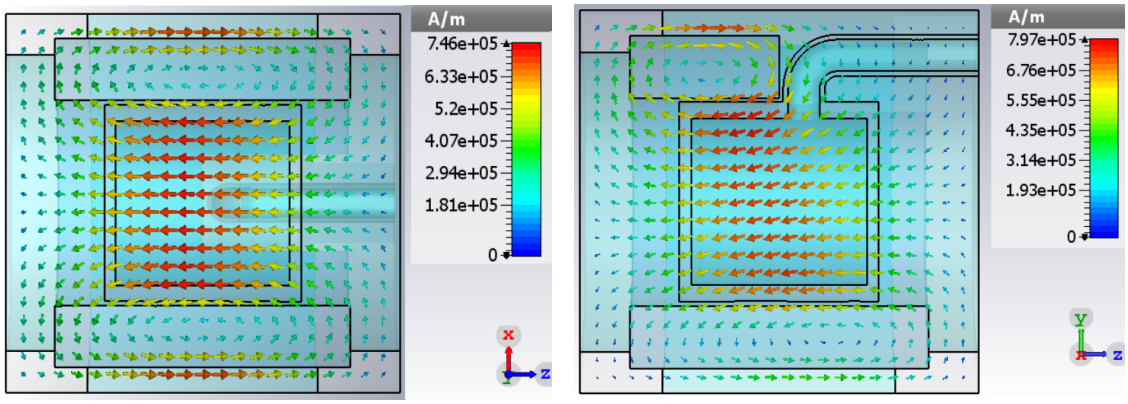

(a) $\vec{H}$ field in the (x, z) plane. (b) $\vec{H}$ field in the (y, z) plane.

Figure 4.2: $\vec{H}$ field distribution for the TE_{011} mode.

the geometrical configuration of section 4.1.2 the TE_{011} resonates at 6.94 GHz. The strong dielectric loading favorably lift the degeneracy with the TM_{111} mode, which is found at 7.38 GHz. The nearest lower-frequency mode is instead at 5.98 GHz and is recognized as the TM_{011}. $\vec{H}$ field distribution for these two modes is shown in Fig. 4.3. Focusing on the TE_{011} mode, the first thing that emerges is that the stem introduces some degree of mode distortion, especially in the (y, z) plane. But as we will see in the next section, the overall degree of uniformity is rather good. This is because the electric field is attracted in the zone of maximum dielectric permittivity (the alumina tube), and the area where the H_z field nulls is pulled farther from the active area. This behavior is expected from perturbation theory,

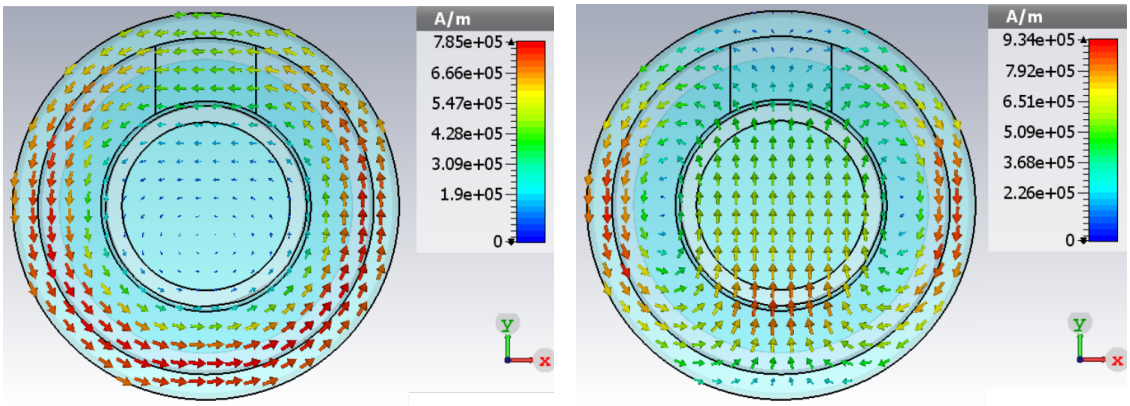

(a) TM_{011}, $\nu = 5.98\,\text{GHz}$. (b) TM_{111}, $\nu = 7.38\,\text{GHz}$.

Figure 4.3: $\vec{H}$ field distribution for the nearest cavity modes.

which demonstrates that the state of minimum energy (the eigenstate) is the one that maximizes the $\vec{E}$ field in the region of higher dielectric constant ϵ [150]. The effect is evident if we look at the distribution of the component E_x of the electric field (Fig. 4.4). Another remarkable finding from the simulation is the need for a small gap between the walls of the cavity and the alumina tube. When no gap is provided, the TE_{011} is not excited or heavily distorted. The physical reason is probably that the electric field is pulled very close to the walls. Consequently, the magnetic field lines have no room to concatenate the electric field and close the loop.

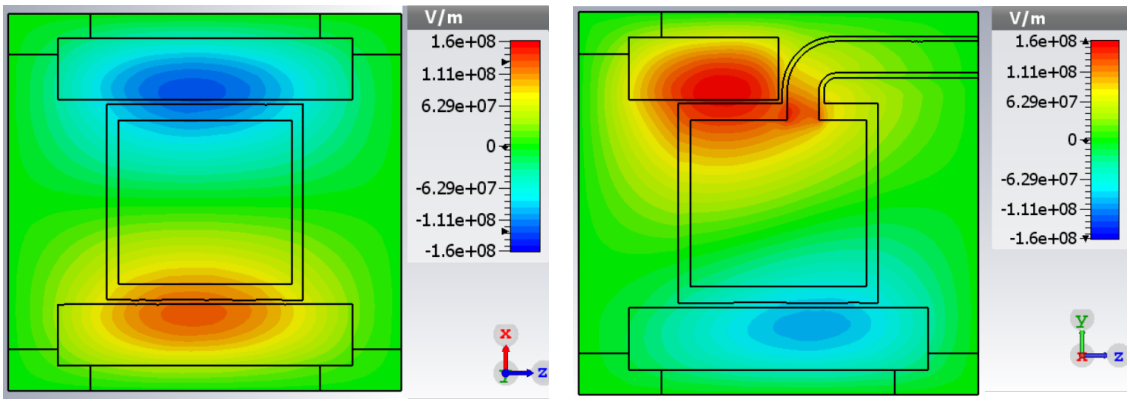

(a) E_x component in the (x, z) plane. (b) E_x component in the (y, z) plane.

Figure 4.4: E_x distribution for the TE_{011} mode.

Quality factor

The quality factor of an electromagnetic mode (at angular frequency ω_0) is defined as the ratio between the stored electromagnetic energy and the power lost in the conducting walls and lossy dielectric [151]:

$$Q = \omega_0 \frac{\text{average energy stored}}{\text{power loss}} = \omega_0 \frac{W_m + W_e}{P_l} \tag{4.1}$$

At resonance, we can also use the fact that the electric and magnetic energy are equal ($W_e = W_m$), so we can write:

$$Q = \omega_0 \frac{2W_m}{P_l} = \omega_0 \frac{2W_e}{P_l} \tag{4.2}$$

Thus it is sufficient to calculate only the time-averaged stored electric energy in the cavity volume V:

$$W_e = \frac{1}{4} \Re \int_V \vec{E} \cdot \vec{D^*}\, dV = \frac{\epsilon}{4} \int_V \vec{E} \cdot \vec{E^*} \tag{4.3}$$

where the second equality holds for a lossless isotropic media (ϵ constant and real, thus $\vec{D} = \epsilon \vec{E}$). Reintroducing small power losses, with the perturbation method approach, we can calculate two main contributions: the loss due to the cavity walls and the dielectric losses. The first contribution is found with the following expression:

$$P_c = \frac{R_s}{2} \int_S |\vec{H} \times \vec{n}|^2 dS \tag{4.4}$$

where $\vec{n}$ is the normal to the cavity inner surface S. R_s is the surface resistivity of the conductor, which is linked to the material electric conductivity σ by the relation $R_s = \sqrt{\frac{\omega_0 \mu}{2\sigma}}$. The losses due to the dielectric inside the cavity volume, on the other hand, are given by:

$$P_d = \frac{1}{2} \int_V \vec{J} \cdot \vec{E^*}\, dV = \frac{\omega_0 \epsilon''}{2} \int_V |\vec{E}|^2\, dV \tag{4.5}$$

Here ϵ'' is the (small) imaginary part of the dielectric constant ($\epsilon = \epsilon' + j\epsilon''$) which in turn is related to the more commonly encountered loss-tangent as $\tan\delta = \epsilon''/\epsilon'$. Equations (4.4) and (4.5) can be used together with (4.2) and (4.3) to obtain the individual quality factors Q_c and Q_d. If the two terms have similar magnitude, they must be added together in the following way to obtain the global quality factor:

$$Q = \left(\frac{1}{Q_c} + \frac{1}{Q_d} \right)^{-1} \tag{4.6}$$

The quality factor is calculated for the results of the simulation by interpolating the electric field $\vec{E}$ and magnetic field $\vec{H}$ as derived from the FEM calculation and

performing a numerical integral over the surface (in the case of the walls losses) or over the inner volume (in the case of the dielectric losses). For the case of the geometry described in section 4.1.2 with the quartz cell, we get a total Q factor of 4500. For the case of the Pyrex cell, from the simulations (assuming $\tan\delta = 0.005$ for Pyrex) we predicted a Q value of 1800. This value must be taken with care, as the concentration of impurities determining the total losses is not usually found in the material datasheet nor easily predictable.

Field uniformity and filling factor

As previously mentioned, the field uniformity inside the active volume is one of the main goals of the design process. To quantify the alignment of the $\vec{H}$ field along the quantization axis (z), we need to define a suitable parameter. This can be the uniformity factor, already introduced in [70]. Here we define it in a slightly different way, to account for the fact that for asymmetry reason the maximum of the field can be away from the center of the cavity:

$$u = \frac{\int_{V_a} H_z(x,y,z)^2 \, dV}{V_a \max\limits_{(x,y,z)\in V_a} |H_z(x,y,z)|^2} \tag{4.7}$$

where V_a is the active volume. The active volume is the portion of the cell that intersects the laser beam. Since often the dimension of the beam coincides with the dimensions of the cell and to avoid ambiguity, we consider the active volume as the whole cell volume. Obviously, the parameter u defined in this manner is always smaller than unity and equal to 1 for a perfectly uniform field.

Another meaningful parameter is the filling factor η', which quantifies the coupling of the $\vec{H}$ field excited by the cavity to the atomic sample. It is defined as:

$$\eta' = \frac{\left(\int_{V_a} \vec{H}\cdot\vec{z}\, dV\right)^2}{V_a \int_{V_c} |\vec{H}|^2 \, dV} \tag{4.8}$$

The filling factor is an important design parameter in the case of maser systems or in POP schemes where the detection is performed via the free-induction decay [106]. In the POP scheme with optical detection η' plays a minor role, determining the strength of the cavity-pulling effect, thus it will be reported here for completeness.

From the values of magnetic field computed in section 4.1.3, we obtain a uniformity coefficient of 0.78, which is better than the value computed for the case of the traditional cylindrical cavity used in [32] (in that case we get $u = 0.58$ with a quartz cell 20 mm × 20 mm and cavity dimensions $2a = 52$ mm, $d = 49$ mm). Regarding the filling factor, for the alumina-loaded cavity, we obtain $\eta' = 0.2$.

Tuning and thermal sensitivity of the cavity resonance frequency

In this section, we report some of the parameters sweeps that where performed during the FEM analysis. By varying some of the parameters of the simulations we gain some insight on the proper way to tune the cavity mode to be resonant with the atomic transition. Moreover, we can calculate a priori some of the ex-

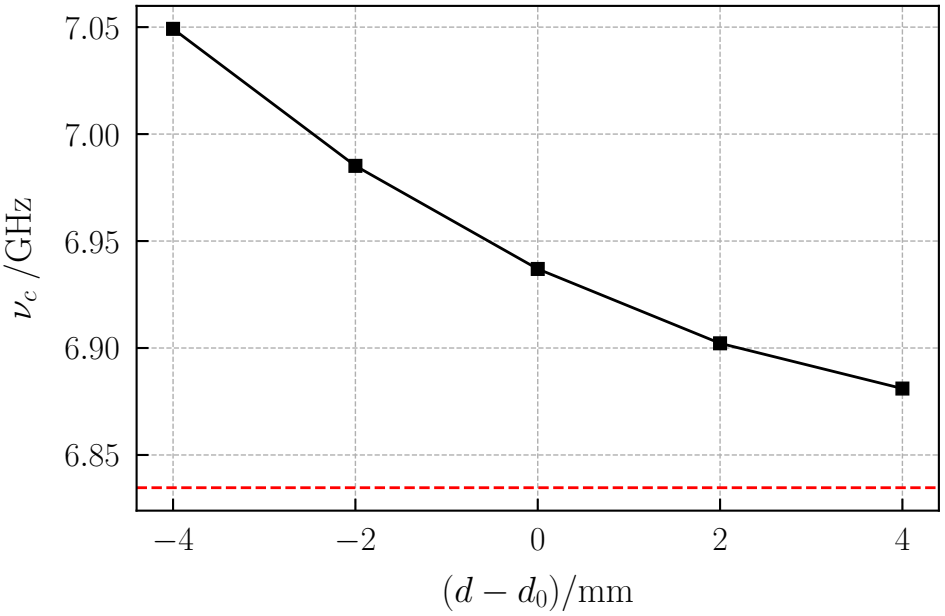

Figure 4.5: Simulated frequency of TE_{011} mode as a function of the cavity length d ($d_0 = 24\,\text{mm}$, $a_0 = 11.5\,\text{mm}$, $\epsilon = 9.4$).

pected sensitivities to environmental perturbations. In particular the sensitivity of the TE_{011} mode to temperature variation can be inferred (knowing the thermal expansion coefficients and dielectric properties of the materials employed).

The first obvious choices of parameters are the cavity length d and the cavity radius a. We separately varied these two quantities, by letting all the other parameters fixed (apart from the Teflon supports dimensions that were varied accordingly to the cavity internal dimensions). The results are shown in, Figs. 4.5 and 4.6. As expected, the frequency of the TE_{011} mode is more dependent on the radius. We can exploit this sensitivity if the cavity needs to be tuned by several hundreds of MHz, whereas a finer tuning is obtained by modifying the cavity length. From the result of the simulation we can extract a total sensitivity coefficient of the loaded cavity to a volume variation, by linearizing the curves of Figs. 4.5 and 4.6 around

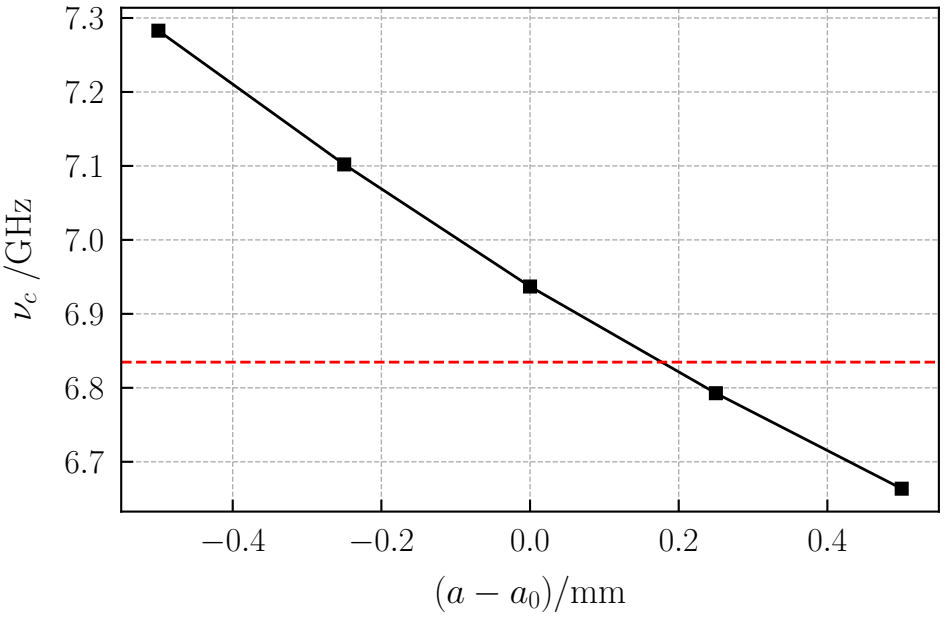

Figure 4.6: Simulated frequency of TE_{011} mode as a function of the cavity radius a ($a_0 = 11.5\,\text{mm}$, $d_0 = 24\,\text{mm}$, $\epsilon = 9.4$).

the expected length values:

$$\frac{\Delta\nu_c}{\Delta T} = \left.\frac{\Delta\nu_c}{\Delta a}\right|_{d_0,a_0} + \left.\frac{\Delta\nu_c}{\Delta d}\right|_{a_0,d_0} \tag{4.9}$$

In this manner the total sensitivity of the cavity resonance due to the thermal expansion is $-180\,\text{kHz/K}$. It can be interesting to compare this value to the case of an empty cavity. For the empty cylindrical cavity the thermal expansion sensitivity has the quite simple expression $\frac{\Delta\nu_c}{\Delta T} = -\alpha_L\nu_C$, where α_L is the linear thermal expansion coefficient of the cavity walls material. In our case, for Aluminum $\alpha_L = 2.3 \times 10^{-5}\,\text{K}^{-1}$, thus leading a sensitivity of $-160\,\text{kHz/K}$. Interestingly, the response of the loaded cavity to a geometric variation is thus quite similar to that of the empty cavity, even with a strong perturbation induced by the alumina.

Finally, we also consider the case of a change in the dielectric properties of the loading material, namely of the alumina tube which has the strongest effect on the resonance frequency. The dielectric constant can change due to temperature, leading to an additional source of environmental sensitivity of the cavity resonance. From the simulation standpoint, we can sweep ϵ to obtain the sensitivity of the resonance frequency to a change of the alumina dielectric constant $\Delta\nu_c/(\Delta\epsilon/\epsilon_0)$. From Fig. 4.7 we get the a value of $-34\,\text{MHz}/\%$. To compute the resonance frequency sensitivity to temperature, we also need the alumina thermal

coefficient $(\Delta\epsilon/\epsilon)/\Delta T$. From the vendor's datasheet, we can extract the ϵ value in the GHz range at three different temperatures (25 °C, 300 °C, 500 °C). Assuming a linear interpolation between the values, we derive a thermal coefficient equal to 9×10^{-5} %/K, and an expected value $\epsilon = 9.4$ at the operational temperature of 65 °C. Combining the sensitivity of ϵ to temperature variation with the cavity resonance sensitivity taken from Fig. 4.7 we obtain an expected sensitivity of the resonance frequency to temperature, due to the loading only, of −280 kHz/K.

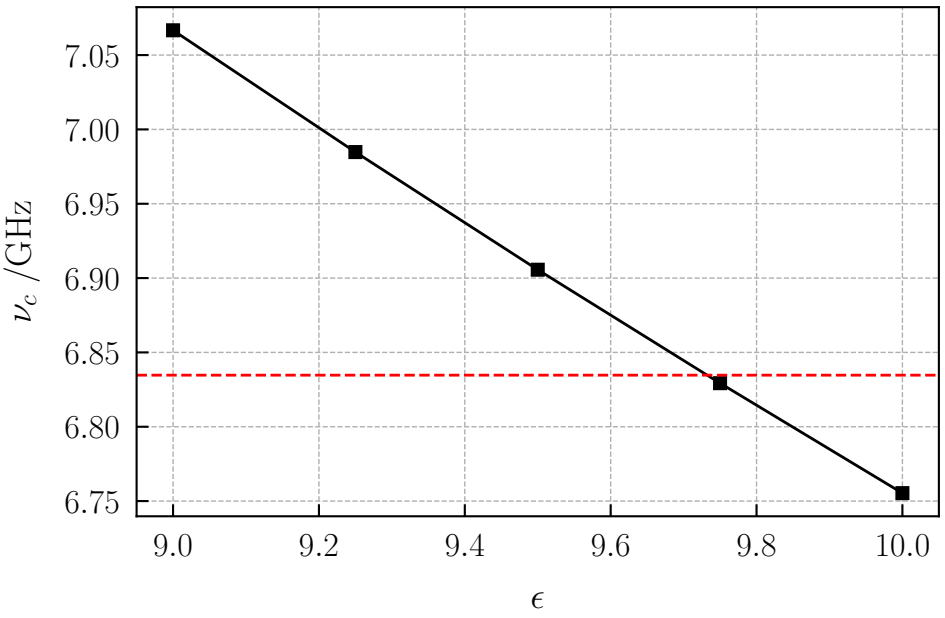

Figure 4.7: Simulated frequency of TE_{011} mode as a function of the alumina dielectric constant ϵ ($a_0 = 11.5$ mm, $d_0 = 24$ mm).

4.1.4 Choice of the buffer-gas

As we have fixed the cavity geometry, and in particular the cell size, we can determine what is the optimal buffer gas mixture total pressure. Two factors need to be considered: the relaxation rate caused by the collisions and the temperature sensitivity of the clock frequency, that is related to the temperature dependence of the buffer gas shift. In the following we will briefly recap these two aspects and later focus on two possible mixture choices that can be used for 1 cm^3 cell.

Relaxation rate terms

In this section, the main contributions to the relaxation of the atomic population inversion and of the atomic coherence, defined with the relaxation rates γ_1 and γ_2 respectively, are briefly resumed.

The first contribution comes from the collision with the cell walls. For a cylindrical geometry, considering only the first diffusive mode, it can be expressed as:

$$\gamma_{1,w} = \gamma_{2,w} = \left[\left(\frac{x_{01}}{R}\right)^2 + \left(\frac{\pi}{L}\right)^2\right] D_0 \frac{P}{P_0} \tag{4.10}$$

where x_{01} is the first zero of the Bessel function $J_0(x)$, R and L the inner radius and length of the cylindrical cell, D_0 the diffusion constant of Rb atoms in the buffer gas at standard pressure P_0 ($P_0 = 1$ atm) and P the total pressure of the buffer gas. This contribution is mainly dependent on the geometry of the cell.

The second contribution to the relaxation rates is due to the collisions with the buffer gas atoms (or molecules). It is thus proportional to the buffer gas cross-section (σ_1 and σ_2), to the total buffer gas density and to the mean velocity of Rb atoms relative to the buffer gas $\overline{v}_r$. Even though this is essentially a density shift, it is generally expressed in terms of buffer gas pressure (assuming a fixed cell volume) with the use of the Loschmidt number L_0:

$$\gamma_{1,bg} = L_0 \overline{v}_r \sigma_1 \frac{P}{P_0} \tag{4.11}$$

$$\gamma_{2,bg} = L_0 \overline{v}_r \sigma_2 \frac{P}{P_0} \tag{4.12}$$

Expression section 4.1.4 is also implicitly dependent on the temperature via the relative velocity $\overline{v}_r$.

The last major contribution comes from the spin-exchange collisions between the alkali atoms:

$$\gamma_{1,se} = n \overline{v}_{Rb} \sigma_{se}. \tag{4.13}$$

Here $\overline{v}_{Rb}$ is the mean relative velocity of Rb atoms and σ_{se} the spin-exchange collision cross-section. In this case, there is a simple theoretical equation connecting γ_1 and γ_2 [131]:

$$\gamma_{2,se} = \gamma_{1,se} \frac{6I+1}{8I+4} \tag{4.14}$$

Temperature sensitivity

The buffer gas introduces an additional source of temperature sensitivity for the clock frequency. The temperature-dependent shift induced by the buffer gas

on the hyperfine frequency can be well approximated by a second-order polynomial expansion [50]:

$$\nu(T) \simeq \nu_0 + P_s \left[\beta + \delta(T - T_0) + \gamma(T - T_0)^2\right] \tag{4.15}$$

where ν_0 is the unperturbed frequency, T_0 is an arbitrary reference temperature and P_s is the sealing buffer gas pressure. The temperature coefficients of various buffer gases have been reported in the literature for ^{87}Rb (see [50]). In table 4.1 we

Table 4.1: Buffer gas coefficients for Ar, N_2, Kr and Ne for the 0-0 hyperfine transition of ^{87}Rb. The reported coefficients are the average of the values available from [53, 130, 152–155]. The uncertainty is set as the scatter between the published values. In the case of the γ coefficient only one value is reported in [130] and no uncertainty is provided.

	Ar	**N_2**	**Kr**	**Ne**
β /(Hz/torr)	-62(7)	550(10)	-610(10)	380(30)
δ /(Hz/torr/K)	-0.34(4)	0.54(2)	-0.63(2)	0.19(8)
γ /(Hz/torr/K^2)	-0.00035	-0.0015	–	–

report them for commonly encountered gas species. If we chose two buffer gases with opposite sign of the coefficient δ, a 2-species mixture can be arranged to suppress the linear term. Thus, only the quadratic term survives and the temperature sensitivity of the clock frequency due to the buffer gas induced shift can be lowered by almost two orders of magnitude. For a mixture of two buffer gases (4.15) can be applied to each gas and the effect of the two components can be added linearly. Thus, we get the expression:

$$\nu(T) = \nu_0 + P_s \left[\beta' + \delta'(T - T_0) + \gamma'(T - T_0)^2\right] \tag{4.16}$$

where now P_s is the sum of the partial pressures ($P_s = P_1 + P_2$). On the other hand, the new coefficient are calculated as:

$$\beta' = \frac{\beta_1 + r\beta_2}{1 + r} \tag{4.17}$$

$$\delta' = \frac{\delta_1 + r\delta_2}{1 + r} \tag{4.18}$$

$$\gamma' = \frac{\gamma_1 + r\gamma_2}{1 + r} \tag{4.19}$$

and $r = P_2/P_1$ is the ratio of the partial pressures. The coefficient β' is responsible for an absolute shift of the clock pressure which can be of several kHz for typical buffer gas pressures. For this reason, together with the low reproducibility of the cell-filling process, vapor-cell clocks are not usable as primary standards. Moreover, the β' coefficient is directly multiplied by the buffer gas pressure. The buffer-gas pressure P_s in the cell volume can be affected by environmental factors, mainly by two mechanisms: a temperature gradient between the cell and the filling stem leads to a migration of the buffer gas between the cell and the stem volume, effectively changing the pressure at cell location. This translates into an augmented sensitivity to temperature [107]. On the other hand, a deformation of the cell walls due to ambient pressure variation can also change the internal pressure of the sealed cell. The latter is usually called "barometric effect" [109, 110, 156]. Both contributions can lead to visible effects, in case of not optimal mechanical design (such as large-volume stem and thin cell walls respectively).

Shift and broadening of the optical D lines

When choosing the buffer gas mixture also the effect of the collision upon the optical (D_1 or D_2) line must be considered. If the frequency lock is performed onto an external reference cell, which does not contain buffer gas, we need to consider the frequency shift induced on the clock cell, which must be bridged by means of acousto-optic modulators or other frequency modulators. As noted in chapter 4, if we consider to lock the laser on the clock cell, also the broadening of the optical line can be an issue, since a broader profile sets more stringent requirements on the detection noise.

In table 4.2 the coefficients for some common buffer gas are reported as taken from [157]. In the following, we will use these data to calculate the expected shift and broadening of the D_2 line (used for pumping and probing of the clock states) for the buffer gas mixtures of interest.

4.1.5 Comparison of two mixtures: argon-nitrogen and krypton-nitrogen

A widely used mixture in vapor-cell clocks is Ar:N_2 [130], due to the relatively low collisional cross-section of the two species and because of the fluorescence-quenching properties of nitrogen [158], a desirable property that reduces radiation trapping with consequent enhanced pumping efficiency when dealing with a thick vapor [144, 159].

We also consider Kr:N_2 mixture because, in this case, not only the δ coefficients are opposite in sign, but also the β coefficients are. Moreover, both coefficients have roughly the same absolute value. Thus a mixture close to 1:1 ratio can lead to a cancellation of the linear temperature dependence together with a small total

Table 4.2: Buffer gas D2-line shift (Δ_{bg}) and broadening (Γ_{bg}) coefficients for ^{87}Rb as taken from [157].

	Δ_{bg} /(MHz/Torr)	Γ_{bg} /(MHz/torr)
He	+0.37(6)	20.0(1)
Ne	-2.44(2)	9.5(1)
Ar	-5.76(4)	17.7(2)
Kr	-5.5(2)	17.2(4)
N_2	-5.8(1)	18.3(4)

pressure shift. With a simple 2-species mixture the temperature sensitivity would be improved and the barometric and stem effect strongly reduced at the same time. The major drawback of using krypton is the higher relaxation rate due to the formation of van der Waals molecules [160]. However, γ_2 values for Kr are not well known in the literature in the pressure range usually employed in vapor-cell clocks, thus we have performed experiments to properly evaluate them.

In the following, we will analyze the two mixtures in terms of temperature sensitivity, collision-induced relaxation and pressure sensitivity.

Argon-nitrogen mixture

The δ coefficient for Ar and N_2 are taken from the literature as $-0.34\,\mathrm{Hz/(K\,torr)}$ and $0.54\,\mathrm{Hz/(K\,torr)}$ respectively. As shown in table 4.3 a pressure ratio of 1.6:1 is used to compensate the linear term. We proceed to investigate the optimal total pressure for such a mixture, in the case of a $1\,\mathrm{cm}^3$ cell, by considering the contributions to the clock state relaxation highlighted in section 4.1.4. In Fig. 4.8 the two pressure-dependent terms are shown as a function of the total buffer gas pressure for a 1.6:1 ratio mixture of Ar and N_2. The values of σ_1 and σ_2 are taken as an average of the values available in the literature [50, 161–165]. In the total relaxation rate the spin-exchange contribution is also included, for a Rb density $n = 3.6\times10^{-11}/\mathrm{cm}^3$ and a value of σ_{se} equal to $1.6\times10^{-14}\,\mathrm{cm}^2$ [131, 166]. From the graph, we can conclude that increasing the buffer gas pressure is helpful to mitigate the effect of walls collisions up to few tens of torr, then the Rb-gas collisional term starts to be predominant and there is no more gain in increasing the pressure. Moreover, higher buffer-gas pressure increases the absolute frequency shift on the

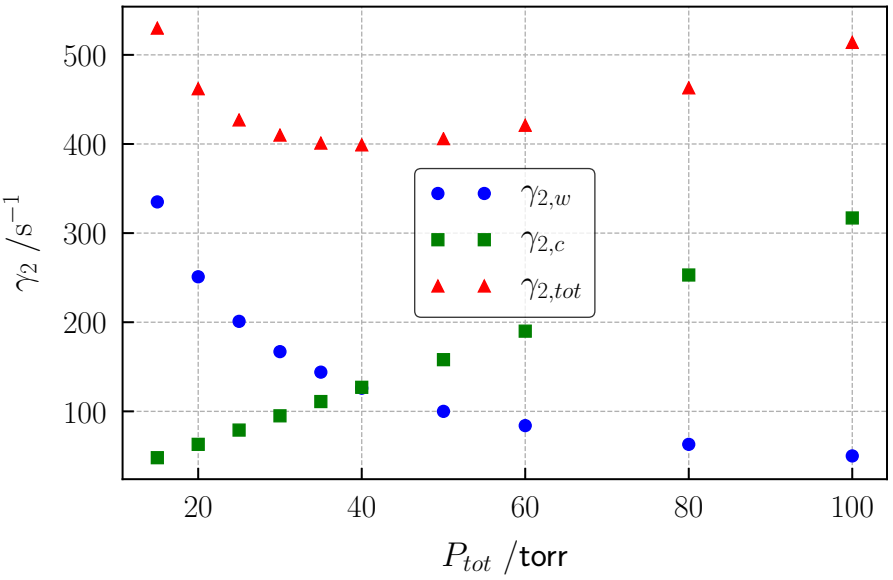

Figure 4.8: Contribution to the relaxation rate due to walls collisions $\gamma_{2,w}$ ($R = 5\,\text{mm}$, $L = 10\,\text{mm}$), Rb-buffer gas collisions $\gamma_{2,bg}$ and total relaxation rate $\gamma_{2,tot}$ (including the spin-exchange term) in the case of Ar-N_2 mixture.

clock transition. In this way, the environmental sensitivities are also increased proportionally to the β' coefficient. An optimal pressure can be around 40 torr, not dramatically higher than the previous POP clock realization with bigger cell size, and where a local minimum for the total γ_2 relaxation rate is expected.

Table 4.3: Buffer gas coefficients for Ar:N_2 and Kr:N_2 mixtures for the 0-0 hyperfine transition of ^{87}Rb. The values are calculated starting from the coefficients for the pure species of table 4.1.

	Ar:N_2 (1.6 : 1)	**Kr:N_2 (0.9 : 1)**
$\boldsymbol{\beta'}$ **/(Hz/torr)**	175(6)	3(8)
$\boldsymbol{\delta'}$ **/(Hz/torr/K)**	-0.00(2)	-0.01(1)
$\boldsymbol{\gamma'}$ **/(Hz/torr/K^2)**	-0.0008	–

Krypton-nitrogen mixture

As already noted, by looking at table 4.3, a proper ratio between the partial pressures of Kr and N_2 that simultaneously cancel the δ' coefficient and the β' coefficient can be found. In particular, a pressure ratio between krypton and nitrogen of 0.9:1 satisfies this condition.

Once we have determined the gas composition, the proper total pressure is to be found. In the case of Kr, the relaxation rate of the coherence shows a non-linear behavior with respect to pressure due to van der Waals molecules formation, thus we cannot easily calculate a priori γ_2 as in the previous case. We can instead plot γ_1, to have an idea about the expected timescales of the relaxation rates for the ground states population. In Fig. 4.9 the main relaxation terms are put together. Here too, a pressure around 30-40 torr is a reasonable compromise between buffer-gas and wall induced relaxation for a $1\,\mathrm{cm}^3$ cell.

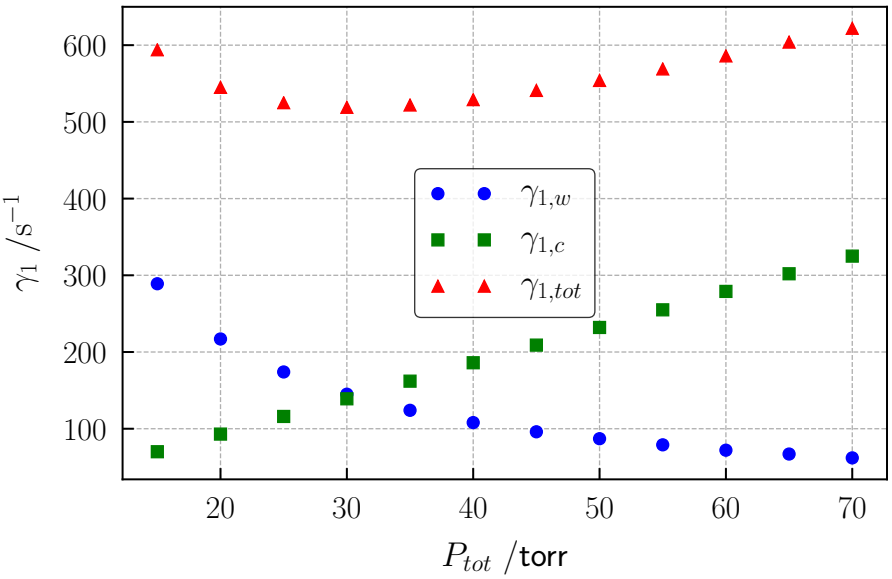

Figure 4.9: Contribution to the relaxation rate γ_1 due to walls collisions ($R = 5\,\mathrm{mm}$, $L = 10\,\mathrm{mm}$), Rb-buffer gas collisions and total relaxation rate (including the spin-exchange term) in the case of Kr-N_2 mixture.

4.1.6 Expected short-term stability budget

In this section, we try to build a theoretical short-term stability budget for the final design in the case of the two buffer gas mixtures. The various effects playing a role in the budget are the ones already highlighted in section 2.2. In particular, we

make use of the signal model theory to evaluate the AM-AM contribution from laser amplitude noise. Regarding the Dick-effect, we assume the phase noise level of our newest synthesis chain, described in detail in [111]. For the shot noise contribution, we would assume the value already expressed in section section 2.2.3 but scaled for the smaller active volume of the cell. We do not have yet a complete model for the FM-AM contribution. The experience on the previous POP prototype suggests that noise enhancement of a factor 2 to 3 with respect to the off-resonance case is to be expected, even with the laser optimally tuned on the minimum of the absorption profile. In the budget, we will consider a phenomenological degradation of a factor 2 with respect to the AM-AM contribution alone. In fact, we expect that higher buffer gas pressure and a consequent larger linewidth absorption profile should mitigate the noise conversion [167]. All the aforementioned terms are summarized in table 4.4.

Table 4.4: Theoretical short-term stability budget for: $T_c = 2.85\,\text{ms}$, $T = 1.5\,\text{ms}$ and $C = 30\,\%$ (Ar mixture); $T_c = 1.75\,\text{ms}$, $T = 1\,\text{ms}$ and $C = 20\,\%$ (Kr mixture).

	Ar:N_2 $\boldsymbol{\sigma_y \times 10^{13}}$	**Kr:N_2** $\boldsymbol{\sigma_y \times 10^{13}}$
AM-AM	1.1	2.2
FM-AM	2.2	4.4
LO Dick-effect	0.4	0.4
Photon shot noise	0.4	1.1
Trans-impedance noise	0.5	1.4
Total $\sqrt{\sum_i \boldsymbol{\sigma_i^2}}$	2.7	5.5

For the argon-nitrogen mixture we expect a total short-term budget close to $3 \times 10^{-13}\ \tau^{-1/2}$, close to the state-of-the-art for these kind of devices, even if a reduction of a factor 8 in the clock cell volume has been adopted, compared to the previous POP clock prototype. In the case of krypton-nitrogen mixture the expected short-term stability is higher of (at least) a factor two. In this case a higher degree of uncertainty is provided by the relaxation of the atomic coherence due to molecule formation, which will set the atomic signal amplitude and decay with increasing Ramsey time. The experimental realization will prove if this approach is feasible for clock application. Nevertheless, is a short-term stability below 1e-12 is proven, this could be acceptable and balanced by the much more favorable properties of the mixture in terms of barometric and thermal sensitivities.

4.2 Experimental realization

The realization of the first prototypes follows the guidelines given by the design process. Since we expected different resonant frequencies for the loaded microwave cavity in the case of quartz and Pyrex cells, we realized two cavities, with slightly different internal radius to for the 2 cases. In this section, more details about the properties of the practical realization are presented. We will summarize common tests and characterization carried out on the cells and on the assembly for the two setups. In particular, the cells are analyzed by means of optical spectroscopy on the D_2 line and the loaded cavity resonance thermal sensitivity is measured. When possible, the results are compared to the predictions of the FEM simulations. After the common tests, we identify the operational setpoints for laser frequency, LO oscillator frequency and temperature of the clock cell for both systems. Finally, a short-term evaluation is presented for both cell arrangements. In both cases, the physics packages have been operated at ambient pressure.

4.2.1 Cavity-cell assembly

The realization of the loaded cavity-cell assembly follows the guidelines expressed in the design phase of section 4.1.2. In Fig. 4.10 the realization of the pieces used for the assembly is shown. We can recognize the $1\,\mathrm{cm}^3$ cell, the cavity body and caps, the under cut-off waveguides, the alumina loading material and the Teflon supports. In the picture, the first thermal shield is included. The shield and the cavity are surrounded by a foil of Kapton heaters. All materials, including the brass screws, are non-magnetic, to avoid static magnetic gradients inside the cavity volume. In Fig. 4.11a the assembled loaded cavity is shown, while in Fig. 4.11b it is compared to the previous realization, with the unloaded cavity. The reduction of size and weight is remarkable.

4.2.2 Optical characterization of the clock cells

In this section, we characterize the two batches of cell by means of optical spectroscopy on the D_2 line. We mainly focus on the $F = 2 \rightarrow F' = 1,2,3$ transitions, which are the ones of interest for the POP clock operation. This analysis has the following objectives: verify the success of the cell filling process and trying to estimate the buffer gas pressure from the measured shift and broadening of the lines. The total buffer gas pressure is a difficult parameter to control during the sealing process of the cell, so it can depart from the nominal value given by the supplier. Conversely, the gas mixture pressure ratio is usually more well defined and we will assume no uncertainty on this parameter.

The experimental setup is very basic: first, we heat the cell by means of a small oven up to around 60 °C. We then send a probe laser beam through the cell.

Figure 4.10: Picture of the building components of the cavity cell assembly. As a dimensional reference, a 10-cent of euro coin is shown.

(a) Assembled loaded cavity.

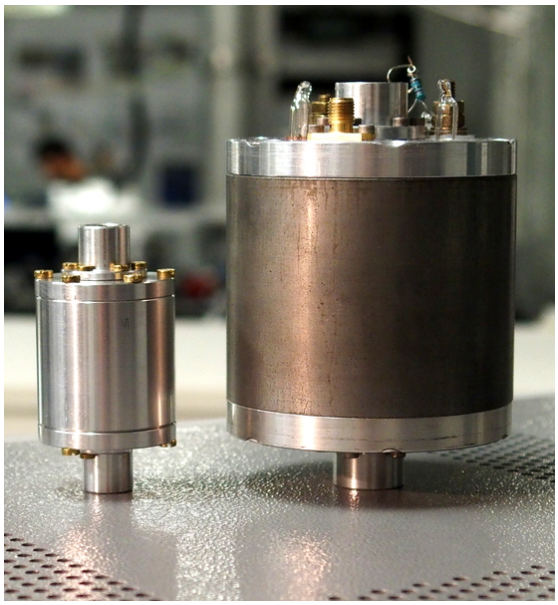

(b) Comparison with the unloaded cavity.

Figure 4.11: (a) Picture of the assembled alumina-loaded cavity. (b) Comparison with the unloaded cavity used in the previous POP prototype.

The output beam is focused onto an amplified Silicon photodiode. We look at the transmitted signal as we sweep the laser frequency with a linear ramp. The input laser is attenuated to few tens of µW, to avoid power broadening and to reduce

background intensity noise. To calibrate the frequency scale, part of the laser light is sent to an evacuated reference cell with no buffer gas. The Doppler-free peaks, detected with a saturated absorption spectroscopy setup serve as a reference for the unshifted atomic transitions.

The line profile is analyzed by the same procedure of [157]. We expect a Gaussian Doppler broadening together with a Lorentzian broadening due to the buffer gas [50]. Since the two broadening mechanisms have comparable magnitude for the temperatures and buffer gas pressure of interest, we need to consider a Voigt profile. Moreover, as the separation of the upper-level hyperfine states ($F' = 1,2,3$) is comparable to the linewidth of the transitions, a best-fit of three superimposed profiles is performed. Thus, the fitting function f_a for the absorption profile has the form:

$$f_a(\nu_L) = c_0 + c_1\nu_L + c_2 \sum_{i=1}^{3} a_i V(\nu_L - (\nu_i + \Delta_{bg});\, \Gamma_{bg}/2;\, \Gamma_D/2) \tag{4.20}$$

In (4.20) c_0 and c_1 are baseline coefficients, to account for a not constant input power (we sweep the laser frequency by changing the current, thus also the input intensity is varied). c_2 is the total absorbance, while a_i is the relative strength of the i-th hyperfine transition. V is the Voigt profile centered in $\nu_i + \Delta_{bg}$, where ν_i is the unperturbed center frequency and Δ_{bg} is the buffer gas shift. Finally Γ_{bg} and Γ_D are the Lorentian and Gaussian FWHM respectively. The Voigt profile is approximated with the function:

$$\begin{aligned} V(x;\, \sigma;\, \gamma) &= \frac{\Re\{w(z)\}}{\sigma\sqrt{2\pi}} \\ z &= \frac{x + i\gamma}{\sigma\sqrt{2}} \end{aligned} \tag{4.21}$$

where $w(z)$ is the Faddeeva function [168]. In the analysis the free parameters are c_0 and c_1, c_2, Γ_{bg} and Δ_{bg}, while the relative strength and positions of the three lines is fixed (as taken from [169]). The Doppler width is also fixed to 540 MHz, corresponding to a temperature of 60 °C. In Fig. 4.12 a typical absorption curve is shown. Two different batches of cells are analyzed. The first batch is composed of two quartz cells with a nominal mixture of 40 torr of Ar-N_2. The cells were manufactured by Precision Glassblowing Inc. (Pennsylvania, US) and filled by Marwan Technology (Pisa, Italy). The second batch is manufactured and filled by Frequency Electronics Inc. (New York, US) and the chosen material is Pyrex 7740. From this batch, three cells are filled with Ar-N_2 and two with Kr-N_2. In table 4.5 the results of the optical analysis is summarized. The shift values are fairly consistent with the expected value calculated using the coefficients in table 4.2 for the nominal mixtures. The broadening instead is generally overestimated. Other broadening mechanisms might be the cause and the uncertainty on the cell temperature was

Table 4.5: Buffer gas-induced shift and broadening for different batches of cells (all values of shift and broadening are in units of MHz). In the last two columns the values of shift and broadening are calculated from the values in table 4.2.

Mixture	**Material**	P_{tot}/torr	Δ_{bg}	Γ_{bg}	Δ_{bg} (th.)	Γ_{bg} (th.)
Ar:N$_2$ (1.6 : 1)	Pyrex	30	-130	690	-173(1)	540(6)
	Pyrex	40	-210	1020	-231(2)	720(10)
	Quartz	40	-265	1160	-231(2)	720(10)
	Quartz	40	-270	-	-231(2)	720(10)
	Pyrex	50	-240	1000	-289(2)	900(10)
Kr:N$_2$ (0.96 : 1)	Pyrex	25	-90	505	-141(3)	450(7)
	Pyrex	40	-195	880	-226(4)	710(10)

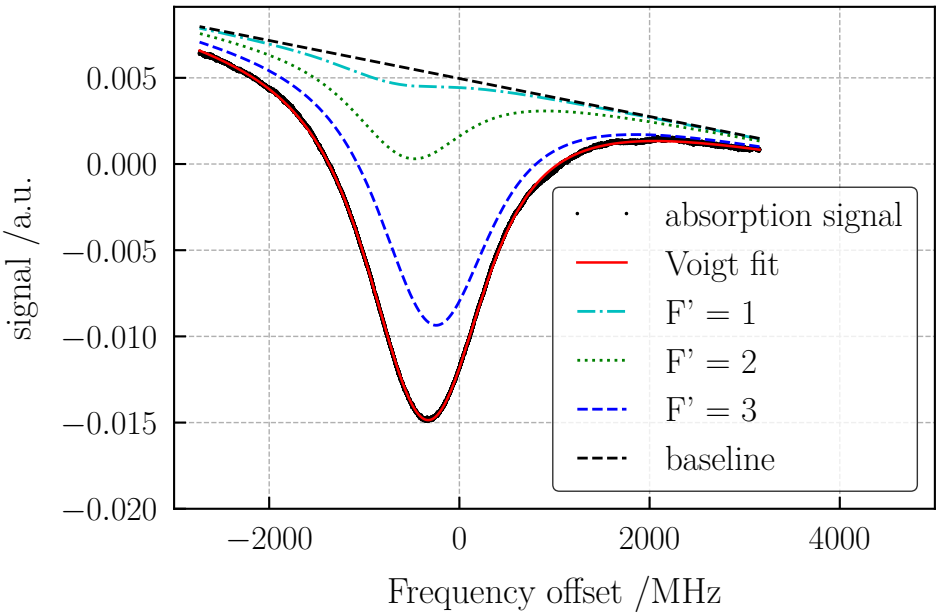

Figure 4.12: Best fit of the absorption line $F = 2 \rightarrow F' = 1,2,3$ for one of the Quartz cell filled with 40 torr of Ar-N_2. A Doppler width of 540 MHz is assumed.

rather large, thus we cannot conclude much from this parameter. With such large profiles, accurate spectroscopy is difficult to perform, thus this analysis is preliminary and mostly qualitative. More precise information about the real buffer gas content can be done with microwave spectroscopy, directly integrating the cell into the clock setup.

4.2.3 Cavity thermal sensitivity and tuning

In this section, we report the measurement of the thermal coefficient of the loaded cavity with the quartz cell. The stability of the cavity resonance is one of the necessary conditions to achieve good long-term performances, as noted in [70, 133]. The measurement has also allowed a coarse tuning of the cavity resonance frequency.

The experimental setup used to investigate the cavity resonance is described in Fig. 4.13. It is composed of a sweep oscillator (HP 8350 B), a circulator, a RF power detector (a GaAs diode). The absolute frequency of the generator is measured with a frequency counter referenced to a hydrogen maser. The cavity assembly is heated by an oven and its temperature is recorded with an NTC thermistor. The cavity resonance profiles are detected by looking at the power reflected from the cavity as a function of the sweep oscillator frequency. In Fig. 4.14 the center frequency

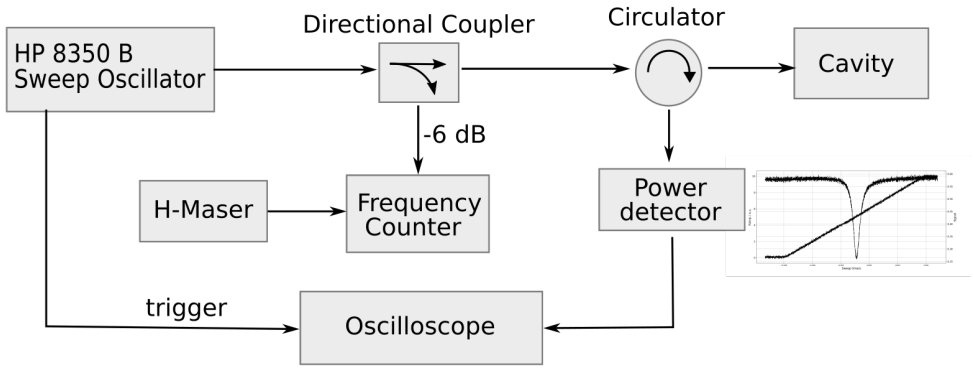

Figure 4.13: Measurement scheme for the analysis of the microwave cavity resonance modes.

of the pseudo-TE_{011} is plotted as a function of the cavity temperature. In the first measurement, the cavity internal dimensions are the nominal ones as given in section 4.1.2. The resonance frequency at the desired working point (around 65 °C) is found to be 22 MHz lower than the Rb atomic frequency and around −120 MHz from the design value (the simulated frequency was set conservatively to be 100 MHz higher than the atomic frequency). The discrepancy is accountable to a 1 % uncertainty on the materials dielectric and/or geometrical properties. To align the cavity resonance to the atomic one, tuning of the cavity was performed, by shortening its length by 1.02 cm. The second curve in Fig. 4.14 refers to the tuned cavity. The resonance frequency, at 65 °C, lies within one MHz from the atomic frequency. A finer tuning will be performed when the operational point (at the buffer-gas inversion point) is assessed.

The thermal sensitivity is found to be $-470\,\mathrm{kHz\,K^{-1}}$ for the untuned cavity and $-460\,\mathrm{kHz\,K^{-1}}$ for the tuned cavity. These values in excellent agreement with the FEM simulation of section 4.1.3 for the combined sensitivity of the Aluminum and of the sintered alumina. Based on that agreement, we can conclude that the contribution from the Al_3O_2 (95 % purity) alone is around $-280\,\mathrm{kHz\,K^{-1}}$.

While performing the resonance analysis, we also analyzed the cavity quality factor. The measured values are shown in Fig. 4.15. We can observe that it slightly decreases at higher temperatures, probably due to metallic deposition of the Rb inside the electromagnetic mode volume. Nevertheless, the Q-factor is rather high, even for the fully assembled loaded cavity and stayed above 3000 at all operating temperatures.

Regarding the sensitivity and tuning of the cavity assembly with Pyrex cells, the measurement is intrinsically less accurate due to the larger quality factor. The latter is found to be around 800. Nevertheless, the sensitivity of the cavity mode

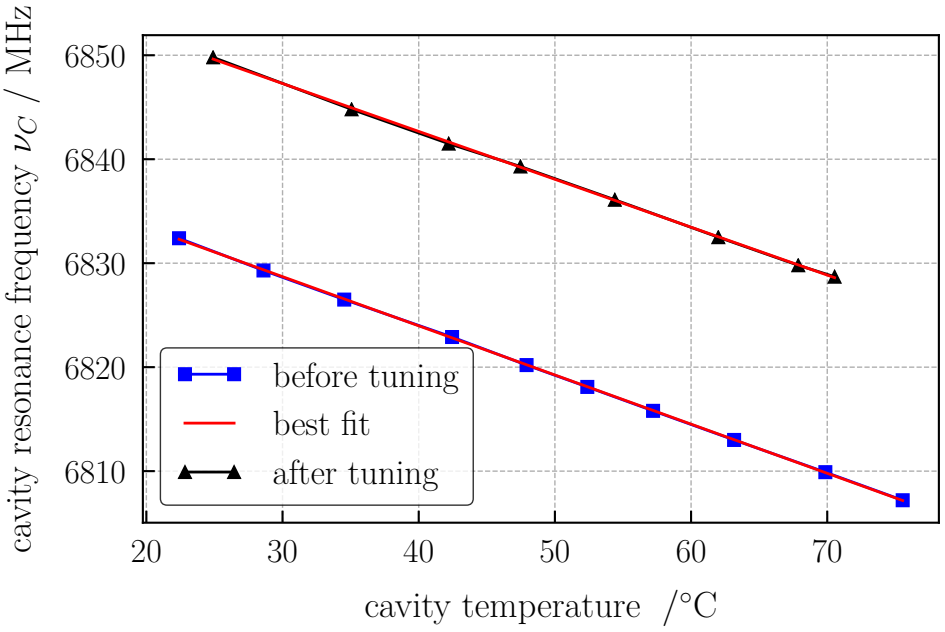

Figure 4.14: Measured cavity resonance for the TE_{011} mode as a function of the cavity temperature.

to temperature is of the same order of magnitude, dominated by the cavity and alumina contributions. As in the previous case, the measured absolute frequency of the cavity mode is around 120 MHz lower than the value predicted by the FEM simulation, thus a tuning of the cavity resonance, executed by shortening the cavity length, was performed.

4.2.4 Argon-nitrogen system - Operational setpoints

In this section, the operational setpoints for the laser and LO frequencies are identified and discussed. Moreover, the absolute frequency of the clock is measured as a function of the cell temperature. The latter analysis allows us to find the expected inversion point for the buffer-gas shift that corresponds to the operational temperature, where the standard is maximally insensitive to temperature variations. The measurements provide the expected temperature sensitivity coefficient due to the buffer gas, that can be compared to the literature value.

Microwave frequency tuning

The first operation to be performed on the new physics package is the LO oscillator tuning on the atomic frequency. The spectroscopy of the hyperfine clock

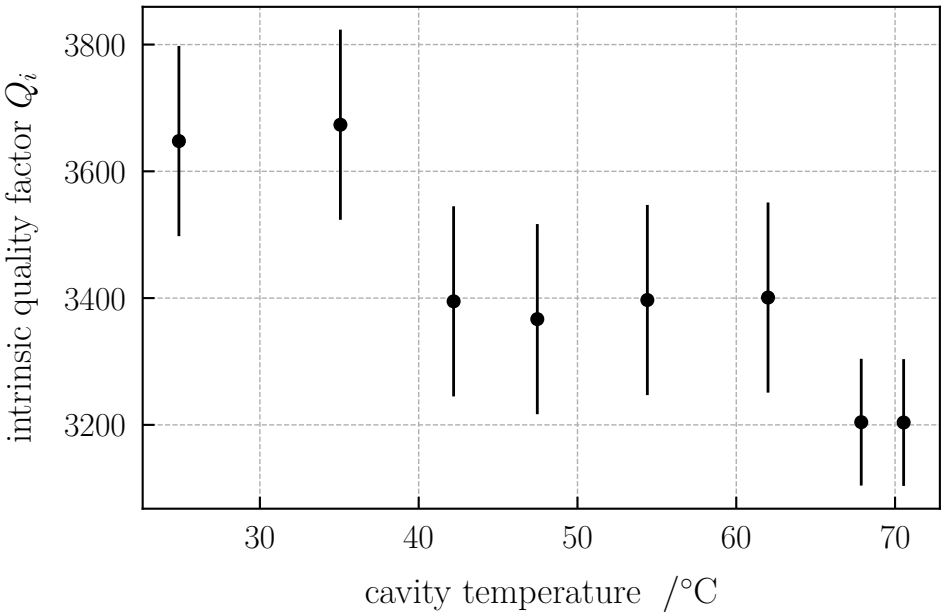

Figure 4.15: Measured intrinsic cavity quality factor (Q_i) for the loaded cavity with Quartz cell as a function of the cavity temperature.

transition can give a more accurate estimate of the total buffer gas pressure present in the cell used in the final setup. To perform the spectroscopy, the LO is tuned to 10 MHz with an accuracy of 6×10^{-10}. This corresponds to an accuracy of 4 Hz at the atomic frequency. A Ramsey spectroscopy is performed to find the resonance center. A typical scan of the resonance obtained during this phase, performed with a Ramsey scheme, is shown in Fig. 4.16. Following this procedure, we experimentally determined the frequency of the $|F = 1, m_F = 0\rangle \rightarrow |F = 2, m_F = 2\rangle$ transition as:

$$\nu_0^{exp.} = 6\,834\,691\,166(4)\,\text{Hz}$$

which, given the unperturbed frequency $\nu_0 = 6\,834\,682\,611$ Hz, corresponds to a total buffer gas shift of:

$$\Delta\nu_0 = 8555(4)\,\text{Hz}$$

This value is rather far from the expected 7.0(2) kHz shift for the nominal 40 torr total sealing pressure. We can consider the buffer gas composition as reliable since the mixture was prepared in a gas tank and the buffer gas was injected already mixed during the cell-filling process. Moreover, if we attribute the discrepancy to the gas composition, we get an unlikely 25 % error in the ratio of the partial pressures. From these considerations, it is more likely that the discrepancy is due to an error in the total pressure, due to temperature uncertainty occurring in the filling-process altering the pressure readings.

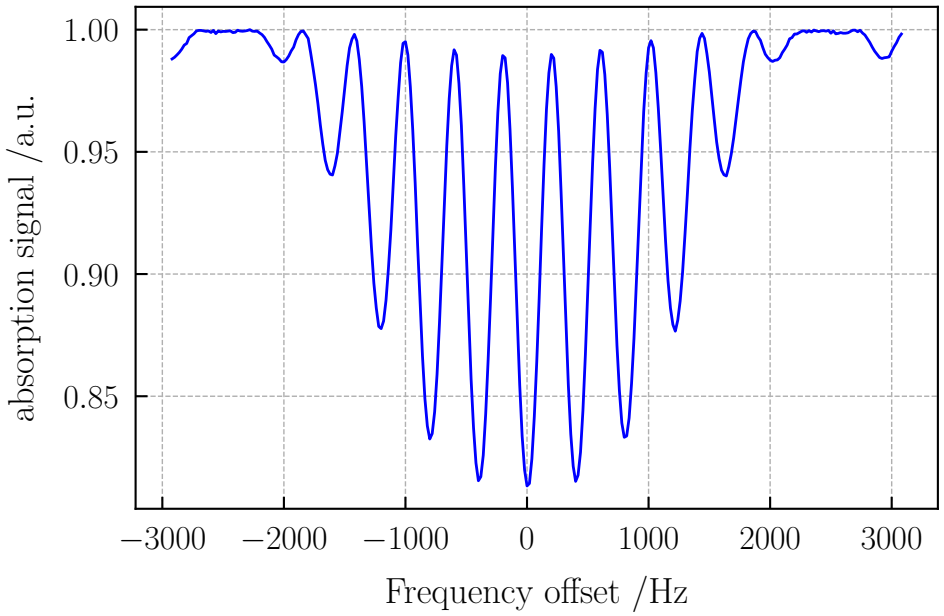

Figure 4.16: Ramsey scan of the 0-0 microwave transition. The synthesizer frequency is set to 6 834 691 166(4) Hz. Average of 5 scans, free-evolution time $T = 2.0$ ms, Rabi pulses length $t_1 = 0.4$ ms. Cavity temperature is 61 °C.

From the measured shift value, we can thus estimate the total buffer gas pressure for this particular cell to be 49(2) torr.

Laser frequency locking point

The laser frequency is locked to the Doppler-free reference peak which corresponds to a minimum of the transmitted intensity for the clock cell. At this frequency the FM-AM conversion is also minimized, thus the short-term stability is the lowest. Compared to the clock cell described in section 2.1.1, which shares the same buffer-gas composition but 25 torr of total pressure, the operational point for laser frequency is shifted by −136 MHz, which is consistent with the expected differential shift Δ_{bg}(49 torr)-Δ_{bg}(25 torr) = −139(3) MHz as calculated from table 4.2. This is another confirmation of the fact that the total pressure for this particular cell is 20 % higher than the nominal value. In Fig. 4.17 the clock absorption profile is shown, superimposed to the reference cell signal.

Thermal sensitivity and operational temperature

In this section, we determine the optimal operational setpoint for the cell temperature. The optimum coincides with the inversion point of the frequency shift

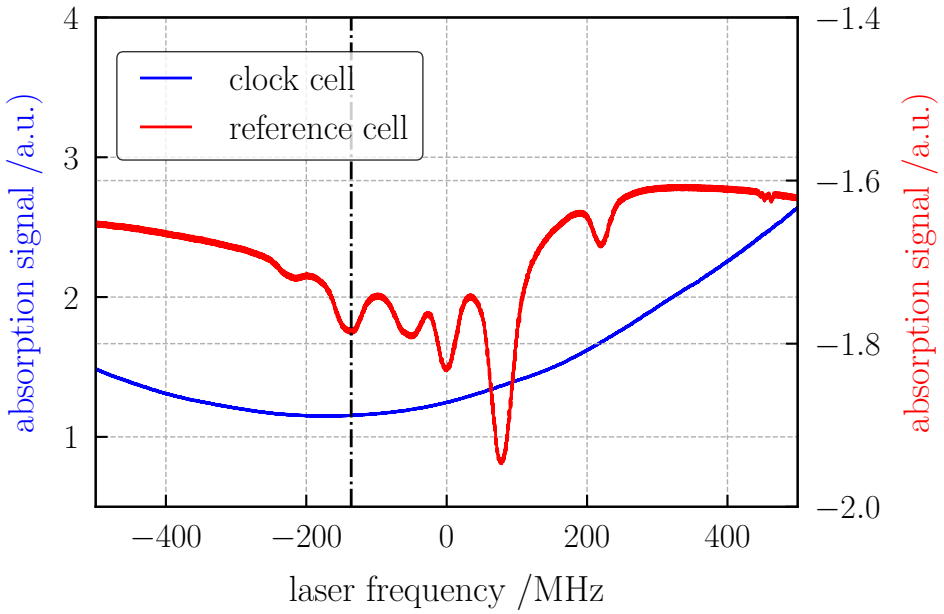

Figure 4.17: Absorption profile of the clock cell compared to the spectroscopy signal from the external reference cell. The clock branch is shifted by −80 MHz with respect to the reference branch. The zero of the frequency axis corresponds to the locking point of the clock cell filled with 25 torr Ar-N_2, while the dashed line corresponds to the locking point for the 49 torr Ar-N_2 cell.

induced by the buffer gas. We change the temperature of the cavity (and thus of the clock cell) in steps, let the system thermalize, and perform a frequency measurement at each step. The stem temperature is varied by the same amount as the cavity, keeping the differential temperature constant. We neglect the frequency shift due to Rb density variation (via spin-exchange), since it is at least one order of magnitude smaller [127, 131]. In Fig. 4.18 the frequency measurements as a function of the cavity temperature are reported. From this characterization we extrapolated an operational setpoint $T_0 = 66.0(5)\,°C$. From the fit we extract the γ quadratic coefficient which is found to be $-7 \times 10^{-12}\,K^{-2}$. Assuming a total buffer gas pressure of 49 torr, this corresponds to $-0.001\,Hz/(torr\,K^2)$, in reasonable agreement with the calculated value from table 4.1. From this data, by operating the clock around T_0 and assuming a conservative uncertainty of 1 K on the ability to operate around the ideal setpoint, we would expect a temperature sensitivity for the clock transition of $1.4 \times 10^{-11}\,K^{-1}$.

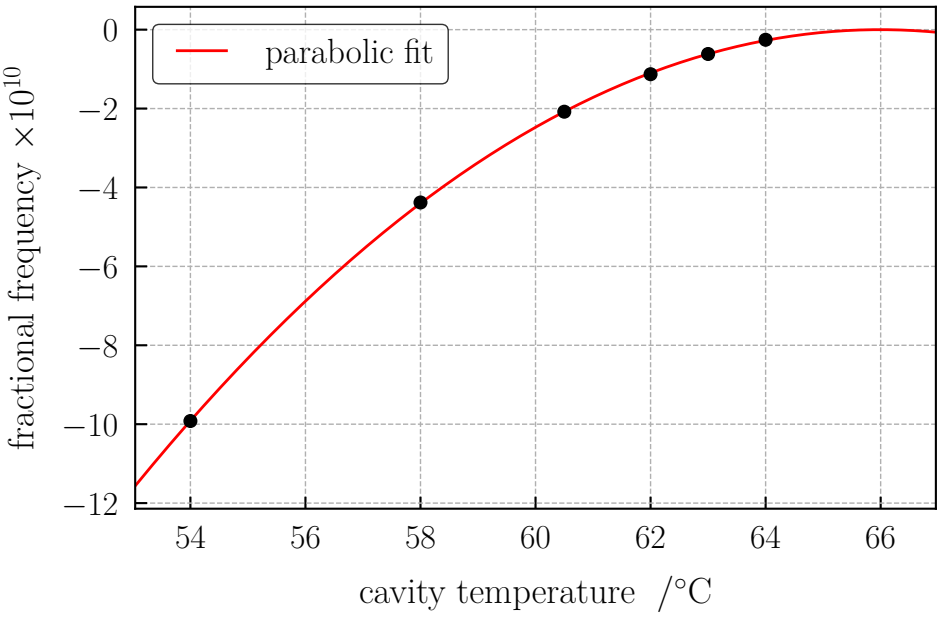

Figure 4.18: Clock frequency as a function of cavity temperature.

4.2.5 Argon-nitrogen system - short-term characterization

Relaxation times measurement

To determine the optimal free-evolution time and to further characterize the physical properties of the atomic system, it is useful to estimate experimentally the relaxation terms. In particular, an easily accessible parameter is γ_1 or, equivalently, its inverse T_1. The latter is the relaxation time of the clock state population, which can be measured with the Franzen method [161, 170]. The atomic sample is optically pumped to the hyperfine ground state $F = 1$ by means of a strong laser pulse resonant with the $F = 2$ state. Then, the laser is shut down and the system is let to evolve in the dark for the time T_{dark}. Finally, the population of the $F = 2$ state is probed with a weak and short laser pulse (by looking at the transmitted intensity through the vapor). The pattern timing is shown in Fig. 4.19. Of course, this method does not discriminate between Zeeman sublevels, thus T_1 is a collective parameter. Nevertheless, considering that during binary collisions with the buffer gas, the collision time is much shorter than the hyperfine precession time, the decay to any of the Zeeman sublevels of any of the two ground-state manifolds happens with equal probability. Thus the collective parameter is representative of any Zeeman pair with $\Delta m_F = 0$ (including the clock transition). A typical set of data obtained with this method is shown in Fig. 4.20. The dark time is varied from 2 ms to above 10 ms. The relaxation of the population (proportional to the decrease

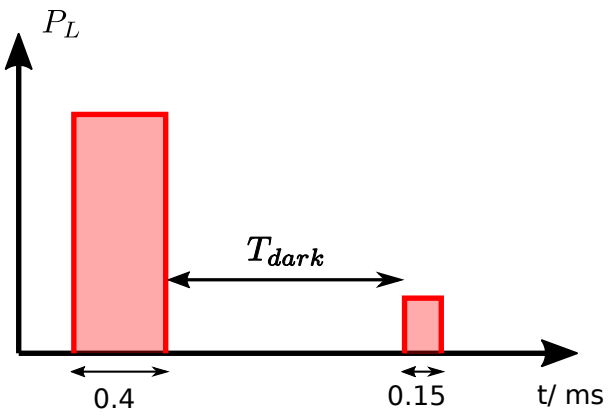

Figure 4.19: Pattern timing for the T_1 measurement with Franzen method. Laser Power P_L is 3 mW for the pumping pulse and 200 µW for the probe pulse.

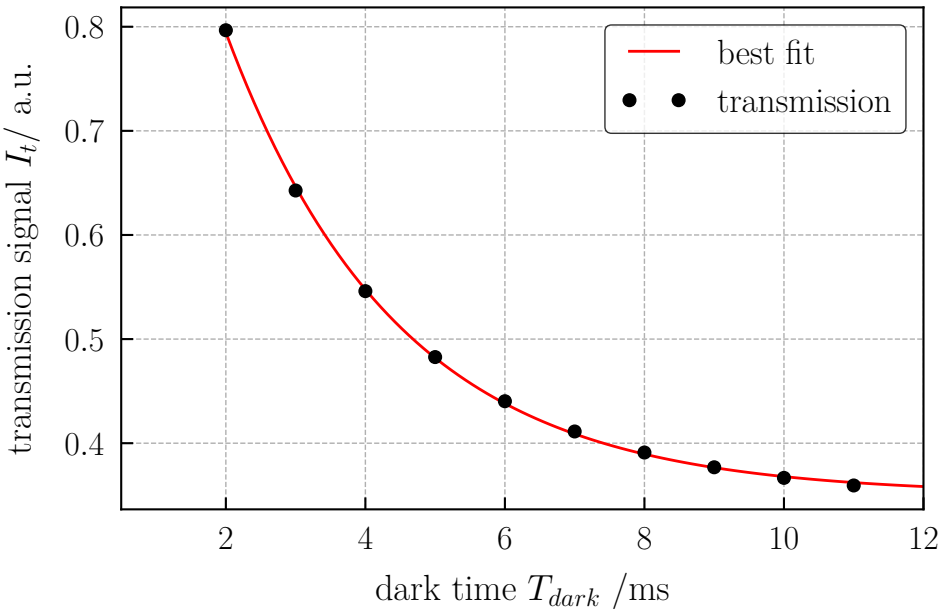

Figure 4.20: Typical relaxation of the atomic population of the level $F = 1$. Stem temperature is 58 °C. In this case the relaxation time T_1 is 2.5(2) ms.

in the transmitted signal I_t) as a function of the dark time is well described by a single exponential of the form:

$$I_t = A + B \exp \frac{-T_{dark}}{T_1} \tag{4.22}$$

We repeated the measurement for different cell temperature around the expected working setpoint. The stem temperature is varied accordingly and maintained 3 K below. In Fig. 4.21 the T_1 estimates at the various temperatures are put together. As a comparison, also the values calculated from the literature (as in section 4.1.5) are shown. The relaxation term which is mostly dependent on temperature is the spin-exchange term $\gamma_{1,se}$. To calculate the expected value of $\gamma_{1,se}(T)$ the numerical density $n(T)$ for Rb in vapor phase is taken from [50]. The collisional term $\gamma_{1,bg}$ is also weakly dependent on temperature through the mean relative velocity between Rb and the buffer gas atoms (or molecules), and this factor is taken into account as well. The experimental data and the calculation agree quite well, even though the

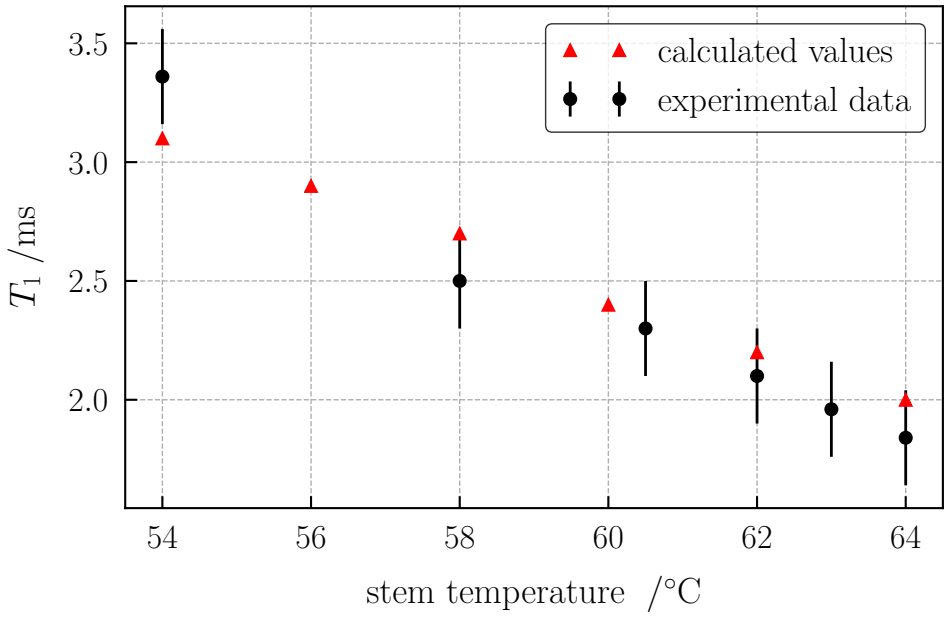

Figure 4.21: T_1, as estimated with Franzen method, compared with the theoretical values calculated with the use of the relaxation rates found in the literature and from the available experimental parameters. The cavity temperature is kept 3 K above the stem temperature.

latter seems to show a stronger dependence on temperature. It is to be noted that the experimental estimate is susceptible to spatial inhomogeneities both in the (x, y) plane (through Gaussian laser profile) and in the z-direction, due to absorption as the laser propagates through the cell.

Estimating the clock state coherence relaxation time T_2 is less straightforward since with the optical detection we have direct access only to the atomic populations. Nevertheless, we can deduce if T_2 is bigger or smaller than T_1 by looking at the shape of the Ramsey fringes. As noted in [106], the shape of the envelope

of the Ramsey fringe has positive concavity if $T_1 < T_2$ and negative concavity in the opposite case. This is shown in Fig. 4.22, where the Ramsey fringes are theoretically computed for the simplified 3-level system (as in [106]) for the two cases. From the shape of experimental the Ramsey fringes (see for example Fig. 4.16), we can conclude that T_2 is smaller than T1, and in the range 1.5 ms to 2.0 ms at the operational temperature.

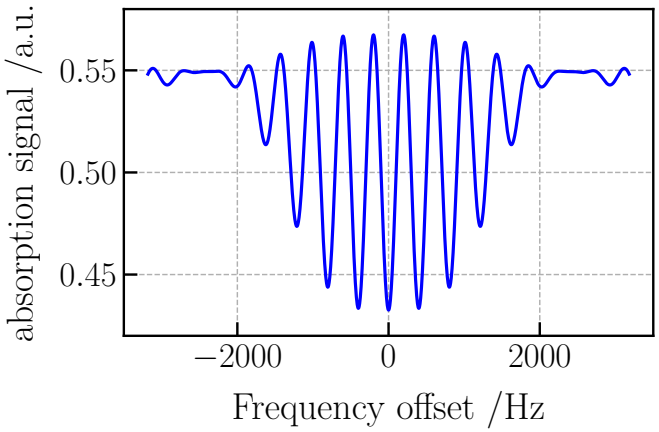

(a) Computed Ramsey fringes with $T_1 = 1.8\,\text{ms}$, $T_2 = 2.5\,\text{ms}$.

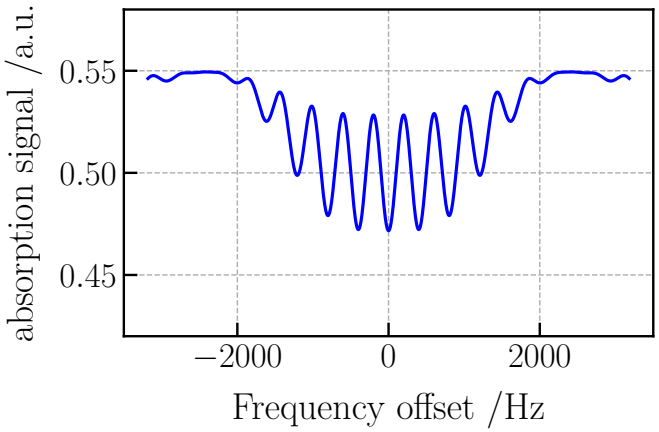

(b) Computed Ramsey fringes with $T_1 = 1.8\,\text{ms}$, $T_2 = 1.2\,\text{ms}$.

Figure 4.22: Comparison of Ramsey scan with the same T_1 and different T_2. Ramsey time = 2.4 ms for both.

Short-term optimization

The power and duration of the pump pulse are chosen in order to achieve saturation of the pumping efficiency. A good combination, given the power availability, is found to be $t_p = 0.4\,\text{ms}$ and $P_p = 4\,\text{mW}$. The optimization of the other parameters is carried out mainly by looking at the slope of the clock frequency discriminator as a figure of merit. Indeed the main parameters p_i, such as free-evolution-time, detection pulse length and power levels, influence the error signal slope $D_e = \partial E/\partial\nu$, where:

$$E(p_i;\nu) = S(p_i;\ \nu - \nu_m) - S(p_i;\ \nu + \nu_m) \tag{4.23}$$

and S is the detected absorption signal integrated over the detection window τ_d. ν_m is the microwave modulation depth, which is chosen to be at half-width-half-maximum of the central Ramsey fringe. Indeed, as noted in section 2.2, we expect the main short-term contributions to scale as a function of the parameter $1/D_e$.

As an example, we report the optimization of the free-evolution time T in Fig. 4.23. As expected, the maximum achievable frequency discriminator is obtained for $T \simeq T_2$.

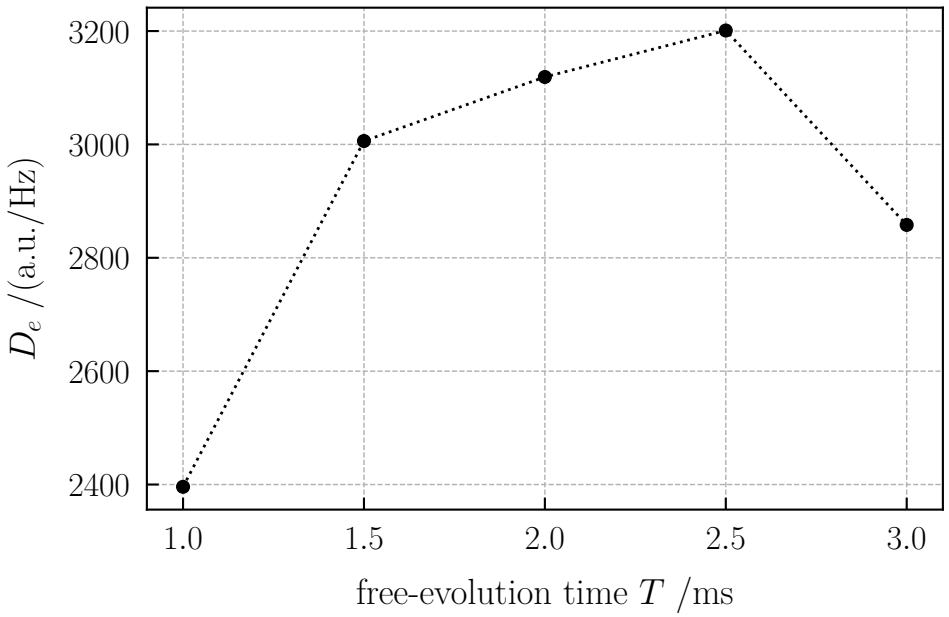

Figure 4.23: Clock error signal slope D_e as a function of the free-evolution time T.

Short-term stability: results

After this rough optimization of the power levels and of the clock timing, we selected the following parameters: Pumping time $t_p = 0.4\,\text{ms}$, Rabi pulse length $t_1 = 0.4\,\text{ms}$, free-evolution time $T = 2.5\,\text{ms}$, detection time $\tau_d = 0.15\,\text{ms}$. Pumping pulse peak power $P_p = 4\,\text{mW}$, detection pulse peak power $P_{det} = 200\,\mu\text{W}$. The microwave pulse area at atoms location is set close to $\pi/2$ by means of a Rabi oscillations measurements. The modulation depth ν_m is set to $\pm 85\,\text{Hz}$. With this configuration we steadily achieved a short term stability of $4.6 \times 10^{-13}\ \tau^{-1/2}$ (see Fig. 4.24). The medium-long term stability suffers from a strong linear drift

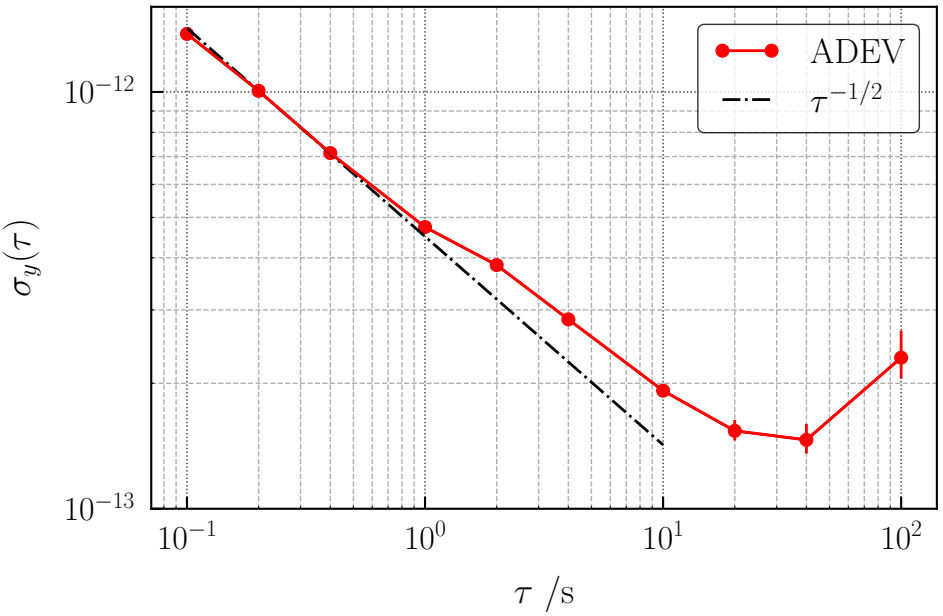

Figure 4.24: Short-term stability of the Ar-N_2 setup.

($-2.3 \times 10^{-15}\,\text{s}^{-1}$). The origin of this drift is under investigation, and it is probably accountable for a change in the chemical properties of the clock cell (mainly the buffer-gas content). Nonetheless, in this phase, we are mostly interested in validating the setup in the short-term. For the long-term, it would be more interesting to evaluate in detail the performances with the krypton mixture since it presents the most favorable thermal coefficients. The short-term analysis presented here can be used as a benchmark to understand the contribution from the wall collisions for the $1\,\text{cm}^3$ cell, since the two systems share the same geometry.

4.2.6 Krypton-nitrogen system - Operational setpoints

Microwave frequency tuning

Following the same procedure of section 4.2.4, we determined the frequency of the $m_F = 0 - m'_F = 0$ transition:

$$\nu_0^{exp.} = 6\,834\,682\,199(5)\,\text{Hz}$$

which, given the unperturbed frequency $\nu_0 = 6\,834\,682\,611\,\text{Hz}$, corresponds to a total buffer gas shift of:

$$\Delta\nu_0 = -410(5)\,\text{Hz}$$

This value is rather consistent with the expected $-600(300)\,\text{Hz}$ absolute shift calculated with the values from the literature (see table 4.1) for a 0.96:1 ratio mixture. The measured shift corresponds to the following beta coefficient:

$$\beta' = -10(1)\,\text{Hz}\,\text{torr}^{-1}$$

This is a reduction of a factor 17 with respect to the traditional Ar-N_2 mixture [107]. The environmental sensitivity to temperature due to buffer gas migration to and from the cell stem and due to the barometric effect can in principle be mitigated by the same amount.

Laser frequency locking point

As in the previous case, the preferred locking point for the laser frequency is located at the minimum of the absorption profile of the clock cell. This detuning yields both to maximum contrast of the Ramsey fringes and to minimize the FM-AM noise conversion. The optimal locking point is found with the laser locked on the crossover peak $F = 2 \rightarrow F' = 1{,}2$ on the external saturation spectroscopy setup, with the clock branch shifted by $-80\,\text{MHz}$ with respect to the reference branch. This is in agreement with the expected red-shift of the D_2 transition, that for the Kr-N_2 mixture ($P = 40\,\text{torr}$) is calculated from table 4.2 to be $-226(5)\,\text{MHz}$.

Thermal sensitivity and operational setpoint

The operational setpoint is determined by scanning the temperature of the cavity (and thus of the clock cell) with a slow ramp. During the ramp, the clock is operated with the LO locked on the atomic transition and its frequency is measured with respect to a hydrogen maser. The result is shown in Fig. 4.25. By performing a parabolic best fit of the above data, we get the following curvature:

$$\gamma' = -4 \times 10^{-12}\,\text{K}^{-2}$$

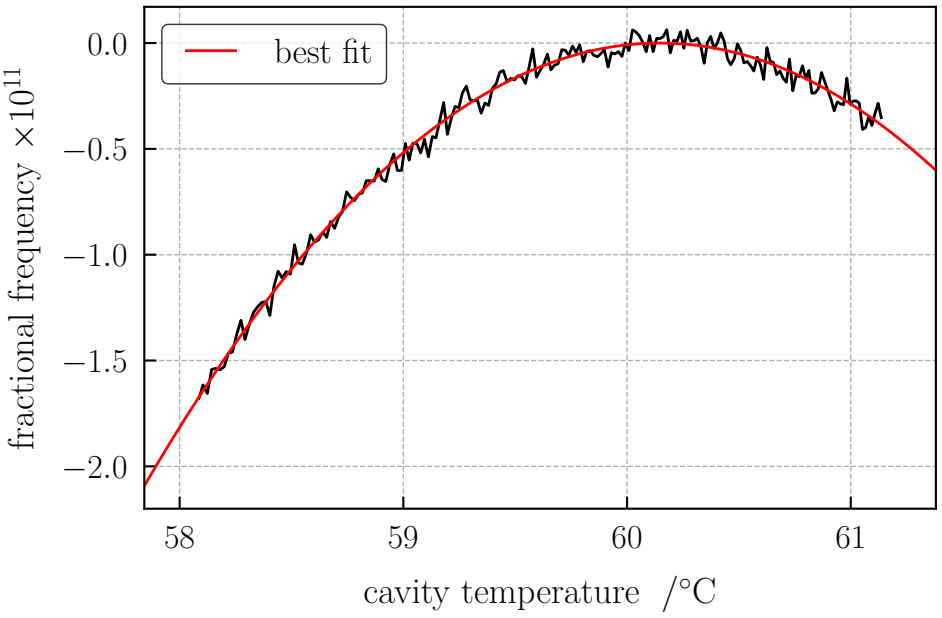

Figure 4.25: Clock frequency as a function of the cavity temperature for the 40 torr Kr-N_2 cell. The vertex of the parabola corresponds to an absolute frequency of 6 834 682 199(5) Hz.

Assuming a total buffer gas pressure of 40 torr, we can also express this coefficient as:

$$\gamma' = -0.0007\,\mathrm{Hz\,torr^{-1}\,K^{-2}}$$

which is an intrinsic property of the mixture (with 0.96:1 Kr:N_2 ratio). The value is comparable to the non-linear coefficient of the 1.6:1 Ar:N_2 mixture. To our knowledge, a value of γ' for a Krypton mixture was not present in the literature. The measurement was possible thanks to the high resolution of the POP scheme, together with its intrinsic reduction of light-shift. A temperature-dependent light shift could, in fact, induce a strong bias in this kind of measurement. The other piece of information extracted from this measurement is the operational temperature corresponding to the vertex of the parabola. This is found to be 60.1(5) °C.

4.2.7 Krypton-nitrogen system - short-term characterization

Relaxation times measurement

As in the case of the other mixture, the population relaxation rates are estimated with the Franzen method. By this means, we estimate a relaxation time T_1 =

1.0(1) ms with the cavity temperature set at 60 °C. By looking at the Ramsey fringes (Fig. 4.26) acquired with this setup, we notice that the coherence relaxation rate γ_2 is higher than γ_1 at the operational temperature, resulting in a strong concavity of the Ramsey fringes envelope. This is expected due to the relaxation of the hyperfine coherence from van der Waals molecule formation between Kr and Rb, but it was not quantified in the design phase due to the lack of information in the literature. In the following we will experimentally estimate the values of the relaxation rates for the krypton-nitrogen mixture. Having an estimate of γ_2

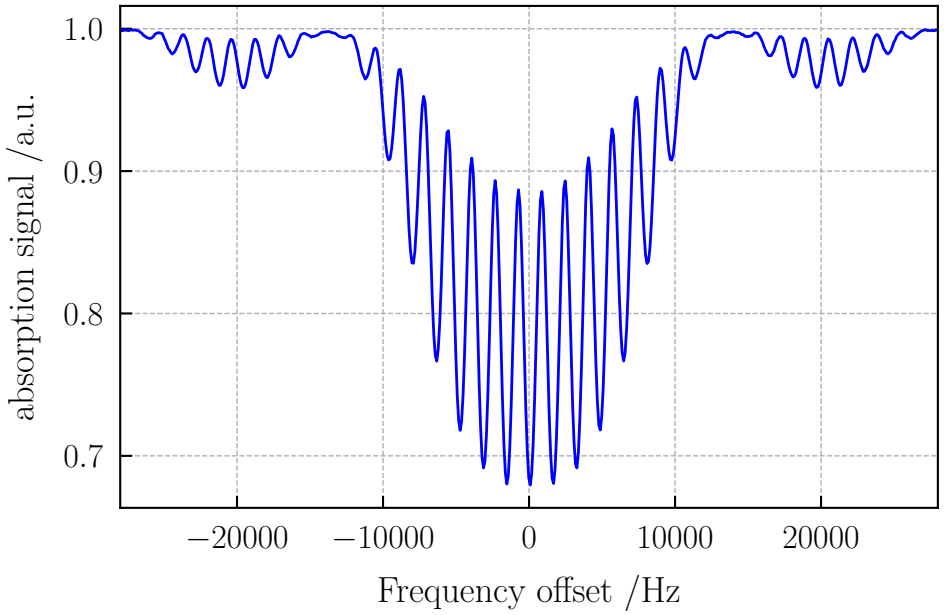

Figure 4.26: Ramsey fringes for the Kr:N_2 system. Cavity temperature 60 °C. Pattern parameters: Pumping time $t_p = 1.5$ ms, Rabi pulse length $t_1 = 0.07$ ms, free evolution time $T = 0.5$ ms, detection time $\tau_d = 0.15$ ms.

(and consequently T_2) is also useful to establish the optimal clock timings (and in particular the free-evolution time). One way to obtain this parameter, for the pulsed clock with optical detection, is to look at the contrast of the central Ramsey fringe C. Indeed, for small detuning from center of the atomic resonance, the envelope of the Ramsey fringes is almost independent from T_1, while it strongly depends on the coherence relaxation rate. We can thus look at the contrast of the central Ramsey fringe and approximate the behavior of this parameter as a function of the Ramsey time ($T_R = T + t_1$) with a single exponential as:

$$C(T) = C_0 \exp\left(-T_R/T_2\right) \tag{4.24}$$

To avoid distortion of the profile due to the Rabi envelope [171], we set the Rabi pulse length to be 1/10 of the free-evolution time. A typycal set of data obtained with this procedure is shown in Fig. 4.27. At the operational temperature of the

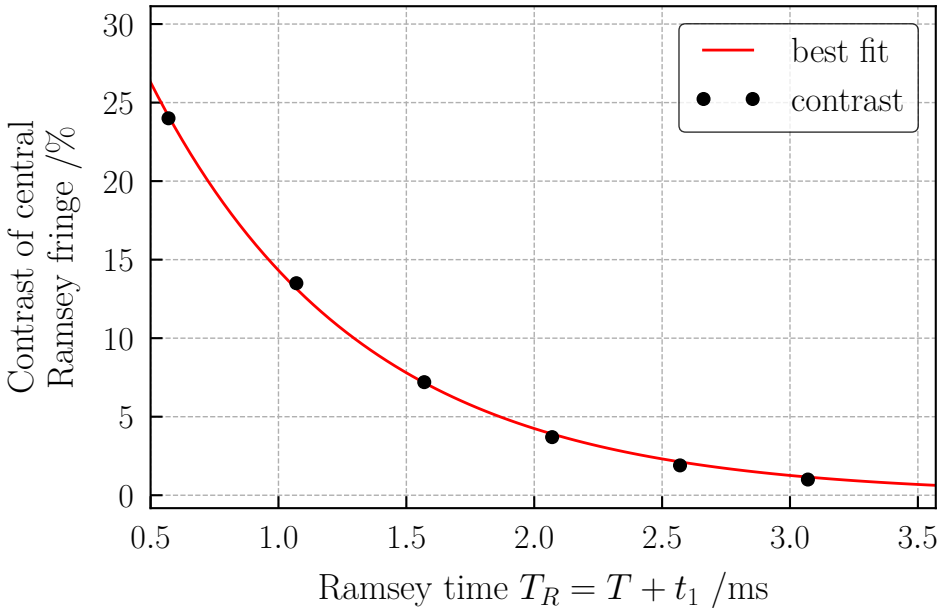

Figure 4.27: Decay of the contrast of the Ramsey fringes as a function of the Ramsey time T_R for a cell temperature of 62 °C.

clock we estimate a coherence relaxation rate around $T_2 = 0.8(2)$ ms. This value implies a clock cycle time of the order of 1 ms, still within the electronics capabilities. In the following sections the impact of this parameter on the short-term optimization is highlighted.

Short-term optimization

Similarly to section 4.2.5, here we present the optimization of the clock short-term stability by tuning the main experimental parameters. The clock frequency discriminator is again considered as the preferred figure of merit. Since we expect to use a shorter free-evolution time due to augmented relaxation of the groundstate coherence, the duration of the Rabi pulses is no longer negligible. For this reason, we consider the Ramsey time ($T_R = T + t_1$) as a more meaningful parameter with respect to the free-evolution time T. When T is changed, t_1 is scaled accordingly. In table 4.6 the slope of the clock error signal, as well as the central-fringe contrast, are shown. The discriminator D_e increases by shortening the Ramsey time as a consequence of the augmented contrast. In Fig. 4.28, the contrast of the central

Table 4.6: Slope of the clock error signal (D_e) and fringe contrast (C) as a function of the Ramsey time.

T_R /(ms)	T /(ms)	t_1 /(ms)	ν_m /Hz	C /%	D_e /(a.u./Hz)
1.65	1.5	0.15	±150	7.0	1667
1.1	1.0	0.1	±225	14.9	2997
0.825	0.75	0.075	±300	21.4	3800
0.56	0.5	0.06	±450	26.8	4410

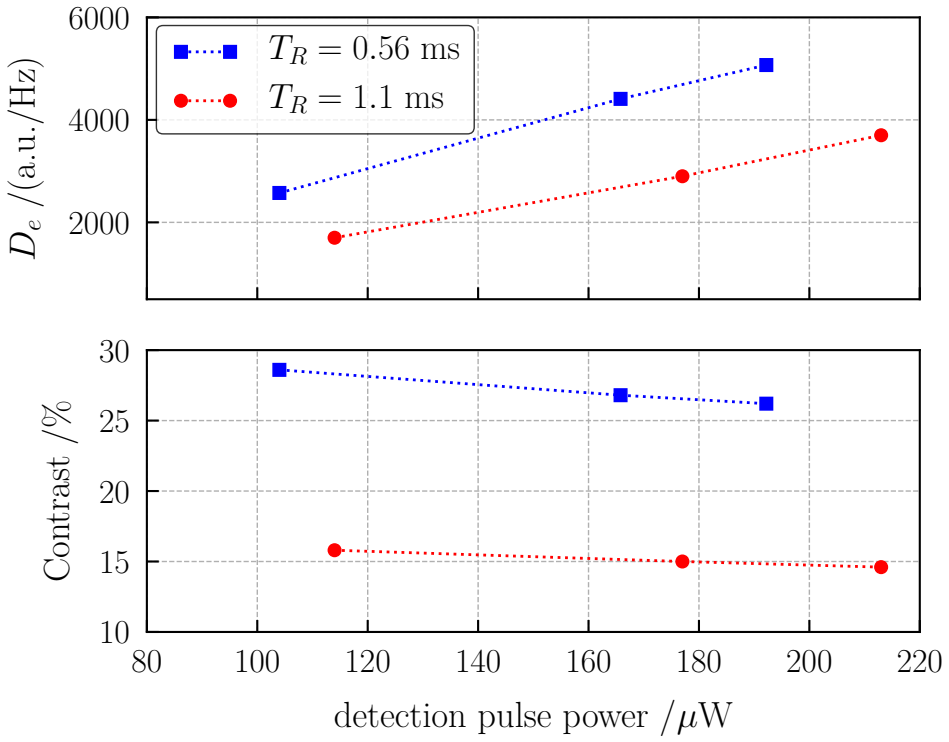

Figure 4.28: Optimization of the detection power for the Kr-N_2 mixture.

Ramsey fringe and the slope of the clock's frequency discriminator (D_e) are shown as a function of the detection power. Two different Ramsey times, that will be used in the following section, are considered. In both cases, we notice a slight decrease in the contrast as a function of the detection power, while the discriminant

increases by a factor 2, passing from $P = 100\,\mu W$ to $P = 200\,\mu W$. Even though the discriminator signal increases as a function of the detection power, we prefer not to raise the power to more than $200\,\mu W$ to avoid optical pumping effects that are likely to enhance the detection noise. This value is thus set as the operational parameter.

Short-term stability: results

Based on the results of the physical characterization, we tested two pattern configurations: one with 0.56 ms Ramsey time and one with 1.1 ms Ramsey time (total cycle time 0.95 ms and 1.78 ms respectively). Rabi pulses duration is 0.06 ms and 0.1 ms respectively. The detection time and power is the same (0.15 ms and $200\,\mu W$) in the two cases, thus the contribution from detection noise is similar (only aliasing effect play a role). The optical pumping rates are also the same, thus the difference in contrast levels is due to the relaxation only. The modulation depth is optimized following to the guidelines of table 4.6. Given these considerations, the comparison between the two obtained stabilities is a fair one.

The stability results are shown in Fig. 4.29. In the case of 1.1 ms Ramsey time, we have a stability $\sigma_y(\tau) = 7.2 \times 10^{-13}\,\tau^{-1/2}$, while in the case of the shorter sequence we have $\sigma_y(\tau) = 5.2 \times 10^{-13}\,\tau^{-1/2}$.

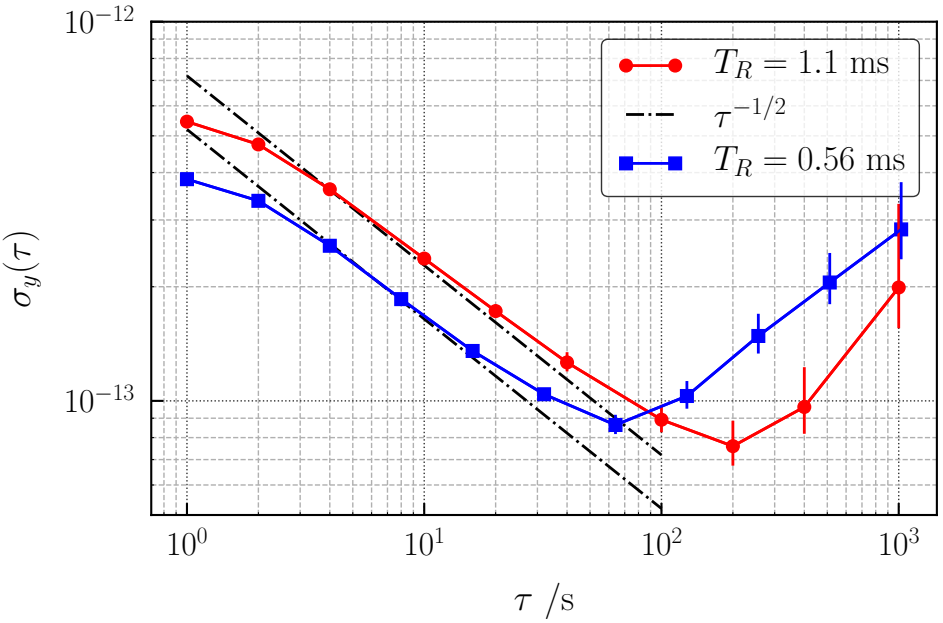

Figure 4.29: Short-term stability of the Kr-N_2 setup with two different Ramsey times.

Even though the best short-term stability is achieved with the shorter sequence, in that case the line quality factor Q_a is halved. In general, retaining a high atomic quality factor is preferred when dealing with longer measurement times. Indeed, some of the long-term sensitivities scale as $1/Q_a$ [127]. Moreover, since the Rabi-pulses duration is shortened, the Rabi envelope is broadened. To avoid line-pulling on the clock resonance from the neighbor magnetic transitions, the quantization magnetic field must be increased accordingly. Increasing the bias field, in turn, increases the sensitivity of the clock to the quantization field and to external magnetic fields (see also section 5.4.2). This poses more stringent constraints on the stability of the quantization field current generator and on the minimum attenuation of the external fields that must be provided by the magnetic shields. When a detailed evaluation of the mid-term properties of the prototype will be carried out, these aspects will be considered more thoroughly and the optimal pattern timing will be chosen.

Chapter 5

First tests on an engineered POP physics package for space applications

In this chapter, some aspects of the activity carried out with Leonardo S.p.A. are reported. The project aims at developing a Rb space-qualified clock based on the pulsed laser technique. The project, co-funded by the Italian Space Agency (ASI) and under the supervision of the European Space Agency (ESA), foresees the development of a physics package in a first phase, to be completed with the realization of the optics and electronic units in a second phase. In the following, the main scientific and technological goals of the project are summarized and the general framework of the activity is described. Moreover, the short-term characterization of the first two realized physics packages is presented, together with an assessment of the magnetic sensitivity. The preparation of a setup to perform the foreseen thermo-vacuum tests is also described, together with a description of the tests procedure.

5.1 Project framework

The project lies within the frame of an ESA General Support Technology Programme (GSTP), a set of initiatives and funded (or co-funded) programs aimed at developing cutting-edge space technologies. The agency's role is to facilitate and coordinate innovative projects within European industries, with the ultimate goal of releasing products that would facilitate the future space mission and related activities. This is achieved by strengthening the companies know-how and capabilities, endorsing the cooperation with research institutes and through technology transfer.

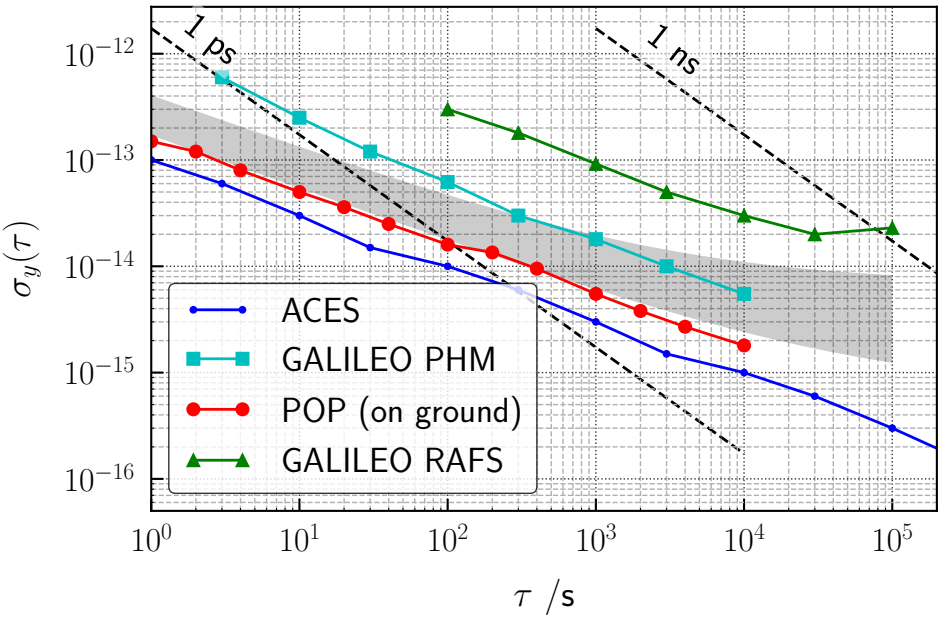

Figure 5.1: Typical stability of atomic clocks in European space programs (as taken from [172]) compared to the best achieved stability of the POP clock (on ground). The grey-shaded area represent the scissor between goal and threshold specifications for the space-qualified prototype. As a reference the frequency stability needed for obtaining 1 ps and 1 ns timing stability are indicated as dashed line.

The development of a space-qualified clock based on rubidium atoms and laser-pumping fits extremely well in this framework. The demonstration of the technological readiness of such a device would enlarge the ESA on-board clocks portfolio, and increase the level of independence of the agency from external suppliers. In fact, the clocks currently on-board of European GNSS satellites are either lamp-based rubidium clocks or passive hydrogen masers. The first ones are compact and low power consumption, while the second ones ensure very good stability performance, but they are heavy and costly. A space-qualified POP clock would fill the gap between the two, increasing technology diversity. This is evident if we look at table 5.1 where the main characteristics of RAFS and passive hydrogen maser currently on-board on GALILEO satellites are compared to the goal design specifications of Leonardo's clock under development. Concerning power consumption, size and mass, the POP clock stands between the other two technologies.

As a further comparison, in Fig. 5.1 the stability of the previously mentioned clock architectures are compared to the stability achieved with the POP clock (on a laboratory prototype on ground) and with the expected performances of ACES/PHARAO, a clock ensemble (composed of a hydrogen maser and a cesium

beam clock) under development for the International Space Station and that is going to provide a reference system for scientific works [173].

Table 5.1: Comparison between GALILEO on-board clocks and the POP clock under development. PHM stands for "passive hydrogen maser".

	Rb-POP		**PHM**	**RAFS**
	goal	**threshold**		
$\sigma_y(1\,\mathrm{s})$	2×10^{-13}	4×10^{-13}	2×10^{-12}	5×10^{-12}
$\sigma_y(1 \times 10^5\,\mathrm{s})$	2×10^{-15}	1×10^{-14}	7×10^{-15}	5×10^{-14}
Frequency drift $/\mathrm{d}^{-1}$	3×10^{-15}	1×10^{-14}	1×10^{-14}	1×10^{-12}
Thermal sensitivity $/\mathrm{K}^{-1}$	1×10^{-15}	3×10^{-15}	2×10^{-14}	3×10^{-14}
Magnetic sensitivity $/\mathrm{mT}^{-1}$	3×10^{-12}	5×10^{-12}	8×10^{-12}	5×10^{-13}
size (LxWxH)/(cm × cm × cm)	$35 \times 24 \times 20$		$53 \times 21 \times 25$	$21 \times 12 \times 12$
Envelope volume $/\mathrm{dm}^3$	17		28	3
Power consumption /W	40		70	25

5.2 Project status

The project starting in 2017 has seen the completion of the preliminary and final design review of the physics package unit. The design phase was supported by a few feasibility tests on a microwave-cavity testbed. The mechanical, thermal and electromagnetic analysis were driven by the target frequency stability, close to the one obtained with the POP frequency standard developed at INRiM (see table 5.1). At the same time, the units need to be compliant with the requirements of the GALILEO space program. In particular, considering the mechanical constraints, the unit must survive sustained vibrations and shocks during the rocket launch. The thermal model of the package aims at reaching temperature stability at cell

location of 100 µK on the relevant timescales, with operating conditions in the range −5 °C to 10 °C and a foreseen stability of the anchoring baseplate of ±2 K.

In parallel to the design phase, a cell filling facility was set up at Leonardo's headquarter (Nerviano, Milan), with the final goal of producing the spectroscopic cells to be employed in the clock setup. The facility design and procedures know-how were acquired also thanks to technology transfer from Marwan S.p.A. (Pisa, Italy). The first filling trials were performed in December 2018 using Ar-N_2 as buffer gas mixture and isotopically enriched ^{87}Rb. The cells were tested by visual inspection and through optical and double-resonance laser spectroscopy.

Figure 5.2: Picture of the realized engineering model EM1. Dimensions 35 cm × 24 cm × 20 cm. Total mass ≃ 3 kg. Courtesy of Leonardo S.p.A.

Following the design phase, in 2019 the first two engineering models, named EM1 and EM2, were produced (see Fig. 5.2). The empty cells were procured from an external supplier. The first prototype was assembled using a cell filled by Marwan S.p.A, while the second prototype with a cell filled at the newly established Leonardo facility. The other difference between the two prototypes is the thickness of the most external magnetic shield (0.5 mm and 1 mm respectively). Apart from these two aspects, the two units are nominally identical.

Shortly after the completion of the design review, the "test readiness review" has been completed. In the latter, the evaluation tests to be performed on the first two prototypes were agreed with ESA and Leonardo S.p.A. was appointed to execute them, following detailed guidelines. In the next sections, we will recap the results of the mechanical tests performed on the EM1 prototype. Moreover, an evaluation of the short-term capability of the two prototypes is presented, together

with an evaluation of the magnetic sensitivity of the EM1 unit.

5.3 Mechanical tests results

To validate the mechanical design, vibrations and shock tests were planned and performed on the EM1 prototype. The expected acceleration that the physics package can experience in a GALILEO mission includes steady-state loads as well as low and high-frequency loads during the rocket launch. From the program history and Leonardo's heritage in the development of passive hydrogen masers for GALILEO, a maximum value of $550\,\mathrm{m\,s^{-2}}$ is expected, assuming a total mass of 3 kg for the package. Another goal of the vibration test was to assess the first natural frequency of the structure (physics package and anchoring support). In fact, one of the design requirements of the structure was to have the first natural resonance above 140 Hz. The main qualification coming from the test is the capability of the structure to tolerate a certain amount of vibration without modifications of the clock performances. The most critical elements are the glass cell and the microwave coupling. Both elements must not undergo ruptures or modifications that can affect (or even prevent) the clock operation.

To this end, a sinusoidal vibration and a random vibration test were carried out in between two clock measurements. The sinusoidal vibration test included a low-amplitude sweep from 20 to 2000 Hz in order to find the mechanical resonance modes. The first natural resonance of the structure was recognized to lie at 450 Hz. The vibration test was performed applying a peak displacement of 10 mm in the range 5 Hz to 22 Hz and a peak acceleration of $200\,\mathrm{m\,s^{-2}}$ in the range 22 Hz to 100 Hz. The sweep rate was 2 oct/min, and one sweep was performed for each spatial direction.

The random vibration tests were arranged so as to apply different acceleration loads in the out-of-plane and in the in-plane directions. Concerning the out-of-plane vibration, an acceleration PSD of $54\,\mathrm{m\,s^{-2}\,Hz^{-1}}$ in the frequency range 100 Hz to 300 Hz was applied, decreasing by +3 dB/oct and by −5 dB/oct for lower and higher frequencies respectively. For the in-plane direction, the vibration levels were reduced to $22.5\,\mathrm{m\,s^{-2}\,Hz^{-1}}$ in the frequency range 100 Hz to 300 Hz, with the same scaling at higher and lower frequencies. The total duration of the test was 150 s on each axis.

For what concerns the shock test, the accelerations are defined in terms of "shock response spectrum levels" (the acceleration felt by an ideal system with only one degree of freedom at its own resonance frequency). The shock response spectrum levels devised for the test were: $500\,\mathrm{m\,s^{-2}}$ at 100 Hz, raising to $1 \times 10^4\,\mathrm{m\,s^{-2}}$ at 2000 Hz and at 10 000 Hz.

Both the vibrations and the shock tests were successfully passed by the EM1 unit. The survival of the unit to the vibrations and shocks was determined by

performing optical spectroscopy of the clock cell and determining the microwave cavity resonance center and quality factor prior and after the two tests. Both measurements showed no appreciable change in the results. Moreover, the test was ruled out as successful by integrating the EM1 physics package into INRiM clock setup and replicating the short-term clock stability performances reported in section 5.4.1 after the two tests.

5.4 Physics package performance tests

The engineering models EM1 and EM2 have been evaluated by integrating the physics package with the existing laser and electronic units at INRiM (see Fig. 2.1). The electronics and laser systems are the ones described in detail in chapter 2. The packages are operated in air, even though designed to be operated in vacuum for optimal performances. Thus, only the short-term properties of the systems are assessed at this stage.

For the performance test, the EM1 packages is heated with foil-heaters placed on the cavity and inner thermal shields. The cavity is slowly heated up to 67.5 °C while measuring the clock frequency and a buffer-gas inversion point close to 65 °C is addressed. From the pressure shift measured at the inversion point (+6000(50) Hz), the total buffer gas pressure is estimated to be 34(1) torr (45(2) hPa). At an operational temperature of 65 °C, a contrast of 38 % is obtained for the central Ramsey fringe with the following parameters: laser pump power 10 mW, detection power 850 µW, pump pulse duration 0.4 ms, detection pulse length 0.15 ms, $t_1 = 0.4$ ms, $T = 3$ ms (see Fig. 5.3). The laser beam is expanded and collimated at the physics package location with a beam size of 8 mm ($1/e^2$ waist). The laser frequency is stabilized on the $|F = 2\rangle$ line with an external reference cell, through saturation spectroscopy. For best performance, the frequency of the clock branch is tuned to the minimum of the broad clock absorption profile.

The EM2 package is operated in the same conditions as in the previous test. For the cell embedded in this unit, the absolute shift due to buffer gas collisions is +4390(50) Hz, thus the total buffer gas pressure is 25(1) torr (33(1) hPa). With the same operational parameters and clock timings as in the EM1 case, we obtain a fringe contrast of 47 %. The higher contrast is probably accountable for the lower buffer gas content and consequent lower decoherence rate.

5.4.1 Short-term evaluation

With these experimental conditions, the frequency stability of the two devices was measured using a hydrogen maser as a reference. The results are shown in Fig. 5.4. The fractional frequency stability is $1.8 \times 10^{-13}\ \tau^{-1/2}$, for both packages, for averaging times up to few tens of seconds. For longer averaging time, thermal

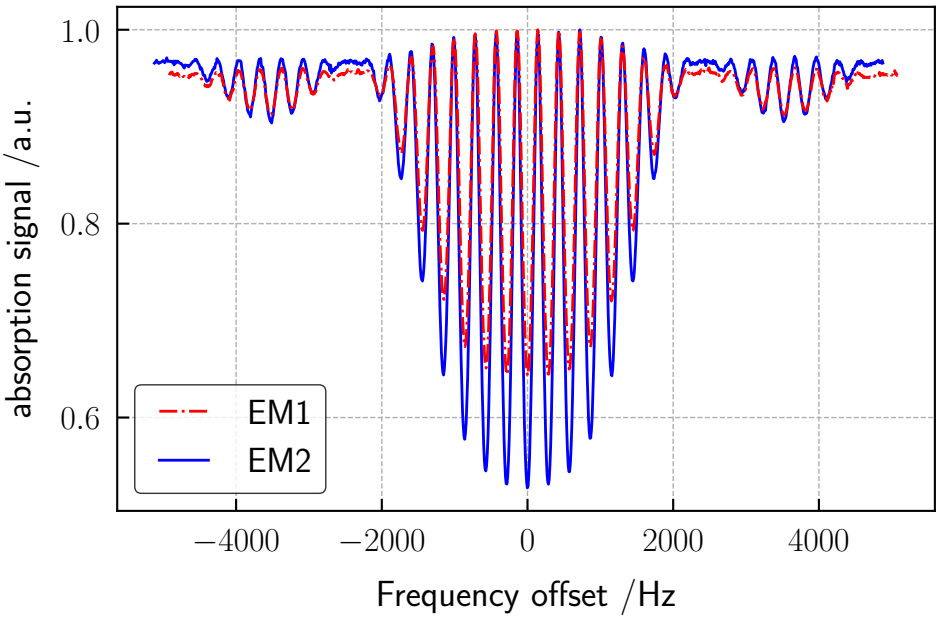

Figure 5.3: Ramsey fringes obtained with the engeneered physics packages (EM1 and EM2) at 64.5 °C. Single scan.

instabilities at the cavity and stem location and other environmental sources start to limit the medium-term stability. The short-term stability value is very close to the state of the art, and well within the target specifications ($\sigma_y(\tau) < 4 \times 10^{-13}\ \tau^{-1/2}$). On the other side, the high fringe contrast value is indicative of good cavity mode uniformity.

5.4.2 Magnetic field sensitivity

The effect of external magnetic fields on the clock transition is due to second-order Zeeman effect. The clock frequency is shifted in presence of a magnetic field $\vec{B}$ by the quantity:

$$\nu_Z = K_0 \left| \vec{B} \cdot \hat{z} \right|^2 \tag{5.1}$$

In the case of ^{87}Rb, $K_0 = 575.14 \times 10^8\,\mathrm{Hz\,T^{-2}}$. The clock is operated with a small bias magnetic field $\vec{B_0}$ directed along the z-axis, generated with a solenoid. Accordingly, the sensitivity is usually calculated considering the effect of small fields adding to the bias one, causing a variation ΔB_0 of the nominal value. We can, therefore, define the clock frequency variation corresponding to a small perturbation of the bias field magnitude:

$$\Delta\nu_0 = 2K_0 B_0\, \Delta B_0 \tag{5.2}$$

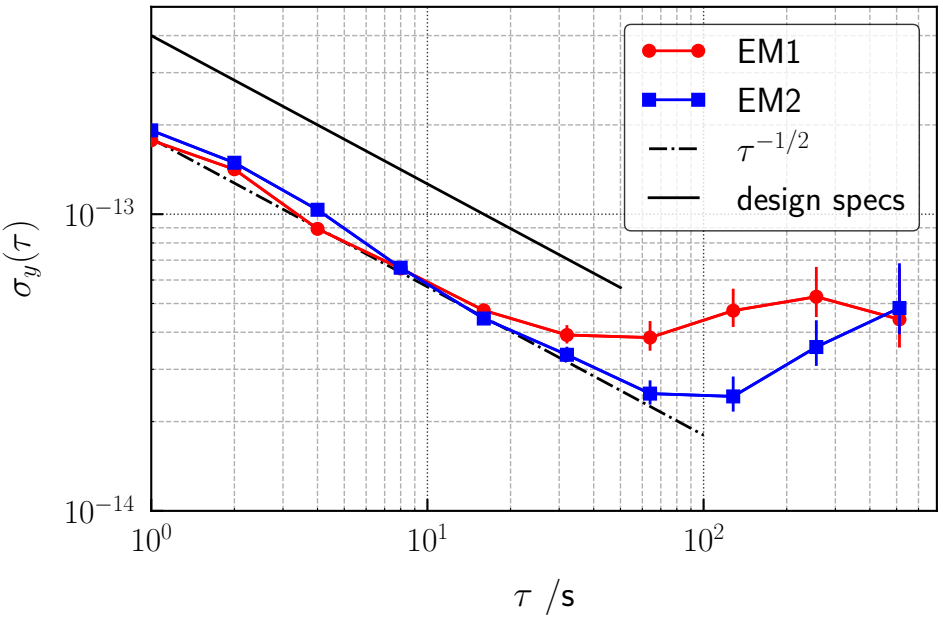

Figure 5.4: Short-term stability obtained with engineered physics packages and INRiM optics and electronics.

Such a variation can come from fluctuations of the current flowing in the solenoid or thermal noise from the mu-metal shield. These contributions can be constrained to negligible values by proper design [127]. Here we consider the effect of an externally applied magnetic field. The satellite environment is subject to varying magnetic fields. In particular the presence of magnetorquer to control and stabilize the satellite attitude induces a varying field inside the spacecraft as large as $1 \times 10^{-2}\,\mathrm{mT}$.

An external field is attenuated by the layers of magnetic shielding, and the residual field at atoms location $B_i\hat{n}$ adds to the bias one. We can thus calculate the device sensitivity to a variation of the external magnetic field $\Delta B_e\hat{n}$ by including the shielding factor $\eta = |B_e|/|B_i|$:

$$\frac{\Delta\nu_0}{\Delta B_e} = 2K_0B_0(\hat{n}\cdot\hat{z})\frac{\Delta B_i}{\Delta B_e} = 2K_0B_0(\hat{n}\cdot\hat{z})\frac{1}{\eta} \tag{5.3}$$

Given the cylindrical geometry of the shields, the attenuation coefficient η will be different for the radial and the axial directions. In particular, it is weaker for the axial one [174].

The experimental validation of the device magnetic sensitivity is performed by applying a known magnetic field generated by a pair of coils in a quasi-Helmholtz configuration. The coils are placed to generate a field directed into the longitudinal

direction (z-axis), where we expect the maximum sensitivity. The coils average radius is 20 cm and the separation between the two coils is 73.5 cm. With this geometrical configuration, the generated magnetic field has 0.1 mT magnitude at cell location, with an electric current of 0.8 A. The magnitude of the field shows less than 20 % variations from the value measured at the center of the system across all the volume of the physics package. The sign of the field can be changed by switching the sign of the current flowing in the coils.

To increase the sensitivity of the measurement, we run the device by locking the local oscillator on the $|F = 1; m_F = 1\rangle \rightarrow |F = 2; m_F = 1\rangle$ transition. In this case the clock frequency is linearly dependent on the magnetic field amplitude variation, with a sensitivity coefficient $K_1 = 14\,\mathrm{MHz\,mT^{-1}}$[50]. In Fig. 5.5 the fractional

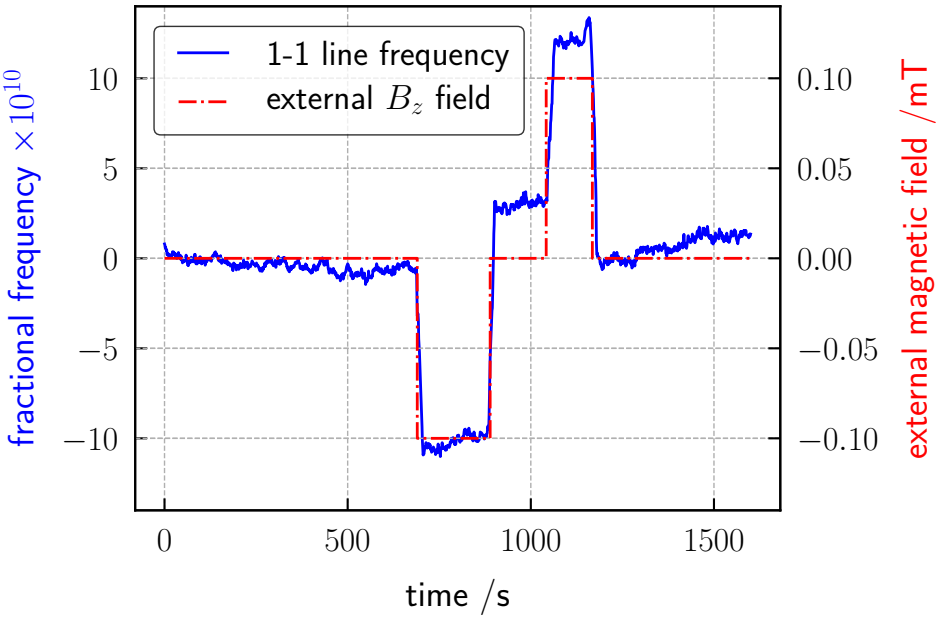

Figure 5.5: Magnetic field shielding measurement.

frequency variations of the 1-1 magnetic line are reported in a time sequence where the external magnetic field was alternatively set to ±0.1 mT. A well recognizable frequency shift is observed when the perturbing field is turned on. We can notice an asymmetry in the frequency shift when we switch the sign of the external field. This can be attributed to hysteresis in the behavior of the shields. Consequently, we can extract a conservative estimate of the attenuation factor, by considering only the biggest frequency jump. Dividing the frequency step by the known sensitivity of the magnetic line, we can estimate the magnitude of the magnetic field at atoms

location and finally get the axial shielding factor η_z:

$$\eta_z = \frac{\vec{B}_e \cdot \hat{z}}{\vec{B}_i \cdot \hat{z}} = 150\,000 \pm 20\,000$$

This value is compliant with the design specifications, which required a lower threshold $\eta > 1 \times 10^4$, and with the design goal $\eta > 1 \times 10^5$. The feasibility of a shielding factor $> 1 \times 10^5$ was supported by FEM simulations which considered also the effects of the shields caps and holes, but nevertheless its experimental verification is an important step in the design validation. Significantly, the shielding factor has been measured twice, before and after the shock test. No appreciable change in the shielding effectiveness was observed. This means that the shields are rather robust against magnetization from strong vibrations.

From the estimated η_z and for an operative bias field $B_0 = 1.5\,\mu\text{T}$, from (5.3) we can infer the clock sensitivity to external magnetic fields to be below $2 \times 10^{-13}/\text{mT}$. This value is one order of magnitude below the threshold specification (see table 5.1).

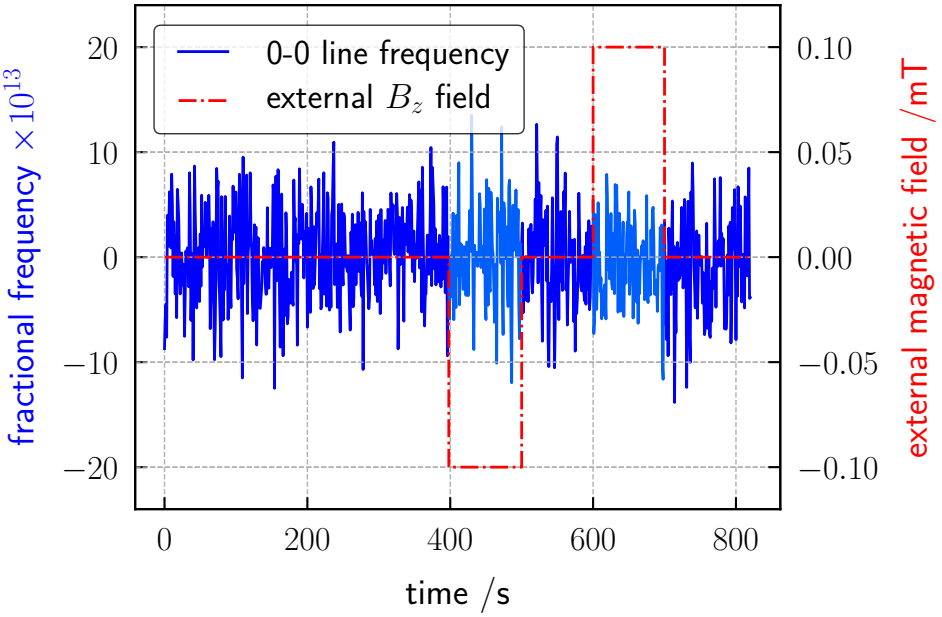

Figure 5.6: Magnetic field sensitivity measurement on the clock transition.

The magnetic sensitivity has been confirmed by operating the clock in the nominal condition, i.e. stabilizing the LO on the 0-0 transition. Even though we expect the frequency shift on the atomic line to be smaller than the clock frequency noise at this stage, we can make sure that no other parts (such as the detection electronics) cause additional sensitivity to the measured clock frequency. Also in this case,

$\pm 0.1\,\mathrm{mT}$ along the longitudinal direction were applied. The clock measurement is shown in Fig. 5.6. As expected, no net shift is observed on the clock transition above the noise level.

5.4.3 Arrangements for a thermo-vacuum test

The medium-long term properties of the physics package will be tested in vacuum environment. To simulate the operational conditions on board of the spacecraft, the package will be placed on top of a temperature-regulated baseplate. The plate is made of brass and contains a U-shaped copper tube in which a refrigerating (or heating) fluid can flow. The baseplate inner circuit is connected to an ISO-KF feedthrough by means of vacuum-proof steel tubing to exit the vacuum chamber. An external recirculating liquid chiller will pump and thermally regulate the coolant fluid. In Fig. 5.7a the whole vacuum chamber is shown. In the picture, we can notice the feedthroughs for the coolant liquid, an optical window for the laser beam delivery and an RF feedthrough for microwave delivery. We can also notice the coils used in the magnetic-shielding test previously described in section 5.4.2. In Fig. 5.7b the baseplate connected to the tubing for liquid circulation is shown. To

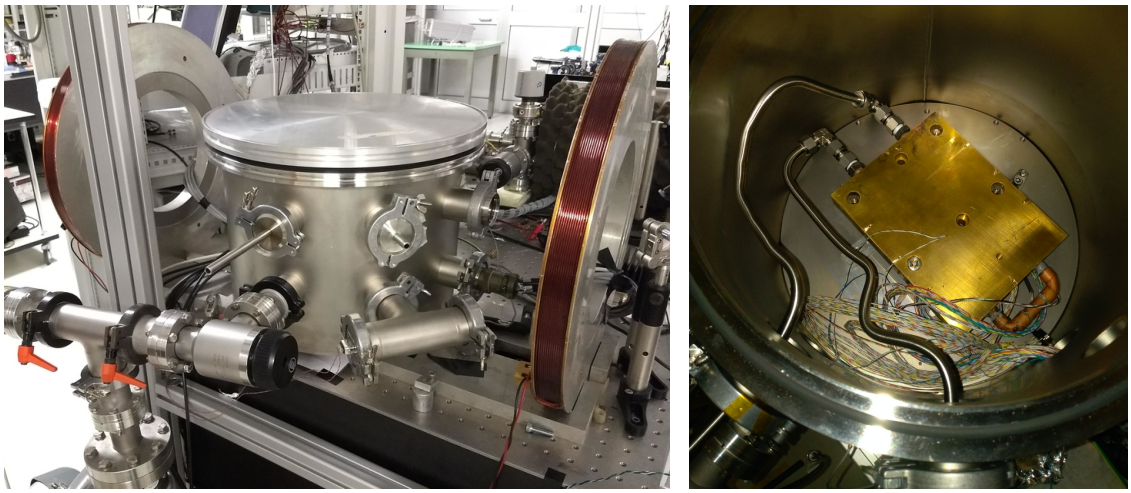

(a) Vacuum system. (b) Thermally-regulated baseplate.

Figure 5.7: Vacuum chamber and thermally-regulated baseplate to perform thermo-vacuum tests.

verify the damping factor of the thermal controls, a thermo-vacuum test has been devised. While the clock is running, the baseplate temperature will be changed with slow ramps with a maximum excursion of 40 K (from a minimum of $-17\,^{\circ}\mathrm{C}$ to a maximum of $22\,^{\circ}\mathrm{C}$). Clock stability and temperature stability at the cavity and stem location will be monitored for the full run. A typical temperature profile that will be employed during the test is shown in Fig. 5.8. To reach temperatures below

the water freezing point a mixture of water and propylene glycol with equal parts will be used. The vacuum chamber has been proven to sustain a vacuum pressure

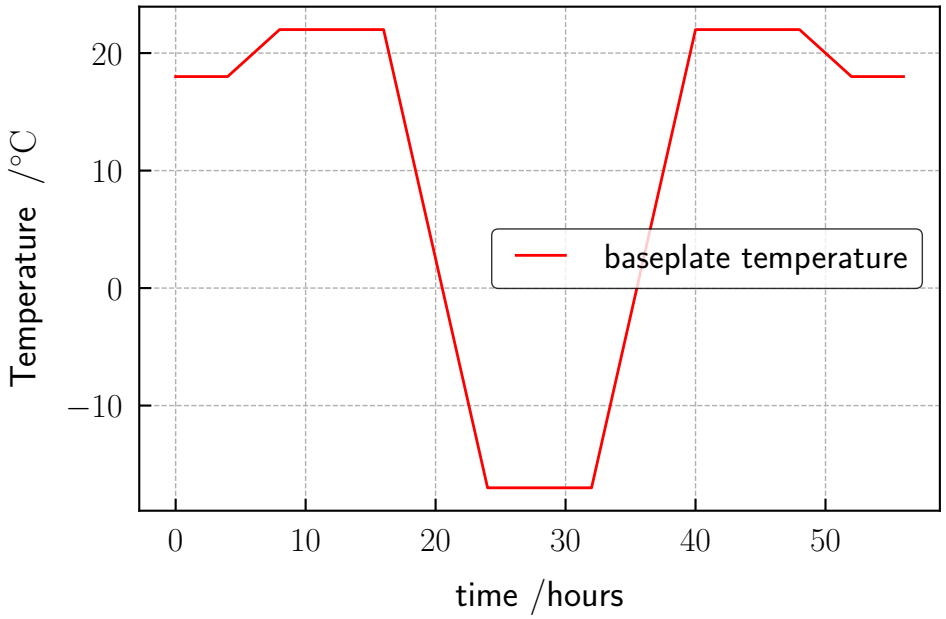

Figure 5.8: Typical thermal ramp induced on the physics package baseplate during the foreseen thermo-vacuum tests.

of 1×10^{-5} mbar at ambient temperature and the vacuum capability is currently under test with circulating liquid in the full range of operational temperatures for the baseplate.

Chapter 6

Conclusions and project perspectives

In this manuscript, I reported some studies on a high-performing POP microwave clock. The short-term behavior of the frequency standard has been further characterized and novel locking techniques have been proposed to simplify the clock implementation. Moreover, a compact design based on a loaded microwave cavity has been developed and tested. The proposed techniques and the novel design contribute to the readiness of the POP technology for practical applications outside the laboratory and for spaceborne applications. Finally, the thesis reports on a few experimental tests performed on the engineered physics packages developed by Leonardo S.p.A. and on the project status towards the realization of a space-qualified POP clock. In the following, the main results obtained during the PhD program are resumed and put in the context of future improvements and outlooks.

POP short-term characterization. Regarding the clock characterization, the major known contributions to the short-term of pulsed optically pumped devices have been resumed in an comprehensive way. Moreover, a signal-theory model has been introduced to calculate the AM-AM contribution coming from laser intensity noise. The proposed model is extremely general, as it does not depend on the physical properties of the atomic sample. Indeed, the atomic medium is considered as an ideal absorber. Thus, the model is valid (and tested) in the weak-probe approximation. The model can be used in the design phase for choosing the correct laser source to reach the target stability or during the characterization phase to distinguish between the various noise sources. The signal-theory approach has allowed us to underline how the noise conversion is basically an aliasing process, similar to the Dick effect. In this case, though, the Fourier frequencies of interest are the odd multiples of half the basic clock sequence ($f_k = kT_c/2$, with odd k).

The next step, to fully describe the noise conversion taking place in the POP

and similar vapor-cell devices is to extend the model, to consider also the effect of FM noise affecting the laser source. The conversion of the FM noise into the amplitude of the detected atomic signal (FM-AM conversion) is a non-linear process, thus its treatment must include a modification of the presented approach. Moreover, some physical parameters of the active medium must necessarily be included (such as density, temperature, length of the cell). If optical pumping effects are included, the extended model would account also for the AM-AM conversion for higher detection probe power.

Advanced locking techniques. The clock implementation has been enriched by novel schemes that enable the stabilization of some physical parameters of interest directly on the clock signal. In particular, the amplitude of the microwave synthesizer and the laser frequency can be stabilized by using double-loop algorithms, without resorting to external references. Notably, such techniques do not degrade the stability performances of the clock, thanks to the low sensitivity of the POP architecture to environmental parameters, that allows implementing low-bandwidth locking schemes.

The possibility to eliminate the external reference system to stabilize the laser frequency constitutes an important step towards the simplification and practical realization of a standard based on the POP technique. Concerning space application, it is also an added value, as the number of optical and electronic components would be reduced, saving volume, mass and power budget. If an external reference is preferred, the technique can be used to increase the system redundancy and resilience against possible failures.

The next steps for the characterization of the laser frequency stabilization techniques would be a more detailed analysis of the impact on the clock long-term stability. In particular, the technique based on resonant light-shift can possibly benefit from locking the laser on the point of "zero" light shift, in terms of sensitivity to laser power. Moreover, to improve the reliability of the proposed techniques, they must be routinely implemented and further standardized.

Compact cavity-cell assembly. Given the interest of the space sector into the POP technique, a strategy to reduce the overall size, weight and power consumption of the physics package unit has been pursued. The introduction of a loaded cavity design has led to a volume reduction of more than a factor 8 for the cavity-cell assembly, with promising scaling of the outer layers. The quality of the electromagnetic mode has been studied in detail with FEM simulations. The reduction in size, and in particular the use of a smaller spectroscopic cell, was demonstrated not to degrade the short-term performances significantly. Indeed, a short-term stability $\sigma_y(\tau) = 4.5 \times 10^{-13}\,\tau^{-1/2}$ was obtained with the compact setup.

Since long-term performance is the real challenge for practical applications of

the device, a smaller form factor can indeed facilitate thermal and magnetic field uniformity, with consequent benefit on the long-term behavior. Moreover, releasing the minimum requirements for the short-term, by accepting a higher decoherence rate from the walls collision and buffer gas interactions, has made appealing the investigation of an alternative Kr-N_2 mixture, which presents a much smaller barometric coefficient. In this case, a short-term stability as low as $5.2 \times 10^{-13}\,\tau^{-1/2}$ was demonstrated. Considering the future long-term characterization, this buffer-gas composition is advantageous in terms of sensitivity to temperature and pressure-related long-term instabilities. The lower sensitivity can be exploited either to relax the design specifications or to pursuit better long-term stability.

Steps towards a space-qualified clock. Finally, the first tests on an engineered physics package developed by Leonardo S.p.A. was a step towards the technology readiness of the POP clock architecture for space applications. The measurements on the two realized prototypes have demonstrated state-of-the-art short-term performances when integrated with INRiM optics and electronics. The mechanical (shock and vibration) tests agreed with ESA were successfully passed by one of the two units, further validating the design. Also, the magnetic shielding was proven to be in line with the specifications and resilient against mechanical vibrations and shocks. The next step is achieving good medium-long term performances by operating in vacuum and further characterizing the thermal sensitivity of the physics package by performing thermo-vacuum tests. The indications coming from the tests will serve as a basis for the activation of the second phase of the project, which foresees the engineering of the optics and electronics packages.

Appendix A

Alternative locking protocol - effect of laser AM noise

In this appendix, we analyze a locking scheme (adopted for example in [122]), alternative to the one described in section 2.1.4, and we describe its impact on the short-term stability due to laser AM noise. To analyze the noise conversion, we will use the same signal-theory tools introduced in section 2.2.1. For simplicity, we will call the protocol of chapter 2 "Protocol 1" and the one described below "Protocol 2".

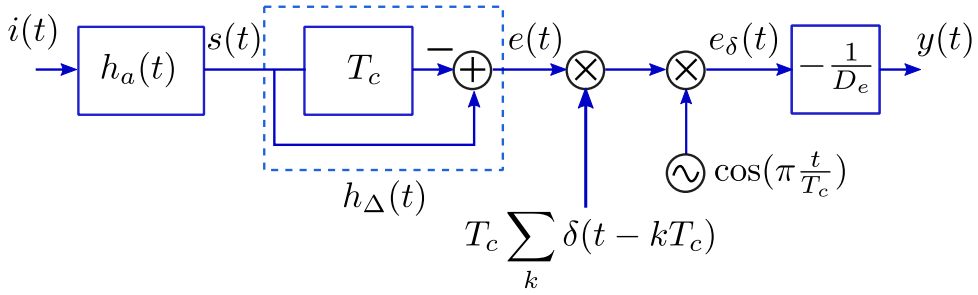

Figure A.1: Block scheme of the model of noise transfer to the clock stability in the time domain. The LO frequency correction is performed with rate $1/T_c$. This implies an additional demodulation term.

By using protocol 2, the error signal E is computed as:

$$E[kT_c] = (S[kT_c] - S[(k-1)T_c])(-1)^k \tag{A.1}$$

Here, S is the sampled atomic signal available after a basic clock sequence of duration T_c (pumping, Ramsey interrogation, optical detection). In the notation, we have dropped the LO frequency modulation, which is performed as usual with a

square wave of period $2T_c$, to probe the two sides of the resonance. The error signal is available with rate $1/T_c$ and the correction to the LO frequency can be applied with the same rate. The $(-1)^k$ factor is needed to perform a correct demodulation of the signal (i.e. preserving always the same slope sign of the error signal as a function of the LO detuning).

The block scheme describing the protocol in time domain is shown in Fig. A.1. As in Protocol 1, $i(t)$ are the relative fluctuations of the laser intensity, which are transferred to the relative fluctuations of the detected signal $s(t)$ and of the sampled error signal $e_\delta(t)$. To simplify the calculation, the demodulation term $(-1)^k$ is substituted with a sinusoidal modulation $\cos(\pi t/T_c)$. The net result is the same, since in the block scheme this term is preceded by the signal sampling.

By switching to frequency domain, we find the following expression, linking the PSD of the error signal to the relative intensity noise of the detection laser:

$$S_{e_\delta}(f) \simeq 2[1+\cos(2\pi f T_c)] \sum_{k \text{ odd}} \left| H_a\left(\frac{k}{2T_c}\right)\right|^2 S_i\left(\frac{k}{2T_c}\right) \tag{A.2}$$

For averaging times $\tau \gg \tau_L$ (where τ_L is the time constant of the frequency loop), i.e. for $f \to 0$, the error signal noise level is the same as in the protocol of section 2.2.1. Despite the fact that the error signal and the correction are available with twice the rate, the effect on the clock stability is essentially the same (for commonly encountered laser noise types). This is a not obvious conclusion, which is rigorously treated by the signal-theory model.

Some different behavior is expected between the two protocols if some spurs are present in the noise spectrum. For Protocol 1, spurs at odd multiples of the sampling rate $1/(2T_c)$, lying within the bandwidth of the filter $H(f)$, are indeed directly translated into baseband and can affect the short-term stability. In protocol 2, the spurs are possibly attenuated thanks to the multiplicative factor $1+\cos(2\pi f T_c)$. Moreover, the frequencies of interest are odd multiples of $1/T_c$. Therefore, concerning the spurs, the two protocols behave differently.

Bibliography

[1] R. T. Dupuis, T. J. Lynch, and J. R. Vaccaro. "Rubidium Frequency Standard for the GPS IIF program and modifications for the RAFSMOD Program". In: *2008 IEEE International Frequency Control Symposium*. IEEE, May 2008. DOI: 10.1109/freq.2008.4623081 (cit. on pp. 1, 9).

[2] P. Waller, F. Gonzalez, S. Binda, I. Sesia, I. Hidalgo, G. Tobias, and P. Tavella. "The In-Orbit performances of GIOVE clocks". In: *IEEE Transactions on Ultrasonics, Ferroelectrics and Frequency Control* 57.3 (Mar. 2010), pp. 738–745. DOI: 10.1109/tuffc.2010.1472 (cit. on p. 1).

[3] S. Revnivykh. "GLONASS status and modernization". In: *International GNSS Committee IGC-7 Beijing* (2012), pp. 4–9. URL: http://www.unoosa.org/pdf/icg/2012/icg-7/3-1.pdf (cit. on p. 1).

[4] H. Chunhao, C. Zhiwu, L. Yuting, L. Li, X. Shenghong, Z. Lingfeng, and W. Xianglei. "Time Synchronization and Performance of BeiDou Satellite Clocks in Orbit". In: *International Journal of Navigation and Observation* 2013 (2013), pp. 1–5. DOI: 10.1155/2013/371450 (cit. on p. 1).

[5] D. Fabien, R. Pascal, B. Sebastien, and S. Batiste. "GNSS RAFS latest improvements". In: *2015 Joint Conference of the IEEE International Frequency Control Symposium & the European Frequency and Time Forum*. IEEE, Apr. 2015. DOI: 10.1109/fcs.2015.7138926 (cit. on pp. 1, 5).

[6] C. L. Thornton and J. S. Border. *Radiometric tracking techniques for deep-space navigation*. John Wiley & Sons, 2003 (cit. on p. 1).

[7] J. D. Prestage and G. L. Weaver. "Atomic Clocks and Oscillators for Deep-Space Navigation and Radio Science". In: *Proceedings of the IEEE* 95.11 (Nov. 2007), pp. 2235–2247. DOI: 10.1109/JPROC.2007.905130 (cit. on p. 1).

[8] T. A. Ely, E. A. Burt, J. D. Prestage, J. M. Seubert, and R. L. Tjoelker. "Using the Deep Space Atomic Clock for Navigation and Science". In: *IEEE Transactions on Ultrasonics, Ferroelectrics, and Frequency Control* 65.6 (June 2018), pp. 950–961. DOI: 10.1109/TUFFC.2018.2808269 (cit. on p. 1).

[9] M. A. Lombardi, A. N. Novick, G. Neville-Neil, and B. Cooke. "Accurate, Traceable, and Verifiable Time Synchronization for World Financial Markets". In: *Journal of Research of the National Institute of Standards and Technology* 121 (Oct. 2016), p. 436. DOI: 10.6028/jres.121.023 (cit. on p. 2).

[10] J. Coffed. "The threat of gps jamming: The risk to an information utility". In: *Report of EXELIS* (2014), pp. 6–10 (cit. on p. 2).

[11] W. J. Riley. "A rubidium clock for GPS." In: *Proc. of the 13th Ann. Precise Time and Time Interval (PTTI) Appl. and Planning Meeting*. 1982 (cit. on p. 2).

[12] Q. Hao, W. Li, S. He, J. Lv, P. Wang, and G. Mei. "A physics package for rubidium atomic frequency standard with a short-term stability of $2.4\times10^{-13}\,\tau^{-1/2}$". In: *Review of Scientific Instruments* 87.12 (Dec. 2016), p. 123111. DOI: 10.1063/1.4972567 (cit. on pp. 2, 9).

[13] J. C. Camparo and R. P. Frueholz. "Fundamental stability limits for the diode-laser-pumped rubidium atomic frequency standard". In: *Journal of Applied Physics* 59.10 (May 1986), pp. 3313–3317. DOI: 10.1063/1.336847 (cit. on p. 2).

[14] T. Bandi, C. Affolderbach, C. Stefanucci, F. Merli, A. K. Skrivervik, and G. Mileti. "Compact high-performance continuous-wave double-resonance rubidium standard with $1.4 \times 10^{-13}\ \tau^{-1/2}$ stability". In: *IEEE Transactions on Ultrasonics, Ferroelectrics, and Frequency Control* 61.11 (Nov. 2014), pp. 1769–1778. DOI: 10.1109/TUFFC.2013.005955 (cit. on pp. 2, 12, 13, 17, 46).

[15] P. Yun, F. Tricot, C. E. Calosso, S. Micalizio, B. François, R. Boudot, S. Guérandel, and E. de Clercq. "High-Performance Coherent Population Trapping Clock with Polarization Modulation". In: *Physical Review Applied* 7.1 (Jan. 2017). DOI: 10.1103/physrevapplied.7.014018 (cit. on pp. 2, 16).

[16] M. A. Hafiz and R. Boudot. "A coherent population trapping Cs vapor cell atomic clock based on push-pull optical pumping". In: *Journal of Applied Physics* 118.12 (Sept. 2015), p. 124903. DOI: 10.1063/1.4931768 (cit. on pp. 2, 15–17).

[17] S. Knappe, P. D. D. Schwindt, V. Shah, L. Hollberg, J. Kitching, L. Liew, and J. Moreland. "A chip-scale atomic clock based on ^{87}Rb with improved frequency stability". In: *Optics Express* 13.4 (2005), p. 1249. DOI: 10.1364/opex.13.001249 (cit. on p. 2).

[18] J. Kitching. "Chip-scale atomic devices". In: *Applied Physics Reviews* 5.3 (Sept. 2018), p. 031302. DOI: 10.1063/1.5026238 (cit. on p. 2).

[19] Y. Zhang, W. Yang, S. Zhang, and J. Zhao. "Rubidium chip-scale atomic clock with improved long-term stability through light intensity optimization and compensation for laser frequency detuning". In: *Journal of the Optical Society of America B* 33.8 (July 2016), p. 1756. DOI: 10.1364/josab.33.001756 (cit. on p. 2).

[20] P. Cash, W. Krzewick, P. Machado, K. R. Overstreet, M. Silveira, M. Stanczyk, D. Taylor, and X. Zhang. "Microsemi Chip Scale Atomic Clock (CSAC) technical status, applications, and future plans". In: *2018 European Frequency and Time Forum (EFTF)*. IEEE, Apr. 2018. DOI: 10.1109/eftf.2018.8408999 (cit. on p. 2).

[21] C. Gorecki. "Development of First European Chip-scale Atomic Clocks: Technologies, Assembling and Metrology". In: *Procedia Engineering* 47 (2012), pp. 898–903. DOI: 10.1016/j.proeng.2012.09.292 (cit. on p. 2).

[22] S. Prazot et al. "The medium and long term stability of the NAC atomic clock". In: *2017 Joint Conference of the European Frequency and Time Forum and IEEE International Frequency Control Symposium (EFTF/IFC)*. IEEE, 2017. DOI: 10.1109/fcs.2017.8088834 (cit. on p. 2).

[23] P. Knapkiewicz. "Technological Assessment of MEMS Alkali Vapor Cells for Atomic References". In: *Micromachines* 10.1 (Dec. 2018), p. 25. DOI: 10.3390/mi10010025 (cit. on p. 2).

[24] C. Gorecki, N. Passilly, V. Maurice, S. Bargiel, R. Chutani, R. Boudot, R. Vicarini, and S. Galliou. "Advanced microfabrication technologies for miniature caesium vapor cells for atomic clocks". In: *Optical, Opto-Atomic, and Entanglement-Enhanced Precision Metrology*. Ed. by S. M. Shahriar and J. Scheuer. SPIE, Mar. 2019. DOI: 10.1117/12.2506225 (cit. on p. 2).

[25] S. Karlen, T. Overstolz, J. Gobet, J. Haesler, F. Droz, and S. Lecomte. "Gold microdiscs as alkali preferential condensation spots for cell clock long-term frequency improvement". In: *2018 European Frequency and Time Forum (EFTF)*. IEEE, Apr. 2018. DOI: 10.1109/eftf.2018.8409005 (cit. on p. 2).

[26] S. Abdullah, C. Affolderbach, F. Gruet, and G. Mileti. "Aging studies on micro-fabricated alkali buffer-gas cells for miniature atomic clocks". In: *Applied Physics Letters* 106.16 (Apr. 2015), p. 163505. DOI: 10.1063/1.4919009 (cit. on p. 2).

[27] J. Kitching et al. "Chip-scale atomic clocks at NIST". In: *NCSL International Workshop and Symposium*. 2005 (cit. on p. 2).

[28] D. Lutwak R. anc Emmons, W. Riley, and R. M. Garvey. *The Chip-Scale Atomic Clock - Coherent Population Trapping vs. Conventional Interrogation*. Tech. rep. Symmetricom-Tecnology Realization Center Beverly MA, 2003 (cit. on p. 2).

[29] M. A. Hafiz, G. Coget, P. Yun, S. Guérandel, E. de Clercq, and R. Boudot. "A high-performance Raman-Ramsey Cs vapor cell atomic clock". In: *Journal of Applied Physics* 121.10 (2017), p. 104903. DOI: 10.1063/1.4977955 (cit. on pp. 3, 16, 17).

[30] S. Micalizio, A. Godone, C. Calosso, F. Levi, C. Affolderbach, and F. Gruet. "Pulsed optically pumped rubidium clock with high frequency-stability performance". In: *IEEE Transactions on Ultrasonics, Ferroelectrics, and Frequency Control* 59.3 (Mar. 2012), pp. 457–462. DOI: 10.1109/TUFFC.2012.2215 (cit. on p. 3).

[31] M. A. Hafiz, G. Coget, M. Petersen, C. E. Calosso, S. Guérandel, E. de Clercq, and R. Boudot. "Symmetric autobalanced Ramsey interrogation for high-performance coherent-population-trapping vapor-cell atomic clock". In: *Applied Physics Letters* 112.24 (June 2018), p. 244102. DOI: 10.1063/1.5030009 (cit. on pp. 3, 16, 17, 41).

[32] S. Micalizio, C. E. Calosso, A. Godone, and F. Levi. "Metrological characterization of the pulsed Rb clock with optical detection". In: *Metrologia* 49.4 (2012), p. 425. URL: http://stacks.iop.org/0026-1394/49/i=4/a=425 (cit. on pp. 3, 17, 19, 42, 70).

[33] S. Kang, M. Gharavipour, C. Affolderbach, F. Gruet, and G. Mileti. "Demonstration of a high-performance pulsed optically pumped Rb clock based on a compact magnetron-type microwave cavity". In: *Journal of Applied Physics* 117.10 (2015), p. 104510. DOI: 10.1063/1.4914493 (cit. on pp. 3, 63).

[34] D. Zhi-jing, Z. Shou-gang, L. Jie, L. Xiao-feng, L. Dan-dan, and X. Wen-xiang. "The pulsed optically pumped Rb frequency standards in National Time Service Center". In: *2012 IEEE International Frequency Control Symposium Proceedings*. IEEE, May 2012. DOI: 10.1109/fcs.2012.6243579 (cit. on p. 3).

[35] G. Dong, J. Deng, J. Lin, S. Zhang, H. Lin, and Y. Wang. "Recent improvements on the pulsed optically pumped rubidium clock at SIOM". In: *Chin. Opt. Lett.* 15.4 (Apr. 2017), p. 040201. URL: http://col.osa.org/abstract.cfm?URI=col-15-4-040201 (cit. on p. 3).

[36] V. Baryshev, D. Kupalov, A. Novoselov, M. Aleinikov, A. Boiko, V. Pal'chikov, and I. Y. Blinov. "Compact Quantum Frequency Standard Using A Rubidium Vapor Cell With Pulsed Optical Pumping and Microwave Excitation Using the Ramsey Scheme". In: *Measurement Techniques* 59.12 (2017), pp. 1286–1290 (cit. on p. 3).

[37] J. C. Camparo, T. U. Driskell, and A. F. S. Command. "The mercury-ion clock and the pulsed-laser rubidium clock: Near-term candidates for future GPS deployment". In: *Aerospace Report No. TOR-2015-03893, 5 October 2015. The Aerospace Corporation: El Segundo, CA* (2015) (cit. on p. 3).

[38] R. L. Tjoelker et al. "Mercury Ion Clock for a NASA Technology Demonstration Mission". In: *IEEE Transactions on Ultrasonics, Ferroelectrics, and Frequency Control* 63.7 (July 2016), pp. 1034–1043. DOI: 10.1109/TUFFC.2016.2543738 (cit. on p. 3).

[39] M. Arditi. "A Gas Cell" Atomic Clock" as a High-Stability Frequency Standard". In: *IRE Transactions on Military Electronics* 1 (1960), pp. 25–28 (cit. on p. 4).

[40] R. Carpenter, E. Beaty, P. Bender, S. Saito, and R. Stone. "A prototype rubidium vapor frequency standard". In: *IRE Trans. Instrum.* 1 (1960), pp. 132–135 (cit. on pp. 4, 9).

[41] M. E. Packard and B. E. Swartz. "The Optically Pumped Rubidium Vapor Frequency Standard". In: *IRE Transactions on Instrumentation* I-11.3 (Dec. 1962), pp. 215–223. DOI: 10.1109/ire-i.1962.5006634 (cit. on p. 4).

[42] URL: https://www.orolia.com/products-services/atomic-clocks-oscillators/rafs (cit. on p. 4).

[43] URL: https://freqelec.com/wp-content/uploads/2019/03/4-RAFS-Brochure.pdf (cit. on p. 4).

[44] A. Kastler. "Quelques suggestions concernant la production optique et la détection optique d'une inégalité de population des niveaux de quantifigation spatiale des atomes. Application à l'expérience de Stern et Gerlach et à la résonance magnétique". In: *Journal de Physique et le Radium* 11.6 (1950), pp. 255–265. DOI: 10.1051/jphysrad:01950001106025500 (cit. on p. 4).

[45] H. G. Dehmelt. "Slow Spin Relaxation of Optically Polarized Sodium Atoms". In: *Physical Review* 105.5 (Mar. 1957), pp. 1487–1489. DOI: 10.1103/physrev.105.1487 (cit. on p. 4).

[46] R. H. Dicke. "The Effect of Collisions upon the Doppler Width of Spectral Lines". In: *Physical Review* 89.2 (Jan. 1953), pp. 472–473. DOI: 10.1103/physrev.89.472 (cit. on pp. 4, 8).

[47] T. Carver. "Rubidium Oscillator Experiments". In: *11th Annual Symposium on Frequency Control*. IEEE, 1957. DOI: 10.1109/freq.1957.199306 (cit. on p. 4).

[48] F. Vannicola, R. Beard, J. White, K. Senior, M. Largay, and J. Buisson. *GPS block IIF atomic frequency standard analysis*. Tech. rep. Naval Research Lab Washington DC, 2010 (cit. on pp. 5, 9).

[49] G. Mei et al. "Main features of space rubidium atomic frequency standard for BeiDou satellites". In: *2016 European Frequency and Time Forum (EFTF)*. IEEE, Apr. 2016. DOI: 10.1109/eftf.2016.7477803 (cit. on pp. 5, 9).

[50] J. Vanier and C. Audoin. *The Quantum Physics of Atomic Frequency Standards*. Vol. 2. Philadelphia: Adam Hilger, 1989 (cit. on pp. 8, 11, 13, 42, 75, 77, 83, 93, 113).

[51] J. P. Wittke and R. H. Dicke. "Redetermination of the Hyperfine Splitting in the Ground State of Atomic Hydrogen". In: *Physical Review* 103.3 (Aug. 1956), pp. 620–631. DOI: 10.1103/physrev.103.620 (cit. on p. 8).

[52] E. C. Beaty, P. L. Bender, and A. R. Chi. "Narrow Hyperfine Absorption Lines of Cs133 in Various Buffer Gases". In: *Physical Review* 112.2 (Oct. 1958), pp. 450–451. DOI: 10.1103/physrev.112.450 (cit. on p. 8).

[53] P. L. Bender, E. C. Beaty, and A. R. Chi. "Optical Detection of Narrow Rb87 Hyperfine Absorption Lines". In: *Physical Review Letters* 1.9 (Nov. 1958), pp. 311–313. DOI: 10.1103/physrevlett.1.311 (cit. on pp. 8, 75).

[54] M. Bloch, O. Mancini, and T. McClelland. "Performance of rubidium and quartz clocks in space". In: *Proceedings of the 2002 IEEE International Frequency Control Symposium and PDA Exhibition (Cat. No.02CH37234)*. IEEE. DOI: 10.1109/freq.2002.1075936 (cit. on p. 10).

[55] J. Camparo, C. Klimcak, and S. Herbulock. "Frequency Equilibration in the Vapor-Cell Atomic Clock". In: *IEEE Transactions on Instrumentation and Measurement* 54.5 (Oct. 2005), pp. 1873–1880. DOI: 10.1109/tim.2005.853217 (cit. on p. 10).

[56] J. Camparo. "Does the light shift drive frequency aging in the rubidium atomic clock?" In: *IEEE Transactions on Ultrasonics, Ferroelectrics and Frequency Control* 52.7 (July 2005), pp. 1075–1078. DOI: 10.1109/tuffc.2005.1503993 (cit. on p. 10).

[57] J. Camparo, V. Formichella, I. Sesia, G. Signorile, L. Galleani, and P. Tavella. "Characterization & consequences of GPS Rb clock lamplight variations". In: *2016 IEEE International Frequency Control Symposium (IFCS)*. IEEE, May 2016. DOI: 10.1109/fcs.2016.7546751 (cit. on p. 10).

[58] V. Formichella, J. Camparo, I. Sesia, G. Signorile, L. Galleani, M. Huang, and P. Tavella. "The ac stark shift and space-borne rubidium atomic clocks". In: *Journal of Applied Physics* 120.19 (Nov. 2016), p. 194501. DOI: 10.1063/1.4967787 (cit. on p. 10).

[59] M. Epstein, T. Dass, J. Rajan, and P. Gilmour. *Long-term clock behavior of GPS IIR satellites*. Tech. rep. ITT CORP CLIFTON NJ SPACE SYSTEMS DIV, 2007 (cit. on p. 10).

[60] R. Bazurto, M. Huang, and J. Camparo. "Spectral emission from the alkali inductively-coupled plasma: Theory and experiment". In: *AIP Advances* 8.4 (Apr. 2018), p. 045319. DOI: 10.1063/1.5018088 (cit. on p. 10).

[61] M. Langlois, L. D. Sarlo, D. Holleville, N. Dimarcq, J.-F. Schaff, and S. Bernon. "Compact Cold-Atom Clock for Onboard Timebase: Tests in Reduced Gravity". In: *Physical Review Applied* 10.6 (Dec. 2018). DOI: 10.1103/physrevapplied.10.064007 (cit. on p. 10).

[62] F. Esnault, N. Rossetto, D. Holleville, J. Delporte, and N. Dimarcq. "HORACE: A compact cold atom clock for Galileo ". In: *Advances in Space Research* 47.5 (2011). Scientific applications of Galileo and other Global Navigation Satellite Systems - {II}, pp. 854–858. DOI: http://dx.doi.org/10.1016/j.asr.2010.12.012 (cit. on p. 10).

[63] P. Liu, Y. Meng, J. Wan, X. Wang, Y. Wang, L. Xiao, H. Cheng, and L. Liu. "Scheme for a compact cold-atom clock based on diffuse laser cooling in a cylindrical cavity". In: *Physical Review A* 92.6 (Dec. 2015). DOI: 10.1103/physreva.92.062101 (cit. on p. 10).

[64] S. T. Müller, D. V. Magalhães, R. F. Alves, and V. S. Bagnato. "Compact frequency standard based on an intracavity sample of cold cesium atoms". In: *Journal of the Optical Society of America B* 28.11 (Oct. 2011), p. 2592. DOI: 10.1364/josab.28.002592 (cit. on p. 10).

[65] B. Pelle, R. Szmuk, B. Desruelle, D. Holleville, and A. Landragin. "Cold-Atom-Based Commercial Microwave Clock at the 10^{-15} Level". In: *2018 IEEE International Frequency Control Symposium (IFCS)*. IEEE, May 2018. DOI: 10.1109/fcs.2018.8597468 (cit. on p. 10).

[66] F. Ascarrunz, Y. Dudin, M. C. Delgado, J. Savory, S. Jefferts, N. Time, et al. "Long-Term Frequency Instability of a Portable Cold 87Rb Atomic Clock". In: *Proceedings of the 49th Annual Precise Time and Time Interval Systems and Applications Meeting*. 2018, pp. 107–110 (cit. on p. 10).

[67] M. V. Balabas, T. Karaulanov, M. P. Ledbetter, and D. Budker. "Polarized Alkali-Metal Vapor with Minute-Long Transverse Spin-Relaxation Time". In: *Physical Review Letters* 105.7 (Aug. 2010). DOI: 10.1103/physrevlett.105.070801 (cit. on p. 11).

[68] T. Bandi, C. Affolderbach, and G. Mileti. "Laser-pumped paraffin-coated cell rubidium frequency standard". In: *Journal of Applied Physics* 111.12 (June 2012), p. 124906. DOI: 10.1063/1.4729570 (cit. on p. 11).

[69] R. P. Frueholz, C. H. Volk, and J. C. Camparo. "Use of wall coated cells in atomic frequency standards". In: *Journal of Applied Physics* 54.10 (Oct. 1983), pp. 5613–5617. DOI: 10.1063/1.331820 (cit. on p. 11).

[70] A. Godone, S. Micalizio, F. Levi, and C. Calosso. "Microwave cavities for vapor cell frequency standards". In: *Review of Scientific Instruments* 82.7 (2011), p. 074703. DOI: 10.1063/1.3606641 (cit. on pp. 11, 37, 38, 63, 65, 70, 85).

[71] W. Happer. "Optical Pumping". In: *Reviews of Modern Physics* 44.2 (Apr. 1972), pp. 169–249. DOI: 10.1103/revmodphys.44.169 (cit. on p. 11).

[72] J. Vanier and C. Mandache. "The passive optically pumped Rb frequency standard: the laser approach". In: *Applied Physics B* 87.4 (2007), pp. 565–593 (cit. on p. 12).

[73] G. Mileti, J. Deng, F. Walls, D. Jennings, and R. Drullinger. "Laser-pumped rubidium frequency standards: new analysis and progress". In: *IEEE Journal of Quantum Electronics* 34.2 (1998), pp. 233–237. DOI: 10.1109/3.658700 (cit. on p. 12).

[74] C. Audoin, V. Candelier, and N. Dimarcq. "A limit to the frequency stability of passive frequency standards". In: *Conference on Precision Electromagnetic Measurements*. IEEE, 1990. DOI: 10.1109/cpem.1990.109938 (cit. on p. 13).

[75] G. Kramer. "Noise in passive frequency standards". In: *Proc. Conf. Precise Electromagnetic Measurements*. 1974, pp. 157–159 (cit. on p. 13).

[76] J. C. Camparo. "Conversion of laser phase noise to amplitude noise in an optically thick vapor". In: *J. Opt. Soc. Am. B* 15.3 (Mar. 1998), pp. 1177–1186. DOI: 10.1364/JOSAB.15.001177 (cit. on pp. 13, 32).

[77] J. C. Camparo and J. G. Coffer. "Conversion of laser phase noise to amplitude noise in a resonant atomic vapor: The role of laser linewidth". In: *Phys. Rev. A* 59 (1 Jan. 1999), pp. 728–735. DOI: 10.1103/PhysRevA.59.728 (cit. on pp. 13, 32).

[78] C. Affolderbach and G. Mileti. "A compact laser head with high-frequency stability for Rb atomic clocks and optical instrumentation". In: *Review of Scientific Instruments* 76.7, 073108 (2005). DOI: http://dx.doi.org/10.1063/1.1979493 (cit. on p. 13).

[79] T. Bandi, C. Affolderbach, C. Calosso, and G. Mileti. "High-performance laser-pumped rubidium frequency standard for satellite navigation". In: *Electronics Letters* 47.12 (2011), p. 698. DOI: 10.1049/el.2011.0389 (cit. on p. 13).

[80] V. I. Yudin, M. Y. Basalaev, et al. "Universal methods for suppressing the light shift in atomic clocks based on continuous-wave spectroscopy". In: (Nov. 6, 2019). arXiv: 1911.02935v1 [physics.atom-ph] (cit. on p. 13).

[81] T. C. English, E. Jechart, and T. M. Kwon. "Elimination of the light shift in rubidium gas cell frequency standards using pulsed optical pumping". In: *Tenth Annual Precise Time and Time Interval (PTTI) Applications and Planning Meeting*. Ed. by M. C. Eischer. Nov. 1978 (cit. on pp. 13, 17).

[82] J. Camparo and R. Frueholz. "A three-dimensional model of the gas cell atomic frequency standard". In: *IEEE Transactions on Ultrasonics, Ferroelectrics and Frequency Control* 36.2 (Mar. 1989), pp. 185–190. DOI: 10.1109/58.19149 (cit. on p. 13).

[83] J. C. Camparo. "Atomic Stabilization of Electromagnetic Field Strength Using Rabi Resonances". In: *Phys. Rev. Lett.* 80 (2 Jan. 1998), pp. 222–225. DOI: 10.1103/PhysRevLett.80.222 (cit. on p. 14).

[84] E. Arimondo. "V Coherent Population Trapping in Laser Spectroscopy". In: *Progress in Optics*. Elsevier, 1996, pp. 257–354. DOI: 10.1016/s0079-6638(08)70531-6 (cit. on p. 14).

[85] J. Vanier. "Atomic clocks based on coherent population trapping: a review". In: *Applied Physics B* 81.4 (July 2005), pp. 421–442. DOI: 10.1007/s00340-005-1905-3 (cit. on p. 14).

[86] V. Shah and J. Kitching. "Advances in Coherent Population Trapping for Atomic Clocks". In: *Advances In Atomic, Molecular, and Optical Physics*. Elsevier, 2010, pp. 21–74. DOI: 10.1016/s1049-250x(10)59002-5 (cit. on p. 14).

[87] S. Brandt, A. Nagel, R. Wynands, and D. Meschede. "Buffer-gas-induced linewidth reduction of coherent dark resonances to below50 Hz". In: *Physical Review A* 56.2 (Aug. 1997), R1063–R1066. DOI: 10.1103/physreva.56.r1063 (cit. on p. 14).

[88] M. Merimaa, T. Lindvall, I. Tittonen, and E. Ikonen. "All-optical atomic clock based on coherent population trapping in ˆ85Rb". In: *Journal of the Optical Society of America B* 20.2 (Feb. 2003), p. 273. DOI: 10.1364/josab.20.000273 (cit. on p. 14).

[89] M. Rosenbluh, V. Shah, S. Knappe, and J. Kitching. "Differentially detected coherent population trapping resonances excited by orthogonally polarized laser fields". In: *Optics Express* 14.15 (2006), p. 6588. DOI: 10.1364/oe.14.006588 (cit. on p. 15).

[90] Y.-Y. Jau, E. Miron, A. B. Post, N. N. Kuzma, and W. Happer. "Push-Pull Optical Pumping of Pure Superposition States". In: *Physical Review Letters* 93.16 (Oct. 2004). DOI: 10.1103/physrevlett.93.160802 (cit. on p. 15).

[91] X. Liu, J.-M. Mérolla, S. Guérandel, C. Gorecki, E. de Clercq, and R. Boudot. "Coherent-population-trapping resonances in buffer-gas-filled Cs-vapor cells with push-pull optical pumping". In: *Physical Review A* 87.1 (Jan. 2013). DOI: 10.1103/physreva.87.013416 (cit. on p. 15).

[92] X. Liu, J.-M. Mérolla, S. Guérandel, C. Gorecki, E. de Clercq, and R. Boudot. "Erratum: Coherent-population-trapping resonances in buffer-gas-filled Cs-vapor cells with push-pull optical pumping [Phys. Rev. A87, 013416 (2013)]". In: *Physical Review A* 87.2 (Feb. 2013). DOI: 10.1103/physreva.87.029903 (cit. on p. 15).

[93] F. Levi, A. Godone, and J. Vanier. "The light shift effect in the coherent population trapping cesium maser". In: *IEEE Transactions on Ultrasonics, Ferroelectrics and Frequency Control* 47.2 (Mar. 2000), pp. 466–470. DOI: 10.1109/58.827437 (cit. on p. 15).

[94] M. Zhu and L. S. Cutler. "Theoretical and Experimental Study of Light Shift in a CPT-Based Rb Vapor Cell Frequency Standard". In: *Proceedings of the 32th Annual Precise Time and Time Interval (PTTI) Systems and Applications Meeting*. Nov. 2000, pp. 311–324 (cit. on p. 15).

[95] O. Kozlova, S. Guérandel, and E. de Clercq. "Temperature and pressure shift of the Cs clock transition in the presence of buffer gases: Ne, N 2, Ar". In: *Physical Review A* 83.6 (2011), p. 062714 (cit. on p. 15).

[96] F. Tricot, S. Guerandel, and E. de Clercq. "Contributions to the mid-term frequency noise of the pulsed CPT clock at SYRTE". In: *2018 European Frequency and Time Forum (EFTF)*. IEEE, Apr. 2018. DOI: 10.1109/eftf.2018.8409007 (cit. on pp. 15, 16).

[97] P. Yun, J.-M. Danet, D. Holleville, E. de Clercq, and S. Guérandel. "Constructive polarization modulation for coherent population trapping clock". In: *Applied Physics Letters* 105.23 (Dec. 2014), p. 231106. DOI: 10.1063/1.4903862 (cit. on p. 16).

[98] T. Zanon, S. Guerandel, E. de Clercq, D. Holleville, N. Dimarcq, and A. Clairon. "High Contrast Ramsey Fringes with Coherent-Population-Trapping Pulses in a Double Lambda Atomic System". In: *Phys. Rev. Lett.* 94 (19 May 2005), p. 193002. DOI: 10.1103/PhysRevLett.94.193002 (cit. on p. 16).

[99] S. Micalizio and A. Godone. "Raman-Ramsey resonances in atomic vapor cells: Rabi pulling and optical-density effects". In: *Physical Review A* 99.4 (Apr. 2019). DOI: 10.1103/physreva.99.043425 (cit. on p. 16).

[100] F. Tricot, P. Yun, E. de Clercq, and S. Guerandel. "Latest achievements on the pulsed CPT clock". In: *2017 Joint Conference of the European Frequency and Time Forum and IEEE International Frequency Control Symposium (EFTF/IFCS)*. IEEE, July 2017. DOI: 10.1109/fcs.2017.8088836 (cit. on p. 16).

[101] C. Sanner, N. Huntemann, R. Lange, C. Tamm, and E. Peik. "Autobalanced Ramsey Spectroscopy". In: *Physical Review Letters* 120.5 (Jan. 2018). DOI: 10.1103/physrevlett.120.053602 (cit. on pp. 16, 41).

[102] V. Yudin, A. Taichenachev, M. Y. Basalaev, T. Zanon-Willette, J. Pollock, M. Shuker, E. Donley, and J. Kitching. "Generalized Autobalanced Ramsey Spectroscopy of Clock Transitions". In: *Physical Review Applied* 9.5 (May 2018). DOI: 10.1103/physrevapplied.9.054034 (cit. on pp. 16, 41).

[103] M. Arditi and T. R. Carver. "Atomic Clock Using Microwave Pulse-Coherent Techniques". In: *IEEE Transactions on Instrumentation and Measurement* IM-13.2 & 3 (June 1964), pp. 146–152. DOI: 10.1109/TIM.1964.4313389 (cit. on pp. 16, 17).

[104] C. O. Alley. "Coherent Pulse Technique in the Optical Detection of the 0 - 0 Ground State Hyperfine Resonance in Rubidium 87". In: *Quantum Electronics*. Ed. by C. H. Townes. 1960, p. 146 (cit. on p. 16).

[105] N. F. Ramsey. "A Molecular Beam Resonance Method with Separated Oscillating Fields". In: *Physical Review* 78.6 (June 1950), pp. 695–699. DOI: 10.1103/physrev.78.695 (cit. on p. 17).

[106] A. Godone, S. Micalizio, and F. Levi. "Pulsed optically pumped frequency standard". In: *Physical Review A* 70.2 (Aug. 2004). DOI: 10.1103/physreva.70.023409 (cit. on pp. 17, 38, 64, 70, 93, 94).

[107] C. E. Calosso, A. Godone, F. Levi, and S. Micalizio. "Enhanced temperature sensitivity in vapor-cell frequency standards". In: *IEEE Transactions on Ultrasonics, Ferroelectrics, and Frequency Control* 59.12 (Dec. 2012), pp. 2646–2654. DOI: 10.1109/TUFFC.2012.2505 (cit. on pp. 20, 21, 36, 48, 76, 97).

[108] A. de Marchi, G. D. Rovera, and A. Premoli. "Pulling by Neighbouring Transitions and its Effects on the Performance of Caesium-Beam Frequency Standards". In: *Metrologia* 20.2 (Jan. 1984), pp. 37–47. DOI: 10.1088/0026-1394/20/2/002 (cit. on p. 20).

[109] W. Moreno, M. Pellaton, C. Affolderbach, and G. Mileti. "Barometric Effect in Vapor-Cell Atomic Clocks". In: *IEEE transactions on ultrasonics, ferroelectrics, and frequency control* 65.8 (2018), pp. 1500–1503 (cit. on pp. 21, 76).

[110] W. J. Riley. "The physics of the environmental sensitivity of rubidium gas cell atomic frequency standards". In: *IEEE transactions on ultrasonics, ferroelectrics, and frequency control* 39.2 (1992), pp. 232–240 (cit. on pp. 21, 36, 76).

[111] B. François, C. E. Calosso, M. Abdel Hafiz, S. Micalizio, and R. Boudot. "Simple-design ultra-low phase noise microwave frequency synthesizers for high-performing Cs and Rb vapor-cell atomic clocks". In: *Review of Scientific Instruments* 86.9 (2015), p. 094707 (cit. on pp. 21, 60, 80).

[112] C. E. Calosso, M. Gozzelino, E. Bertacco, S. Micalizio, B. François, and P. Yun. "Generalized electronics for compact atomic clocks". In: *2017 Joint Conference of the European Frequency and Time Forum and IEEE International Frequency Control Symposium (EFTF/IFCS)*. July 2017, pp. 322–323. DOI: 10.1109/FCS.2017.8088881 (cit. on p. 22).

[113] H. Kogelnik and C. V. Shank. "Coupled-Wave Theory of Distributed Feedback Lasers". In: *Journal of Applied Physics* 43.5 (May 1972), pp. 2327–2335. DOI: 10.1063/1.1661499 (cit. on p. 22).

[114] K. Utaka, S. Akiba, K. Sakai, and Y. Matsushima. "Room-temperature CW operation of distributed-feedback buried-heterostructure InGaAsP/InP lasers emitting at 1.57 μm". In: *Electronics Letters* 17.25-26 (1981), p. 961. DOI: 10.1049/el:19810672 (cit. on p. 22).

[115] J. W. Kirchner. "Aliasing in $1/f^{\alpha}$ noise spectra: Origins, consequences, and remedies". In: *Phys. Rev. E* 71 (6 June 2005), p. 066110. DOI: 10.1103/PhysRevE.71.066110 (cit. on p. 28).

[116] F. Vernotte, G. Zalamansky, and E. Lantz. "Time stability characterization and spectral aliasing. Part II: a frequency-domain approach". In: *Metrologia* 35.5 (1998), p. 731 (cit. on p. 28).

[117] J. Rutman. "Characterization of phase and frequency instabilities in precision frequency sources: Fifteen years of progress". In: *Proceedings of the IEEE* 66.9 (Sept. 1978), pp. 1048–1075. DOI: 10.1109/PROC.1978.11080 (cit. on p. 28).

[118] C. E. Calosso, C. Clivati, and S. Micalizio. "Avoiding Aliasing in Allan Variance: An Application to Fiber Link Data Analysis". In: *IEEE Transactions on Ultrasonics, Ferroelectrics, and Frequency Control* 63.4 (Apr. 2016), pp. 646–655. DOI: 10.1109/TUFFC.2016.2519265 (cit. on p. 29).

[119] F. Riehle. *Frequency standards: basics and applications*. John Wiley & Sons, 2006 (cit. on p. 30).

[120] J. Vanier and C. Tomescu. *The Quantum Physics of Atomic Frequency Standards: Recent Developments*. CRC Press, 2015 (cit. on p. 30).

[121] G. J. Dick, J. D. Prestage, C. A. Greenhall, and L. Maleki. *Local oscillator induced degradation of medium-term stability in passive atomic frequency standards*. Tech. rep. CALIFORNIA INST OF TECHNOLOGY PASADENA JET PROPULSION LAB, 1990 (cit. on p. 34).

[122] C. Audoin, G. Santarelli, A. Makdissi, and A. Clairon. "Properties of an oscillator slaved to a periodically interrogated atomic resonator". In: *IEEE Transactions on Ultrasonics, Ferroelectrics, and Frequency Control* 45.4 (July 1998), pp. 877–886. DOI: 10.1109/58.710546 (cit. on pp. 34, 121).

[123] L. L. Presti, D. Rovera, and A. De Marchi. "A simple analysis of the Dick effect in terms of phase noise spectral densities". In: *IEEE transactions on ultrasonics, ferroelectrics, and frequency control* 45.4 (1998), pp. 899–905 (cit. on p. 34).

[124] A. Quessada, R. P. Kovacich, I. Courtillot, A. Clairon, G. Santarelli, and P. Lemonde. "The Dick effect for an optical frequency standard". In: *Journal of Optics B: Quantum and Semiclassical Optics* 5.2 (Apr. 2003), S150–S154. DOI: 10.1088/1464-4266/5/2/373 (cit. on p. 34).

[125] M. Schioppo et al. "Ultrastable optical clock with two cold-atom ensembles". In: *Nature Photonics* 11.1 (Nov. 2016), pp. 48–52. DOI: 10.1038/nphoton.2016.231 (cit. on p. 34).

[126] J.-M. Danet, M. Lours, S. Guérandel, and E. D. Clercq. "Dick effect in a pulsed atomic clock using coherent population trapping". In: *IEEE Transactions on Ultrasonics, Ferroelectrics, and Frequency Control* 61.4 (Apr. 2014), pp. 567–574. DOI: 10.1109/tuffc.2014.2945 (cit. on p. 34).

[127] S. Micalizio, A. Godone, F. Levi, and C. Calosso. "Medium-long term frequency stability of pulsed vapor cell clocks". In: *IEEE Transactions on Ultrasonics, Ferroelectrics, and Frequency Control* 57.7 (July 2010), pp. 1524–1534. DOI: 10.1109/TUFFC.2010.1583 (cit. on pp. 36, 90, 103, 112).

[128] C. Affolderbach, N. Almat, M. Gharavipour, F. Gruet, W. Moreno, M. Pellaton, and G. Mileti. "Selected Studies on High Performance Laser-Pumped Rubidium Atomic Clocks". In: *2018 IEEE International Frequency Control Symposium (IFCS)*. IEEE, 2018. DOI: 10.1109/fcs.2018.8597452 (cit. on pp. 36, 38).

[129] M. Gharavipour, C. Affolderbach, S. Kang, T. Bandi, F. Gruet, M. Pellaton, and G. Mileti. "High performance vapour-cell frequency standards". In: *Journal of Physics: Conference Series* 723 (June 2016), p. 012006. DOI: 10.1088/1742-6596/723/1/012006 (cit. on p. 36).

[130] J. Vanier, R. Kunski, N. Cyr, J. Y. Savard, and M. Têtu. "On hyperfine frequency shifts caused by buffer gases: Application to the optically pumped passive rubidium frequency standard". In: *Journal of Applied Physics* 53.8 (1982), pp. 5387–5391. DOI: 10.1063/1.331467 (cit. on pp. 36, 75, 76).

[131] S. Micalizio, A. Godone, F. Levi, and J. Vanier. "Spin-exchange frequency shift in alkali-metal-vapor cell frequency standards". In: *Physical Review A* 73.3 (Mar. 2006). DOI: 10.1103/physreva.73.033414 (cit. on pp. 36, 74, 77, 90).

[132] C. Affolderbach, W. Moreno, A. E. Ivanov, T. Debogovic, M. Pellaton, A. K. Skrivervik, E. de Rijk, and G. Mileti. "Study of additive manufactured microwave cavities for pulsed optically pumped atomic clock applications". In: *Applied Physics Letters* 112.11 (Mar. 2018), p. 113502. DOI: 10.1063/1.5019444 (cit. on p. 37).

[133] M. Gozzelino, S. Micalizio, F. Levi, A. Godone, and C. E. Calosso. "Reducing Cavity-Pulling Shift in Ramsey-Operated Compact Clocks". In: *IEEE Transactions on Ultrasonics, Ferroelectrics, and Frequency Control* 65.7 (July 2018), pp. 1294–1301. DOI: 10.1109/tuffc.2018.2828987 (cit. on pp. 38, 41, 64, 85).

[134] V. I. Yudin, A. V. Taichenachev, et al. "Hyper-Ramsey spectroscopy of optical clock transitions". In: *Physical Review A* 82.1 (July 2010). DOI: 10.1103/physreva.82.011804 (cit. on p. 41).

[135] T. Zanon-Willette, V. I. Yudin, and A. V. Taichenachev. "Generalized hyper-Ramsey resonance with separated oscillating fields". In: *Physical Review A* 92.2 (Aug. 2015). DOI: 10.1103/physreva.92.023416 (cit. on p. 41).

[136] C. E. Calosso and E. Rubiola. "Phase noise and jitter in digital electronic components". In: *2014 IEEE International Frequency Control Symposium (FCS)*. May 2014, pp. 1–3. DOI: 10.1109/FCS.2014.6859990 (cit. on p. 42).

[137] C. E. Calosso, S. Micalizio, A. Godone, E. K. Bertacco, and F. Levi. "Electronics for the Pulsed Rubidium Clock: Design and Characterization". In: *IEEE Transactions on Ultrasonics, Ferroelectrics, and Frequency Control* 54.9 (Sept. 2007), pp. 1731–1740. DOI: 10.1109/TUFFC.2007.458 (cit. on p. 46).

[138] A. Horsley, G.-X. Du, M. Pellaton, C. Affolderbach, G. Mileti, and P. Treutlein. "Imaging of relaxation times and microwave field strength in a microfabricated vapor cell". In: *Phys. Rev. A* 88 (6 Dec. 2013), p. 063407. DOI: 10.1103/PhysRevA.88.063407 (cit. on p. 46).

[139] J. L. Hall, L. Hollberg, T. Baer, and H. G. Robinson. "Optical heterodyne saturation spectroscopy". In: *Applied Physics Letters* 39.9 (Nov. 1981), pp. 680–682. DOI: 10.1063/1.92867 (cit. on p. 50).

[140] D. W. Preston. "Doppler-free saturated absorption: Laser spectroscopy". In: *American Journal of Physics* 64.11 (Nov. 1996), pp. 1432–1436. DOI: 10.1119/1.18457 (cit. on p. 50).

[141] J. Millo et al. "Ultralow noise microwave generation with fiber-based optical frequency comb and application to atomic fountain clock". In: *Applied Physics Letters* 94.14 (Apr. 2009), p. 141105. DOI: 10.1063/1.3112574 (cit. on p. 57).

[142] T. M. Fortier et al. "Generation of ultrastable microwaves via optical frequency division". In: *Nature Photonics* 5.7 (June 2011), pp. 425–429. DOI: 10.1038/nphoton.2011.121 (cit. on p. 57).

[143] F. Levi, J. Camparo, B. Francois, C. E. Calosso, S. Micalizio, and A. Godone. "Precision test of the ac Stark shift in a rubidium atomic vapor". In: *Physical Review A* 93.2 (Feb. 2016). DOI: 10.1103/physreva.93.023433 (cit. on p. 58).

[144] W. Happer and B. S. Mathur. "Effective Operator Formalism in Optical Pumping". In: *Physical Review* 163.1 (Nov. 1967), pp. 12–25. DOI: 10.1103/physrev.163.12 (cit. on pp. 58, 76).

[145] H. E. Williams, T. M. Kwon, and T. McClelland. "Compact Rectangular Cavity for Rubidium Vapor Cell Frequency Standards". In: *37th Annual Symposium on Frequency Control*. June 1983, pp. 12–17. DOI: 10.1109/FREQ.1983.200637 (cit. on p. 63).

[146] D. A. Howe and F. L. Walls. "A Compact Hydrogen Maser with Exceptional Long-Term Stability". In: *IEEE Transactions on Instrumentation and Measurement* 32.1 (Mar. 1983), pp. 218–223. DOI: 10.1109/TIM.1983.4315045 (cit. on p. 63).

[147] D. D. Marco, K. Drissi, N. Delhote, O. Tantot, P.-M. Geffroy, S. Verdeyme, and T. Chartier. "Dielectric properties of pure alumina from 8GHz to 73GHz". In: *Journal of the European Ceramic Society* 36.14 (2016), pp. 3355–3361. DOI: https://doi.org/10.1016/j.jeurceramsoc.2016.05.047 (cit. on p. 64).

[148] D. D. Marco, K. Drissi, P.-M. Geffroy, N. Delhote, O. Tantot, S. Verdeyme, and T. Chartier. "Dielectric properties of alumina doped with TiO2 from 13 to 73GHz". In: *Journal of the European Ceramic Society* 37.2 (2017), pp. 641–646. DOI: https://doi.org/10.1016/j.jeurceramsoc.2016.09.016 (cit. on p. 64).

[149] A. Godone, S. Micalizio, F. Levi, and C. Calosso. "Physics characterization and frequency stability of the pulsed rubidium maser". In: *Physical Review A* 74.4 (Oct. 2006). DOI: 10.1103/physreva.74.043401 (cit. on p. 64).

[150] J. D. Joannopoulos, P. R. Villeneuve, and S. Fan. "Photonic crystals". In: *Solid State Communications* 102.2-3 (1997), pp. 165–173 (cit. on p. 68).

[151] D. M. Pozar. *Microwave Engineering*. 3rd ed. John Wiley & Sons, Inc., 2005 (cit. on p. 69).

[152] G. Missout and J. Vanier. "Pressure and Temperature Coefficients of the More Commonly Used Buffer Gases in Rubidium Vapor Frequency Standards". In: *IEEE Transactions on Instrumentation and Measurement* 24.2 (June 1975), pp. 180–184. DOI: 10.1109/TIM.1975.4314400 (cit. on p. 75).

[153] B. Bean and R. Lambert. "Temperature dependence of hyperfine density shifts. IV. Na 23, K 39, and Rb 85 in He, Ne, Ar, and N2 at low temperatures". In: *Physical Review A* 13.1 (1976), p. 492 (cit. on p. 75).

[154] V. V. Batygin and V. S. Zholnerov. "Temperature dependence of the hyperfine transition frequency of the ground state of Rb87 in a buffer medium". In: *Optics and Spectroscopy* 39 (1975), pp. 254–255 (cit. on p. 75).

[155] N. Cyr. PhD thesis. Universite Laval, Quebec (unpublished), 1983 (cit. on p. 75).

[156] M. Huang, C. M. Klimcak, and J. C. Camparo. "Vapor-cell clock frequency and environmental pressure: Resonance-cell volume changes". In: *2010 IEEE International Frequency Control Symposium*. June 2010, pp. 208–211. DOI: 10.1109/FREQ.2010.5556344 (cit. on p. 76).

[157] M. D. Rotondaro and G. P. Perram. "Collisional broadening and shift of the rubidium D1 and D2 lines (52S12 → 52P12, 52P32) by rare gases, H2, D2, N2, CH4 and CF4". In: *Journal of Quantitative Spectroscopy and Radiative Transfer* 57.4 (1997), pp. 497–507. DOI: https://doi.org/10.1016/S0022-4073(96)00147-1 (cit. on pp. 76, 77, 83).

[158] J. Bellisio, P. Davidovits, and P. Kindlmann. "Quenching of rubidium resonance radiation by nitrogen and the noble gases". In: *The Journal of Chemical Physics* 48.5 (1968), pp. 2376–2377 (cit. on p. 76).

[159] A. F. Molisch and B. P. Oehry. *Radiation trapping in atomic vapours*. Oxford University Press, 1998 (cit. on p. 76).

[160] M. A. Bouchiat, J. Brossel, and L. C. Pottier. "Evidence for Rb-Rare-Gas Molecules from the Relaxation of Polarized Rb Atoms in a Rare Gas. Experimental Results". In: *The Journal of Chemical Physics* 56.7 (1972), pp. 3703–3714. DOI: 10.1063/1.1677750 (cit. on p. 77).

[161] W. Franzen. "Spin Relaxation of Optically Aligned Rubidium Vapor". In: *Physical Review* 115.4 (Aug. 1959), pp. 850–856. DOI: 10.1103/physrev.115.850 (cit. on pp. 77, 91).

[162] F. A. Franz. "Rubidium Spin Relaxation in the Rare Gases Under Ultraclean Conditions". In: *Physical Review* 139.3A (Aug. 1965), A603–A611. DOI: 10.1103/physrev.139.a603 (cit. on p. 77).

[163] J. Vanier, J.-F. Simard, and J.-S. Boulanger. "Relaxation and frequency shifts in the ground state of Rb85". In: *Physical Review A* 9.3 (Mar. 1974), pp. 1031–1040. DOI: 10.1103/physreva.9.1031 (cit. on p. 77).

[164] F. A. Franz and C. Volk. "Spin relaxation of rubidium atoms in sudden and quasimolecular collisions with light-noble-gas atoms". In: *Physical Review A* 14.5 (Nov. 1976), pp. 1711–1728. DOI: 10.1103/physreva.14.1711 (cit. on p. 77).

[165] R. J. McNeal. "Disorientation Cross Sections in Optical Pumping". In: *The Journal of Chemical Physics* 37.11 (Dec. 1962), pp. 2726–2727. DOI: 10.1063/1.1733089 (cit. on p. 77).

[166] J. Vanier. "Relaxation in Rubidium-87 and the Rubidium Maser". In: *Physical Review* 168.1 (Apr. 1968), pp. 129–149. DOI: 10.1103/physrev.168.129 (cit. on p. 77).

[167] J. G. Coffer, M. Anderson, and J. C. Camparo. "Collisional dephasing and the reduction of laser phase-noise to amplitude-noise conversion in a resonant atomic vapor". In: *Physical Review A* 65.3 (Feb. 2002). DOI: 10.1103/physreva.65.033807 (cit. on p. 80).

[168] V. Faddeeva and N. Terent'ev. "Tables of values of the function $w(z) = e^{-z^2}(1 + 2i/\sqrt{\pi}\int_0^z \exp t^2 dt)$ for complex argument," in: *Gosud. Izdat. Teh.-Teor. Lit., Moscow* (1954) (cit. on p. 83).

[169] D. A. Steck. *Rubidium 87 D line data.* http://steck.us/alkalidata. (revision 2.1.5,13 January 2015). 2001 (cit. on p. 83).

[170] M. Gharavipour, C. Affolderbach, F. Gruet, I. S. Radojičić, A. J. Krmpot, B. M. Jelenković, and G. Mileti. "Optically-detected spin-echo method for relaxation times measurements in a Rb atomic vapor". In: *New Journal of Physics* 19.6 (June 2017), p. 063027. DOI: 10.1088/1367-2630/aa73c2 (cit. on p. 91).

[171] S. Micalizio, C. E. Calosso, F. Levi, and A. Godone. "Ramsey-fringe shape in an alkali-metal vapor cell with buffer gas". In: *Physical Review A* 88.3 (Sept. 2013). DOI: 10.1103/physreva.88.033401 (cit. on p. 100).

[172] P. Berceau, M. Taylor, J. Kahn, and L. Hollberg. "Space-time reference with an optical link". In: *Classical and Quantum Gravity* 33.13 (May 2016), p. 135007. DOI: 10.1088/0264-9381/33/13/135007 (cit. on p. 106).

[173] P. Laurent, D. Massonnet, L. Cacciapuoti, and C. Salomon. "The ACES-PHARAO space mission". In: *Comptes Rendus Physique* 16.5 (2015), pp. 540–552. DOI: http://dx.doi.org/10.1016/j.crhy.2015.05.002 (cit. on p. 107).

[174] T. Sumner, J. Pendlebury, and K. Smith. "Conventional magnetic shielding". In: *Journal of Physics D: Applied Physics* 20.9 (1987), p. 1095 (cit. on p. 112).

This Ph.D. thesis has been typeset by means of the TEX-system facilities. The typesetting engine was pdfLATEX. The document class was `toptesi`, by Claudio Beccari, with option `tipotesi=scudo`. This class is available in every up-to-date and complete TEX-system installation.